Mistral and Tramontane: Simulation of Mesoscale Winds in Regional Climate Models

Dissertation
zur Erlangung des Doktorgrades
der Naturwissenschaften

vorgelegt beim Fachbereich 11 Geowissenschaften / Geographie
der Johann Wolfgang Goethe-Universität
in Frankfurt am Main

von
Anika Obermann-Hellhund
aus Gießen

Frankfurt 2017
(D 30)

Vom Fachbereich 11 Geowissenschaften / Geographie der
Johann Wolfgang Goethe-Universität als Dissertation angenommen.

Dekan:
Prof. Dr. Peter Lindner

Gutachter:
Prof. Dr. Bodo Ahrens
Prof. Dr. Heiko Paeth

Datum der Disputation:

Abstract

Mistral and Tramontane are wind systems in southern France and the western Mediterranean Sea. Both are caused by similar synoptic situations and channeled in valleys. Their relevance for the climate of the western Mediterranean region motivated this work. The representation of Mistral and Tramontane in regional climate simulations was surveyed with the models ALADIN, WRF, PROMES, COSMO-CLM, RegCM, and LMDZ. ERA-Interim and global CMIP5 simulations (MPI-ESM, CMCC-CM, HadGEM2-ES, and CNRM-CM5) provided the lateral boundary data for the regional simulations regarding the 20th century and two representative concentration pathways for the 21st century (RCP4.5 and RCP8.5).

A Mistral and Tramontane time series, a principal component analysis of pressure fields, and a Bayesian network were combined to develop a classification algorithm to identify pressure patterns in favor of Mistral and Tramontane. The regional climate models were able to reproduce the observed climatology of Mistral and Tramontane. Compared to observational data (SAFRAN and QuikSCAT), the simulations underestimate the wind speed over the Mediterranean Sea, mainly at the borders of the main flow. Simulations with smaller grid spacing showed better agreement with the observations.

A sensitivity study tested the influence of the Charnock parameter on the Mistral wind field. Its value impacted both wind speed and wind direction. Decreasing the orographic resolution in idealized simulations using COSMO-CLM caused a reduction in wind speed and a broader flow area. Including a parameterization for subgrid scale orography improved the simulation. However, an accurate simulation of Mistral and Tramontane still requires a high-resolution orography.

The classification algorithm also was applied to pressure fields from regional climate simulations driven by global simulation data. At the end of the 21st century, only small, non-significant changes in the number of Mistral days per year occur in the projection simulations. The number of Tramontane days per year decreased significantly.

Kurzzusammenfassung

Mistral und Tramontane sind die im Westen des Mittelmeeres vorherrschenden Windsysteme. Beide entstehen unter ähnlichen synoptischen Bedingungen und zeichnen sich durch Kanalisierung in Tälern Südfrankreichs aus. Die Relevanz von Mistral und Tramontane für das Klima des westlichen Mittelmeergebiets, unter anderem durch Tiefenwasserbildung, motivierte diese Arbeit. Es wurde die Darstellung von Mistral und Tramontane in regionalen Klimasimulationen mit den Modellen ALADIN, WRF, PROMES, COSMO-CLM, RegCM und LMDZ untersucht. Angetrieben wurden die Simulationen mit Daten aus ERA-Interim und globalen CMIP5 Simulationen (MPI-ESM, CMCC-CM, HadGEM2-ES und CNRM-CM5). Zwei repräsentative Konzentrationspfade wurden untersucht (RCP4.5 und RCP8.5).

Eine Mistral- und Tramontane-Zeitserie wurde zusammen mit einer Hauptkomponentenanalyse von Druckfeldern und einem Bayesschen Netz zur Entwicklung eines Druckmuster-Klassifikationsalgorithmus genutzt. Die regionalen Klimamodelle sind in der Lage die Klimatologie von Mistral und Tramontane zu reproduzieren. Im Vergleich mit Beobachtungsdaten (SAFRAN und QuikSCAT) unterschätzten die Simulationen die Windgeschwindigkeit über dem Mittelmeer, besonders an den Rändern der Hauptströmung. Simulationen mit kleinerer Gitterweite zeigten eine größere Übereinstimmung mit den Beobachtungen.

In einer Sensitivitätsstudie wurde der Einfluss des Charnock-Parameters auf das Mistral-Windfeld getestet. Es zeigte sich, dass sein Wert sowohl die Windgeschwindigkeit als auch die Windrichtung beeinflusst. Außerdem führte eine Verringerung der Orographiauflösung in idealisierten Simulationen mit COSMO-CLM zu einer geringeren Windgeschwindigkeit und gleichzeitig einem breiteren Mistralstrom. Die Berücksichtigung einer Parametrisierung für subgridskalige Orographie verbesserte die Darstellung. Dies zeigt, dass für eine genaue Simulation von Mistral und Tramontane nicht nur eine hohe Auflösung im numerischen Gitter, sondern auch in der Orographie wünschenswert ist.

Der Klassifikationsalgorithmus wurde auch auf Druckmuster aus regionalen Klimasimulationen, die mit globalen Simulationsdaten angetrieben wurden, angewendet. Gegen Ende des 21. Jahrhunderts zeigten sich kleine, statistisch nicht signifikante Änderungen in der Anzahl der Mistraltage pro Jahr für beide repräsentative Konzentrationspfade. Die Anzahl der Tramontanetage pro Jahr nahm jedoch signifikant ab.

Contents

Deutsche Zusammenfassung **9**

List of Contributing Peer-Reviewed Publications **15**

1. Introduction **17**

2. Theoretical Background **23**
2.1. Large Scale Flow 23
2.2. Planetary Boundary Layer 26
2.3. Downslope Winds 28
2.4. Gap Winds 30
2.5. Hydraulic Jumps 32

3. Data **33**
3.1. Observational Datasets 33
3.2. Reanalysis Data 37
3.3. Climate Simulations 38

4. Methods **43**
4.1. Time Series of observed Mistral and Tramontane Events 43
4.2. Classification Algorithm for sea-level Pressure Patterns 44
4.3. Idealized Simulations with COSMO-CLM 46
4.4. Evaluation 47

5. Results and Discussion **49**
5.1. How well do RCMs simulate the Mistral and Tramontane permitting sea-level Pressure Patterns? 49
5.2. How well are the Wind Speed and Wind Direction Patterns represented? 53
5.3. Which Factors determine the Mistral and Tramontane Representation in Simulations? 59
5.4. Which Changes in Mistral and Tramontane can be found in Climate Projections? 65

6. Conclusion **69**

A. Paper 1:
Mistral and Tramontane Wind Speed and Wind Direction Patterns in Regional Climate Simulations **71**

B. Paper 2:
Influence of Sea Surface Roughness Length Parameterization on Mistral and Tramontane Simulations **107**

C. Paper 3:
Mistral and Tramontane Simulations with changing Resolution of Orography **119**

D. Paper 4:
Mistral and Tramontane Wind Systems in Climate Simulations from 1950 to 2100 **131**

Bibliography **155**

Acknowledgements **167**

Lebenslauf **169**

Deutsche Zusammenfassung

Mistral und Tramontane:

Simulation mesoskaliger Windsysteme mit regionalen Klimamodellen

Die Mittelmeerregion wird seit mehreren zehntausend Jahren von modernen Menschen bewohnt. An den östlichen Küsten des Mittelmeeres, in Ägypten und dem fruchtbaren Halbmond entwickelten sich frühe menschliche Zivilisationen und Technologien wie Landwirtschaft und Bewässerung. Namensgebend für die Mittelmeerregion ist das Mittelmeer, das frühen Handel zwischen den Küstenstädten ermöglichte (Abulafia and Bischoff (2013)).

Auch für die Klimaforschung ist die Region interessant. In den letzten zehntausend Jahren traten im Mittelmeerraum mehrere Wechsel sowohl zwischen warmen und kalten Perioden als auch zwischen trockenen und feuchten Perioden auf, darunter sind die mittelalterliche Warmzeit und die Kleine Eiszeit. Die Region wird als ein Hotspot des Klimawandels angesehen (Giorgi (2006); Diffenbaugh and Giorgi (2012)). Daher werden Simulationen des vergangenen, gegenwärtigen und zukünftigen Klimas in der Mittelmeerregion entwickelt und kontinuierlich verbessert.

Klimasimulationen werden mit Hilfe von numerischen Klimamodellen angefertigt, die die verschiedenen Sphären des Klimasystems simulieren (zum Beispiel Atmosphäre, Ozean oder Boden). Globale Klimamodelle simulieren dabei die gesamte Erde mit Hilfe eines dreidimensionalen Gitters, dessen Gitterlinien einen horizontalen Abstand von etwa 100 km haben. Für diese Gitterzellen lösen die Modelle ein Set aus Differenzialgleichungen, die die grundlegenden Gleichungen der Physik beschreiben. Durch den großen Abstand der Gitterpunkte müssen kleinskalige Prozesse, die innerhalb einer Gitterzelle stattfinden, genähert und parametrisiert werden.

Die Mittelmeergegend hat eine komplexe Geographie. Gemäßigtes Klima, Trockenklimate und Schneeklimate treten in relativ kleinen Abständen auf (Lionello et al. (2012)). Durch diese verschiedenen Landschaften, und auch durch viele Inseln verschiedenster Größe, Meerengen, Bergketten und Meere, ist der Mittelmeerraum eine interessante, aber auch herausfordernde Studienregion für Klimasimulationen.

Um die kleinräumigen Phänomene untersuchen zu können, werden regionale Klimamodelle verwendet. Sie basieren auf den gleichen Differenzialgleichungen wie globale Klimamodelle, aber lösen diese nur für einen Bereich der Erde. Damit können sie wie ein Vergrößerungsglas für globale Klimamodelle benutzt werden. An den Rändern der mit dem regionalen Klimamodell simulierten Region müssen die Randbedingungen aus einem globalen Klimamodell oder einem anderen Datensatz bereitgestellt werden. Dieses Verfeinern der globalen Berechnungen durch regionale Klimasimulationen wird auf internationaler Ebene von dem CORDEX Projekt (Giorgi and Gutowski (2015)) und im Mittelmeerraum durch Med-CORDEX (Ruti et al. (2016)) koordiniert. Diese Projekte geben einen Rahmen vor, der die Vergleichbarkeit von Simulationen mit verschiedenen regionalen Klimamodellen sicherstellt.

Diese Arbeit beschäftigt sich mit Windgeschwindigkeit und -richtung, die zu den die für den Menschen wichtigsten und erfahrbarsten Wettererscheinungen gehören. Hohe Windgeschwindigkeiten und besonders Böen können hohe Schäden verursachen. Außerdem ist die Vorhersage von Wind interessant für die Erzeugung von Windenergie und die Simulation von Ozeanströmungen.

In der Mittelmeerregion gibt es viele durch die lokale Orographie erzeugte mesoskalige Windsysteme, darunter Mistral und Tramontane in Südfrankreich und über dem westlichen Mittelmeer. Mistral und Tramontane werden durch ähnliche synoptische Bedingungen in Kombination mit der lokalen Orographie verursacht und treten daher oft gleichzeitig auf. Beide Windsysteme zeichnen sich durch Kanalisierung in Tälern Südfrankreichs aus. Dadurch zeigen sie sowohl Charakteristika von "gap flows" als auch "downslope flows" (Lionello et al. (2012)) und sind interessante Testfälle für Simulationen dieser physikalischen Phänomene. Auch die Ozeanforschung benötigt eine akkurate Vorhersage von Mistral und Tramontane, weil sie durch Kaltluftadvektion die Tiefenwasserbildung fördern und so die Zirkulation des Mittelmeeres beeinflussen (Schott et al. (1996); Béranger et al. (2010)).

Diese Relevanz für das Klima des westlichen Mittelmeergebiets motivierte diese Arbeit, die sich mit der Darstellung von Mistral und Tramontane in regionalen Klimamodellen beschäftigt. Aus den obigen Ausführungen können die folgenden Fragenkomplexe erschlossen werden, die im Folgenden behandelt werden:

- Wie gut können regionale Klimamodelle die Mistral und Tramontane begünstigenden Druckmuster reproduzieren?

- Mit welcher Genauigkeit werden die Windgeschwindigkeits- und Windrichtungsfelder dargestellt?
- Welche Faktoren beeinflussen die Darstellung der Windfelder?
- Welche möglichen zukünftigen Änderungen lassen sich aus Klimaprojektionen ableiten?

Die in dieser Arbeit diskutierten regionalen Klimasimulationen stammen aus der Med-CORDEX Datenbank (www.medcordex.org). Im Einzelnen sind dies ALADIN (Colin et al. (2010); Herrmann et al. (2011)), WRF (Skamarock et al. (2008)), PROMES (Domínguez et al. (2010)), COSMO-CLM Rockel et al. (2008), RegCM (Giorgi et al. (2012)) und LMDZ (Hourdin et al. (2006)). Angetrieben wurden die Simulationen mit Daten aus dem Reanalyseprodukt ERA-Interim (Dee et al. (2011)), oder mit Daten aus globalen Simulationen.

Die hier untersuchten globalen Klimamodelle sind MPI-ESM (Mauritsen et al. (2012); Giorgetta et al. (2013)), CMCC-CM (Madec et al. (1997)), HadGEM2-ES (Martin et al. (2011)) und CNRM-CM5 (Voldoire et al. (2013)). Sie sind Teil von CMIP5 (Taylor et al. (2012)) und berücksichtigen zwei repräsentative Konzentrationspfade (Representative Concentration Pathways, RCPs), die die mögliche Entwicklung des Strahlungsantriebs im 21. Jahrhundert darstellen. Dies sind RCP4.5 mit +4,5 W/m^2 und RCP8.5 mit +8,5 W/m^2 im Vergleich zu 1850. Während ERA-Interim ab 1979 bis in die Gegenwart verfügbar ist, decken die globalen Simulationen einen längeren Zeitraum ab (1950–2100).

Zur Evaluation der Simulationsergebnisse wurden Beobachtungsdaten als Referenz benötigt. Zunächst wurde eine 30-Jahreszeitserie der beobachteten Mistral- und Tramontaneereignisse erstellt. Diese wurde aus Böenbeobachtungen (Jacq et al. (2005); Jacq (2011)) abgeleitet. Neun Stationen im Einzugsgebiet des Mistral und vier Stationen im Tramontanegebiet sind verfügbar. Ein Tag wurde als Mistraltag eingeordnet, wenn im Rhônetal, in den Ebenen zwischen dem Tal und der Küste und an der Küste von jeweils mindestens einer Station Böen aus der jeweils vorherrschenden Mistralrichtung gemessen wurden. Für Tramontane wurden die Stationen in zwei Bereiche eingeteilt, wobei ebenfalls in beiden Bereichen Böen gemessen werden mussten. Diese Methode stellt sicher, dass nur Tage mit einem voll entwickelten Mistral bzw. Tramontane als solche gezählt werden. In den Jahren 1981–2010 wurden so an 32 % der Tage Tramontaneereignisse und an 16 % der Tage Mistralereignisse identifiziert. An 12,6 % der Tage traten sowohl Mistral als auch Tramontane auf.

Diese Zeitserie wurde als Referenz für einen Druckmuster-Klassifikationsalgorithmus verwendet. Dazu wurden zunächst die täglichen Druckmuster von ERA-Interim auf Empirische Orthogonalfunktionen (EOFs, von Storch and Zwiers (2001)) projiziert. Die daraus resultierenden Hauptkomponenten wurden zusammen mit der Mistral- und

Tramontanezeitserie zum Training eines Bayesschen Netzes (Scutari (2010)) genutzt. Das trainierte Bayessche Netz berechnet nun aus einem Satz Hauptkomponenten eine Zahl, die damit in Zusammenhang steht, wie ähnlich das Druckmuster den Druckmustern während Mistral- und Tramontanetagen in den Trainingsdaten ist und damit ein Maß dafür, wie wahrscheinlich an dem gegebenen Tag ein Mistral oder Tramontane aufgetreten ist. Das Bayessche Netz kann auch ein Maß für Daten aus anderen Klimamodellen angeben, solange diese auf die gleichen EOFs wie der Trainingsdatensatz projiziert wurden.

Das trainierte Bayessche Netz identifizierte an 70 % der Tage mit den Beobachtungen übereinstimmende Mistral- und Tramontaneereignisse in ERA-Interim. Die sechs in dieser Arbeit untersuchten regionalen Klimamodelle erreichen etwa 90 % des von ERA-Interim erreichten Wertes. Dies ist ein guter Wert, weil die regionalen Klimamodelle an den Rändern mit ERA-Interim Daten angetrieben wurden.

Betrachtet man die Anzahl der Mistral- und Tramontanetage pro Jahr, so sind die Modelle in der Lage, die Jahre mit besonders wenig oder besonders vielen solcher Ereignisse zu reproduzieren. Schwieriger gestaltet sich die Simulation der Ereignisdauern. Die beobachtete mittlere Dauer eines Mistralereignisses ist 1,7 Tage, in den Simulationen finden sich jedoch Werte von 2,0–2,3 Tagen. Bei Tramontane liegt die beobachtete Dauer bei 2,5 Tagen und die simulierte bei 2,9–3,5 Tagen.

An Tagen, wo ein Mistral oder Tramontane sowohl beobachtet als auch in den simulierten Druckmustern gefunden wurde, ist es von Interesse, wie die simulierten und beobachteten Windfelder sich zueinander verhalten. Die Windfelder von ERA-Interim, ALADIN, WRF, PROMES, COSMO-CLM und LMDZ wurden dazu mit Daten von SAFRAN (Vidal et al. (2010); Quintana-Seguí et al. (2008)) und QuikSCAT (Lungu et al. (2006)) verglichen. Die Modelle zeigen zu einem großen Teil geringere Abweichungen von den Beobachtungen als ERA-Interim. Allerdings zeigten sich einige Schwachstellen in der Simulation kleinskaliger Muster.

An Tagen mit Mistral und Tramontane wird die Windgeschwindigkeit über dem Mittelmeer von fast allen Modellen unterschätzt. Die Unterschätzung ist am größten an den Rändern des von Mistral und Tramontane betroffenen Mittelmeergebiets. Außerdem zeigen alle Simulationen einen im Vergleich zu QuikSCAT im Uhrzeigersinn gedrehten Wind. Simulationen mit höherer Auflösung zeigten geringere Abweichungen von den Beobachtungen. Von diesen Ergebnissen ausgehend wurden verschiedene Effekte in Sensitivitätsstudien und idealisierten Simulationen untersucht.

Eine mögliche Ursache für das Muster in der Abweichung über dem Mittelmeer ist die Parametrisierung der Rauhigkeitslänge über Wasser. Diese ist abhängig von der Windgeschwindigkeit und einem zu wählenden Parameter, dem Charnock Parameter (α, Charnock (1955)). Dazu wurde eine Sensitivitätsstudie mit COSMO-CLM durchgeführt. Der Wert von α im Bereich des Golfe du Lion wurde variiert und am Rand

dieses Modellbereichs die Randbedingungen aus einem Med-CORDEX COSMO-CLM Lauf mit gleicher Gitterweite vorgeschrieben. Höhere Werte von α führten nicht nur zu geringeren Windgeschwindigkeiten, sondern auch einer gegen den Uhrzeigersinn gerichteten Drehung des Windes.

Außerdem wurden idealisierte Simulationen mit COSMO-CLM durchgeführt. In vier verschiedenen Konfigurationen wurden die Corioliskraft, Flüsse an der Erdoberfläche und die subgridskalige Orographie an- und abgeschaltet. In allen vier Konfigurationen wurden verschiedene Auflösungen der Orographie getestet, während die Gitterweite der Simulation konstant blieb. Je geringer die Auflösung der Orographie war, desto niedrigere Windgeschwindigkeiten wurden simuliert. Allerdings stiegen die Windgeschwindigkeiten an den Rändern von Mistral und Tramontane an. Dies konnte damit erklärt werden, dass bei geringerer Auflösung das Rhônetal breiter wird, was eine größere Fläche südlich des Tals dem Einfluss des Mistral aussetzt. Gleichzeitig wird allerdings auch der Querschnitt des Tals größer, was die Beschleunigung durch Kanalisierungseffekte reduziert.

Zusammen führen beide Effekte zu einer Verlagerung des Hauptflusses und der longitudinalen Position der Strömung mit der höchsten Geschwindigkeit um 10–45 km. Dies ist bedeutsam, weil im Golfe du Lion Vortices in der Meeresströmung mit Durchmessern von 12 bis 28 km gefunden wurden (Allou et al. (2010)) und eine größere Verschiebung des Windfeldes die Wechselwirkung mit den Vortices verfälschen könnte. Eine hohe Auflösung der Orographie ist daher erstrebenswert, besonders wenn gekoppelte Simulationen gemacht werden oder das Windfeld zur Berechnung von Ozeanströmungen herangezogen werden soll.

Regionale Klimasimulationen stehen nicht nur für die Vergangenheit zur Verfügung sondern können auch mit Randbedingungen aus globalen Simulationen des zukünftigen Klimas angetrieben werden. Hier wurden drei regionale Klimamodelle (ALADIN, WRF und COSMO-CLM) mit fünf globalen Klimamodellen angetrieben (MPI-ESM-LR, MPI-ESM-HR, CMCC-CM, HadGEM und CNRM-CM5). Die resultierenden Druckmuster wurden wie oben beschrieben mit Hilfe eines Bayesschen Netzes klassifiziert.

Gegen Ende des 21. Jahrhunderts zeigen die Simulationen nur kleine Änderungen in der Häufigkeit von Mistraltagen pro Jahr. Dies gilt für beide untersuchte repräsentative Konzentrationspfade, RCP4.5 und RCP8.5. Dagegen zeigt sich eine signifikante Abnahme an Tramontanetagen pro Jahr. Außerdem ist das 90. Perzentil der Windgeschwindigkeit in RCP8.5 niedriger als in RCP4.5. Diese Verringerung wurde auch in anderen Studien gefunden und könnte einer Änderung der Mistral- und Tramontaneereignisse geschuldet sein. Die Druckmusterklassifikationen der regionalen Klimamodelle und des jeweils antreibenden globalen Klimamodells stimmen an etwa 80 % der Tage überein.

In dieser Studie wurden die regionalen Klimamodelle mit verschiedenen globalen Klimamodellen angetrieben, was es schwierig macht, den Einfluss der globalen Modelle auf die regionalen Modelle abzuschätzen. Für zukünftige Studien wäre es wünschenswert, wenn mehrere globale Modelle zum Antrieb des gleichen regionalen Modells genutzt würden und umgekehrt. Dies könnte die Ensemblegröße und damit die Aussagekraft der Simulationen des 21. Jahrhunderts erhöhen.

List of Contributing Peer-Reviewed Publications

- Anika Obermann, Sophie Bastin, Sophie Belamari, Dario Conte, Miguel Angel Gaertner, Laurent Li, and Bodo Ahrens
  Mistral and Tramontane Wind Speed and Wind Direction Patterns in Regional Climate Simulations
  Climate Dynamics (2016), 1–18.
- Anika Obermann, Benedikt Edelmann, and Bodo Ahrens
  Influence of Sea Surface Roughness Length Parameterization on Mistral and Tramontane Simulations
  Advances in Science and Research (2016), 13, 107–112.
- Anika Obermann-Hellhund and Bodo Ahrens
  Mistral and Tramontane Simulations with changing Resolution of Orography
  Atmospheric Science Letters (2017), submitted
- Anika Obermann-Hellhund, Dario Conte, Samuel Somot, Csaba Zsolt Torma, and Bodo Ahrens
  Mistral and Tramontane Wind Systems in Climate Simulations from 1950 to 2100
  Climate Dynamics (2017), 1–11

1. Introduction

Modern humans have inhabited the Mediterranean region (left panel of Figure 1.1) for ten thousands of years. At its eastern coasts, in Egypt, and the Fertile Crescent, early human civilizations evolved, agriculture, irrigation, and many other technologies were developed (Abulafia and Bischoff (2013)). The centerpiece of the Mediterranean region is the Mediterranean Sea, which connects to the Atlantic via the Strait of Gibraltar. Many ancient trade routes crossed the Mediterranean Sea and contributed to the development of the civilizations on the circumjacent shores.

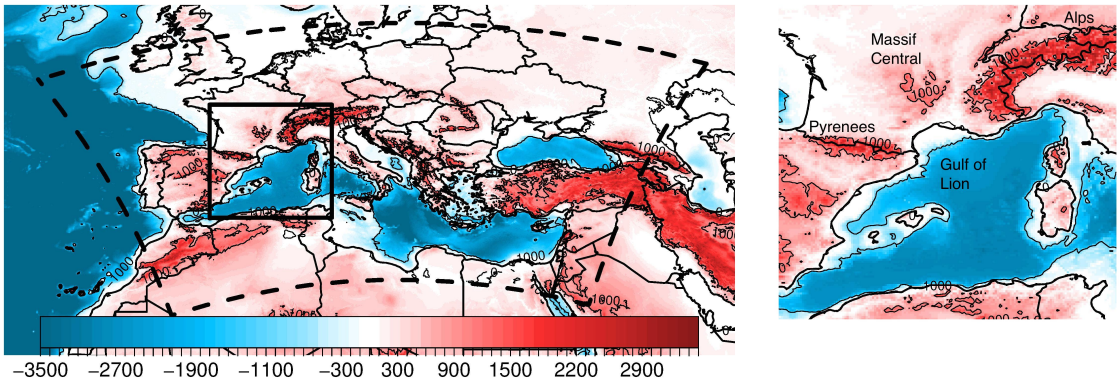

Figure 1.1.: Orography (m) of the Mediterranean region (left) and of the western Mediterranean basin (right) from ETOPO1 (Amante and Eakins (2009)) with Med-CORDEX area (Ruti et al. (2016), dashed lines) and enlarged area (full lines).

The densely populated Mediterranean region experienced a sequence of humid/dry and warm/cold periods in last thousands of years, including the Medieval Climate Anomaly and the Little Ice Age and is assumed to be one of the primary hotspots of climate change (Giorgi (2006); Diffenbaugh and Giorgi (2012)). Therefore, knowledge of the regions past and future climate are not only of large interest for archeology, history, and social science but also for climate adaption and mitigation studies. Such knowledge is acquired by natural climate archives and observations in combination with climate simulations.

Climate simulations require models, which simulate the time evolution of the atmosphere, ocean, and other parts of the climate system. Global circulation models (GCMs)

span the whole globe using a three-dimensional grid with a horizontal resolution of hundreds of kilometers. A system of differential equations based on the basic laws of physics is solved for each grid cell. Fine-scale structures and small-scale physical processes which occur inside a grid cell need to be parameterized or averaged.

The Mediterranean region shows a spatially non-uniform environment. Temperate, arid and snow climate exist in close distances, ranging from deserts to glaciers and from maritime to steppe (Lionello et al. (2012)). This variety of landscapes, with many islands of different sizes, straits, mountain ridges, and basins makes it a challenging area for climate simulations. To gain information in geographical regions with small structures compared to the global scale the resolution of the model has to be increased.

Like a magnifying glass for climate simulations, regional climate models (RCMs) simulate the climate system of a particular area with higher resolution (e.g., the Med-CORDEX area, Figure 1.1). RCMs consist of the same differential equations as GCMs. Since RCMs do not span the whole globe, but only part of it, the so-called boundary conditions must be prescribed at the borders of the modeling domain. This boundary data usually comes from GCMs. The process of refining the results of GCMs by RCMs is called dynamical downscaling.

Downscaling activities are coordinated using a joint experimental framework, the coordinated regional climate downscaling experiment CORDEX (Giorgi and Gutowski (2015), www.cordex.org). The Mediterranean part of CORDEX is the Med-CORDEX framework (Ruti et al. (2016), www.medcordex.eu). It aims at understanding processes responsible for climate variability and trends in the Mediterranean region, and, therefore, increase the reliability of past and future climate information.

As in other places in the world, wind speed, wind direction, and wind gust are among the main quantities of interest for people living in the Mediterranean area, because they influence their life most directly in conjunction with temperature and precipitation. In ancient times, the prevailing wind and ocean currents were vital for establishing trade routes over the Mediterranean Sea. Nowadays, wind information is also relevant for, e.g., fire and gust risk evaluation, forecasting wind energy production, and leisure sailors. Located in the zone of westerly winds, the Mediterranean Region shows many local wind phenomena as well. Along with the diverse orography of the region goes a variety of wind systems from land and sea breezes at its shore, through funneling in valleys and straits to blocking by mountain ranges.

Figure 1.2 shows some of the local Mediterranean wind systems. The Etesians dominate the eastern Mediterranean in summer, Bora is prevailing in the Adriatic area, and Sirocco comes from northern Africa during fall and spring. Ghibli and Khasim are hot and dusty desert winds blowing from Africa over the Mediterranean Sea. Cierzo,

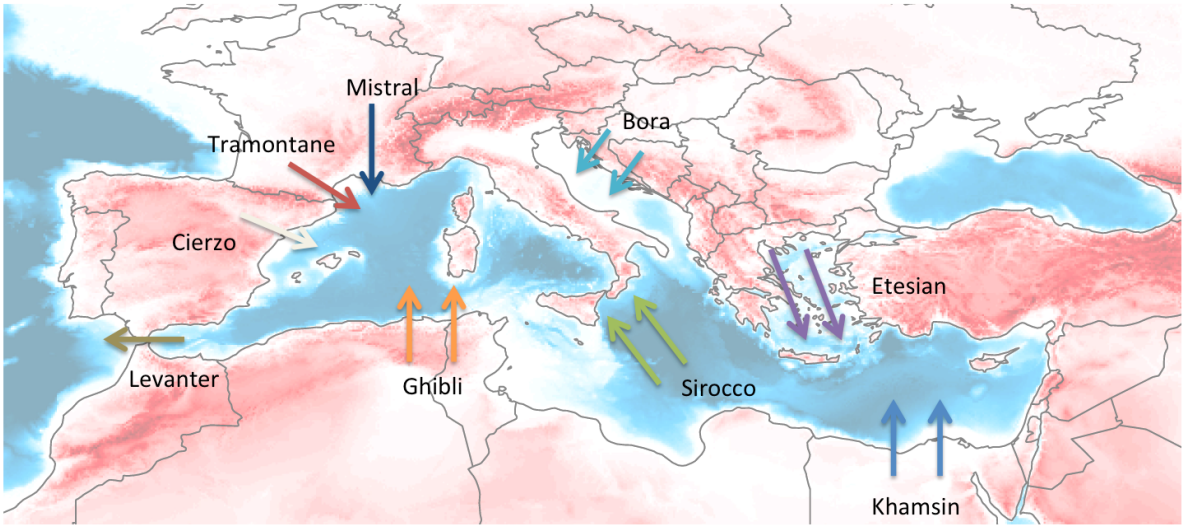

Figure 1.2.: Mediterranean wind systems (adapted from Lionello et al. (2006); Reiter (1975)).

Tramontane, and Mistral occur mainly during autumn and winter in the Ebro, Aude, and Rhône Valley, respectively (Reiter (1975)).

Mistral and Tramontane are the dominant wind systems in the western Mediterranean Region (right panel of Figure 1.1). Since similar large-scale pressure patterns cause Mistral and Tramontane in conjunction with the local orography, they often co-occur (Georgelin et al. (1994); Guenard et al. (2005)). They are most likely to happen in winter (Jacq et al. (2005)). Mistral passes through the Rhône Valley between the Alps and Massif Central from north to south, while Tramontane emerges in the Aude Valley between Pyrenees and Massif Central. In the constricting valleys, they accelerate before they reach the Mediterranean Sea at the Gulf of Lion.

Due to high wind speeds, Mistral and Tramontane can cause damage to structures (Smith (2015); Parish (2015)). They bring dry air and thus can accelerate ground drying during summer, which increases the fire risk (Guenard et al. (2005); Pugnet et al. (2013)). Furthermore, Mistral influences the transport of pollutants to and from southern France (Corsmeier et al. (2005); Guenard et al. (2005)) and was found to be related to heavy precipitation events (Berthou et al. (2014, 2015)). Accurate simulation of wind speeds is essential for assessing the risk of damage from vigorous winds, evaluating possible sites for wind energy production, and many other purposes.

The northern dry and cold winds cause evaporation in the area, especially in winter (Mariotti et al. (2002)). By advecting cold air over the western Mediterranean Sea, Mistral and Tramontane cause deep water formation (Schott et al. (1996); Marshall and Schott (1999); Béranger et al. (2010); Somot et al. (2016)), which makes them

crucial drivers also for ocean circulation (Schott et al. (1996); Béranger et al. (2010)). They connect to vortices, which occurred in the Gulf of Lion after episodes of high wind speeds (Allou et al. (2010)). Hence, Mistral and Tramontane are of great interest for studies on model evaluation and improvement.

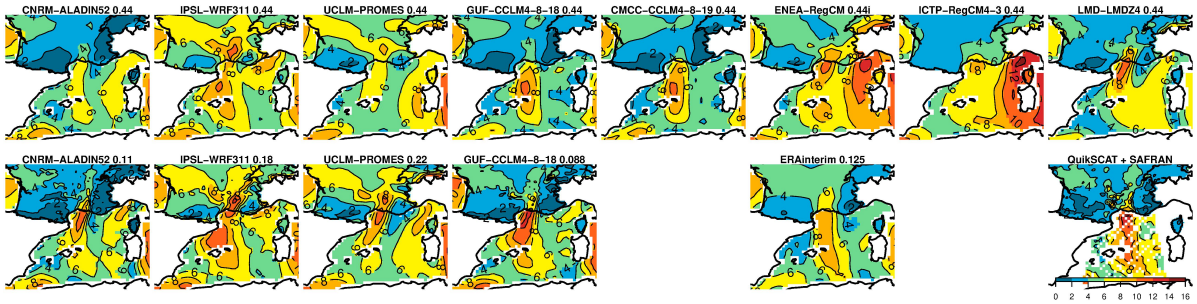

Figure 1.3.: Daily mean wind speed (m/s) on 24th March, 2002 optained from Med-CORDEX RCMs (Ruti et al. (2016), www.medcordex.eu), ERA-Interim (Dee et al. (2011)), QuikSCAT (Lungu et al. (2006)), and SAFRAN (Vidal et al. (2010); Quintana-Seguí et al. (2008)).

Furthermore, a reliable representation of those winds is desirable for risk assessment, which motivated this work. Figure 1.3 shows the daily mean wind speed for a Mistral event taken from several Med-CORDEX RCMs, reanalysis, and observational datasets. Differences between simulated and observed wind speeds are apparent. Moreover, there is some variation between the models.

This thesis focuses on the representation of Mistral and Tramontane in climate simulations. Starting from observational data and simulation results from RCMs of the MedCORDEX framework, the ability of climate simulations to simulate Mistral and Tramontane on the correct dates is assessed. Second, the observed and simulated wind speed and wind direction patterns are compared. The results of this surveys lead to the next question: Which factors determine the Mistral and Tramontane representation in simulations? Finally, the future evolution of Mistral and Tramontane is studied in climate projections. Figure 1.4 summarizes the four main research questions this thesis is targeting to answer and links them to the contributing publications.

The next chapter discusses the processes which determine the occurrence and characteristics of Mistral and Tramontane. Chapter 3 presents the database of this thesis, including observations from satellites, stations, and buoys, reanalysis data sets and data from 5 GCMs and 6 RCMs. The methods used are presented in chapter 4. Chapter 5 presents the results and discussion. The last section gives an outlook.

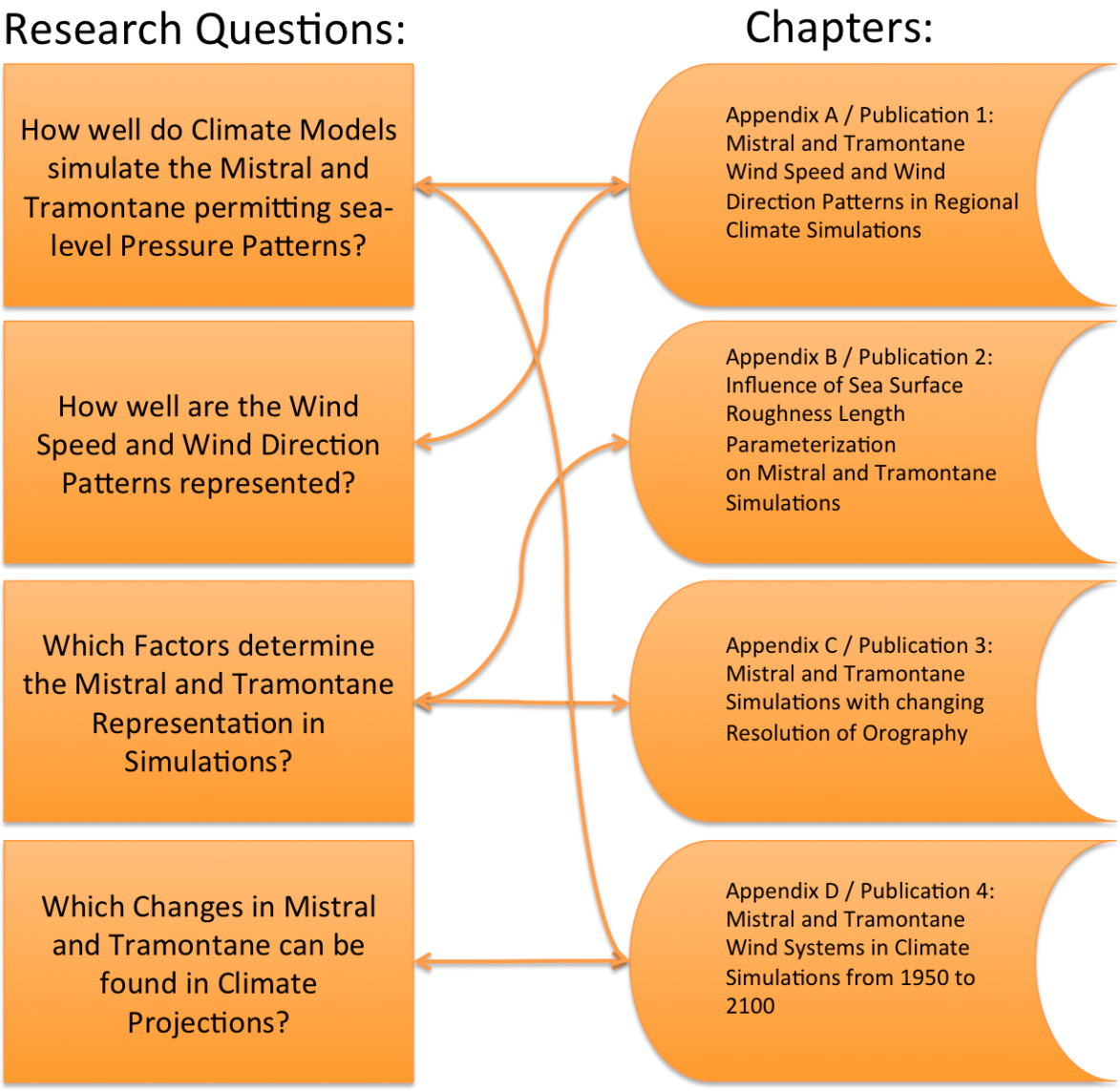

Figure 1.4.: Flowchart of this thesis.

2. Theoretical Background

Numerous factors influence Mistral and Tramontane, ranging over several spatial scales from the large-scale pressure patterns to the local surface friction. Funneled in inclined valleys, they show characteristics of both gap flows and downslope flows (Lionello et al. (2012); Ulbrich et al. (2012)). Further effects and processes connected to Mistral and Tramontane are, i.a., the Coanda effect (Giles (1977)), the flow through a mountain gap (Gaberšek and Durran (2004, 2006)), hydraulic jumps (Drobinski et al. (2001, 2005)), and the interaction with sea breeze (Simpson (1994), Bastin et al. (2006)). This chapter discusses the processes and effects relevant for modeling of Mistral and Tramontane events.

2.1. Large Scale Flow

During a Mistral event, air accelerates along the Rhône Valley between the Alps and Massif Central (Figure 2.1). In the case of Tramontane, the acceleration happens along the Aude Valley between Massif Central and Pyrenees. Like other fluids, air on large spatial scales moves from areas of high pressure to areas of low pressure. Such a pressure gradient causes Mistral and Tramontane to enter the valleys. Figure 2.1 shows the simulated surface wind and sea-level pressure for the morning of 24th March, 2002. The data comes from ERA-Interim (Dee et al. (2011)), a reanalysis product discussed in detail in Chapter 3. On that day, a pressure gradient was present along the Rhône Valley and an accelerating Mistral flow established in the valley.

Several synoptic situations can lead to such a pressure gradient along the valleys. High pressure above the bay of Biscay, sometimes a low about central Europe, and a low-pressure system in the Gulf of Genoa occurring at the same time lead to a pressure gradient which favors Mistral and Tramontane events (Jacq et al. (2005)). Mistral also has been described as a wind channeled in the Rhône Valley, caused by cyclogenesis in the Gulf of Genoa, in conjunction with a trough passing through France (Drobinski et al. (2005)). Blocking of airflow also is discussed as the reason for Mistral and Tramontane to occur. If the Alpine range blocks a north-westerly flow a cold air reservoir forms,

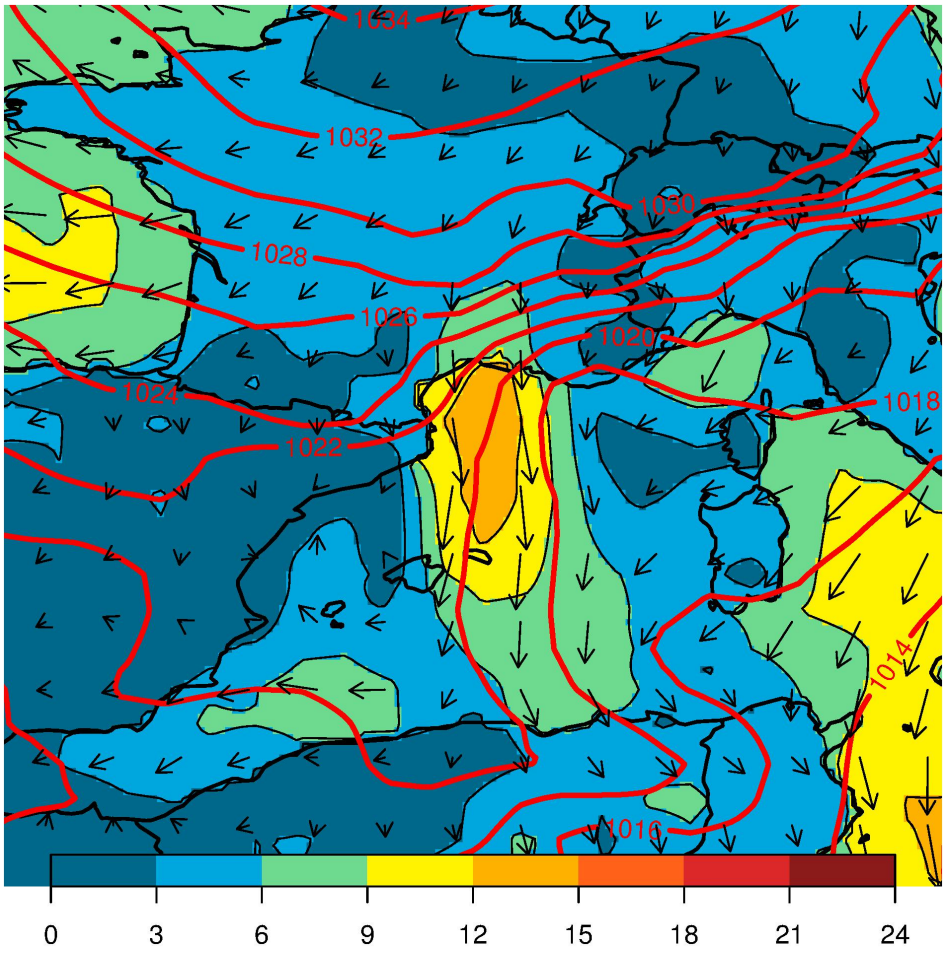

Figure 2.1.: Wind speed, direction and sea-level pressure from ERA-Interim on 24th March, 2002.

which then accelerates as Mistral in the Rhône Valley (Barry (2008)). At the same time, a lee cyclone develops in the Gulf of Genoa (Guenard et al. (2005)).

For a fluid with density ρ, the pressure gradient $\vec{\nabla}p$ causes an acceleration $\vec{a}_p = -\frac{\vec{\nabla}p}{\rho}$. The resulting pressure-gradient force $\vec{F}_p$ on a fluid parcel of mass m is given by

$$\vec{F}_p = m \cdot \vec{a}_p = -\frac{m}{\rho}\vec{\nabla}p \tag{2.1}$$

If the motion of the air is described in earth following coordinates or other non-inertial frames of reference inertial forces are apparent. Centrifugal force and Coriolis force are the most important of these. In a rotating system with angular velocity $\vec{\omega}$, a moving body with velocity $\vec{v}$ experiences the Coriolis acceleration $\vec{a}_c$. The Coriolis force $\vec{F}_c$ is

given by

$$\vec{F_c} = m \cdot \vec{a}_c = 2m \cdot (\vec{v} \times \vec{\omega}) = -2m \cdot v \cdot \omega \cdot \sin(\phi) \cdot \vec{n} \tag{2.2}$$

With ω the angular speed and the latitude ϕ, the Coriolis force points in the direction of unity vector $\vec{n}$, perpendicular to $\vec{v}$ and $\vec{\omega}$ and, therefore, is always perpendicular to the wind vector. In the northern hemisphere it leads to a right hand deflection of the wind. The quantity $f = 2\omega \sin(\phi)$ is called the Coriolis parameter. It varies with latitude and its typical value in the Mistral and Tramontane area is $f \approx 10^{-4}$/s.

Together with the pressure-gradient force, the Coriolis force provides the components for the so-called geostrophic wind, which travels parallel to isobars. In the Mistral case shown in Figure 2.1, the wind direction over the Mediterranean Sea is almost parallel to the isobars. Indeed, Mistral was found to be in quasi-geostrophic balance over parts of the Mediterranean Sea (Drobinski et al. (2017)). Geostrophic wind is a good assumption for large-scale flows in the mid-troposphere at mid-latitudes. However, due to other forces, the actual wind usually differs from the geostrophic wind.

2.2. Planetary Boundary Layer

Mistral and Tramontane occur in relatively close distance to the ground. In contrast to geostrophic winds in higher levels of the atmosphere, the friction force and, therefore, the properties of the surface become relevant for calculating the wind speeds. The layer of the atmosphere that is directly influenced by the roughness and energy balance at the surface is called planetary boundary layer (PBL). Both the topography and the surface cover influence the PBL (Finnigan (2015)).

In the layer closest to the surface, the flow is in local equilibrium with the surface. Above the equilibrium layer, the wind speed increases until it reaches the wind speed of the free atmosphere at $z = \delta_i$. The roughness length z_0 is about 10–30 % of the height of roughness elements (e.g., buildings, crops) on the ground. Displacement height d is the height above the ground below which the wind speed is zero m/s due to obstacles. It usually corresponds to about 60 % of the obstacle height.

The logarithmic wind profile is

$$\bar{u}(z) = \frac{u_*}{\kappa} \ln\left(\frac{z-d}{z_0}\right) \tag{2.3}$$

with roughness length z_0, displacement height d, κ von Karman's constant, and friction velocity $u_* = \sqrt{\tau_0}$, which is the square root of the kinematic surface stress τ_0. The surface wind parameterizations in atmospheric models depend on the surface roughness length z_0. Land use and the annual cycle of vegetation determine its value.

Figure 2.2 shows how the wind profile $\bar{u}(z)$ will adjust to new surface properties if the surface roughness and displacement height change. Diffused vertically by turbulence, the new internal boundary layer grows to depth $\delta_i(x)$. At the bottom of the internal boundary layer, an inner equilibrium layer $\delta_e(x)$ develops, in which the flow achieves equilibrium with the new surface.

The orography influences many mesoscale wind systems. In the case of Mistral and Tramontane, the orography causes the channeling, and, therefore, the acceleration in valleys. Since climate simulations run on a numerical grid, orographic features on smaller scales than the grid resolution cannot be regarded directly in the calculations. This subgrid-scale orography (SSO) has to be parameterized. Thus, the values for mean elevation, standard deviation, anisotropy, mean angle, and mean slope are calculated from a high-resolution orography data set for each grid point (Lott and Miller (1997)). During the calculation of the surface momentum fluxes, an additional term is added to increase the surface drag if subgrid-scale orography is present.

When reaching the Mediterranean Sea, the wind speed of Mistral and Tramontane increases, due to the decrease of surface roughness over water compared to the land

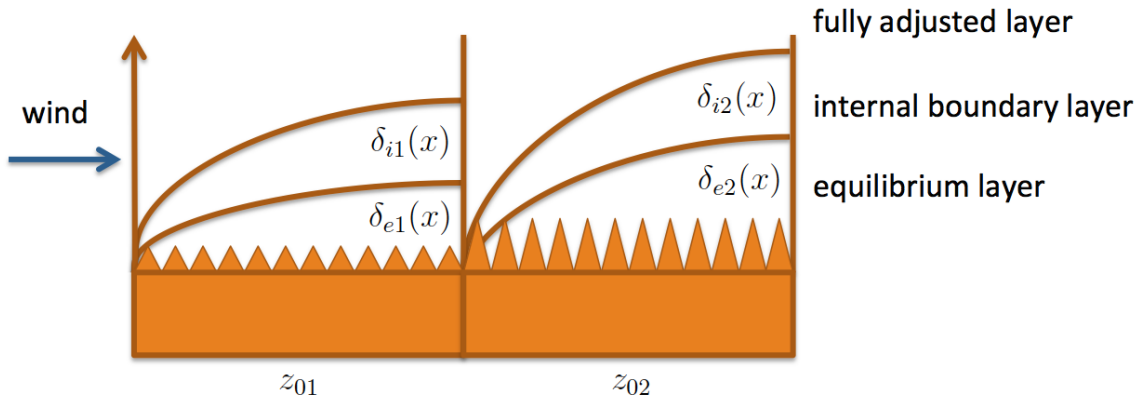

Figure 2.2.: Change in flow structure with changing surface roughness z_{0i} (adapted from Finnigan (2015)).

surface roughness. Over the sea surface, the roughness length depends on the waves, which in turn were partially generated by winds. Charnock (1955) proposed a still widely used parameterization

$$z_0 = \frac{\alpha}{g} u_*^2 \tag{2.4}$$

In this equation, z_0 depends on gravity constant g, Charnock parameter α and the friction velocity u_*, which is calculated from surface momentum fluxes and density. A complete description of the ocean-atmosphere interaction and, therefore, the sea surface roughness, also should account for ocean currents, waves, and interaction between these phenomena (Carniel et al. (2016); Ricchi et al. (2016)).

2.3. Downslope Winds

Air which moves down a topographic incline, e.g., a mountainside, or in the case of Mistral and Tramontane an inclined valley, is called a fall wind or downslope wind. The air of the wind can be either colder (e.g., for Mistral, Tramontane, and winds over the Antarctic and Greenland ice shields) or warmer (e.g., for Föhn in the Alps and Chinook in North America) than the replaced air. Until the middle of the 20th century, the term katabatic was most commonly used for Föhn type winds. Over time, the use of katabatic changed and nowadays refers to cold winds (Parish (2015)).

Besides Mistral and Tramontane, other examples for katabatic winds are the Bora which descends from the Carpathian Mountains and the Alps to the shores of the Adriatic Sea and the Oroshi at the Pacific side of the mountain ranges in Japan. Many more wind systems of this type have been observed ranging over all latitudes (Parish (2015)).

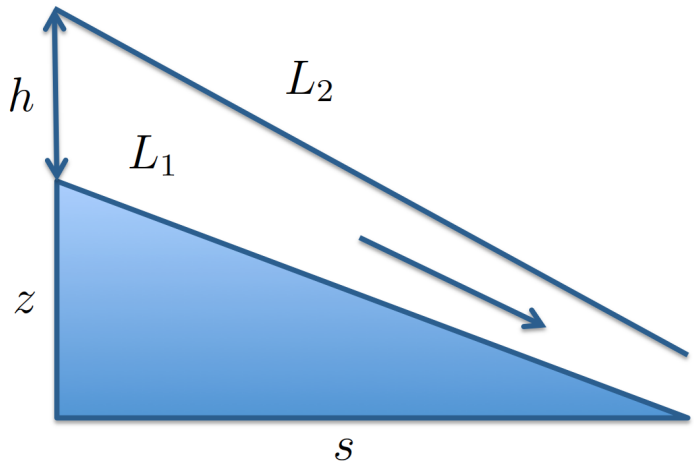

Figure 2.3.: Accelerating downslope flow in a two-layer fluid with cold layer L_1 and undisturbed ambient atmosphere layer L_2 (adapted from Parish (2015)). z indicates terrain height, h is the depth of layer L_1 and s is the horizontal length scale.

Figure 2.3 shows a cross-sectional view of a two-layer downslope flow. A downslope wind is driven by gravity because the air of the downslope flow (L_1) with depth h is denser than the air it replaces (L_2). Due to compression, the air in L_1 experiences adiabatic warming during downslope movement. In Figure 2.3 shows a situation with accelerating flow and, therefore, with decreasing h. This acceleration and decrease of h are not present in all cases of downslope flows.

The horizontal pressure gradient Δp depends on the temperatures $T_{i=1,2}$ and densities $\rho_{i=1,2}$ of the cold lower layer L_1 and the undisturbed layer L_2 as well as the terrain

height z and the depth of the lower layer h. Both height coordinates vary with the horizontal coordinate s. The pressure difference along the variation of s is

$$\Delta p = g\frac{\Delta T}{T_1}\left(\frac{\delta z}{\delta s} + \frac{\delta h}{\delta s}\right) - \frac{1}{\rho_1}\frac{\delta p}{\delta s} \tag{2.5}$$

The first term is the buoyancy force term, which depends on the temperature difference over sloping terrain. The second term depends on the thickness of the lower layer L_1 and often is neglected for horizontal scales larger than a few km. The third term is the pressure gradient force in the atmosphere above the cold layer L_1.

Figure 2.4 shows the force balance for downslope winds in the northern hemisphere. Here, the pressure gradient is assumed to be parallel to the inclination, and therefore the resulting acceleration due to gravity is parallel to the inclination as well. The stronger the pressure gradient becomes, the more the angle between wind vector $\vec{v}$ and $\vec{F}_p$ decreases. This description of downslope winds helps to understand part of the acceleration of Mistral and Tramontane. The other part of the acceleration is due to the constriction of the valleys. The Rhône Valley has a slope of about 2.5 % (Barry (2008)).

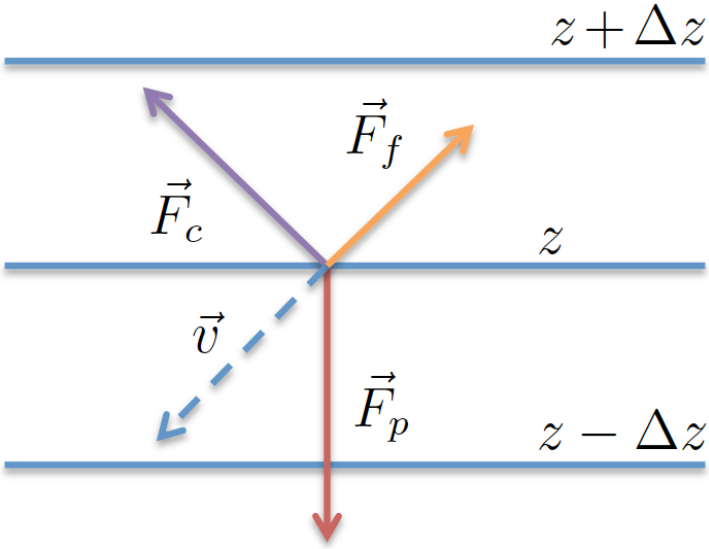

Figure 2.4.: Force balance for downslope winds on the northern hemisphere (adapted from Parish (2015)). $z + \Delta z$, z, and $z - \Delta z$ are isolines of terrain height, $\vec{F}_c$ denotes Coriolis force, $\vec{F}_p$ is the pressure gradient force, and $\vec{F}_f$ is the friction force. $\vec{v}$ is the resulting wind vector.

2.4. Gap Winds

Besides being treated as downslope winds, Mistral and Tramontane both are gap winds. This type of wind occurs in mountain gaps, valleys, and marine straits. In the valley, approximate geostrophic balance develops in the cross gap direction between the cross-gap pressure gradient force and the Coriolis force associated with the along-gap flow (Overland (1984)). In the along-gap direction, a balance between pressure gradient and inertial accelerations develops, while friction force and entrainment limit the along-gap wind speed (Barry (2008)).

Mistral travels from north to south in the Rhône Valley between Alps and Massif Central, while Tramontane follows the Aude Valley between Pyrenees and Massif Central. Both winds experience channeling and acceleration in the constricting valleys. Assuming the wind is an incompressible fluid with density ρ, the flow follows Bernoulli's principle. Along all points of a streamline, the air then obeys the energy conservation equation

$$E_m = \alpha\frac{v^2}{2} + gz + \frac{p}{\rho} = const \tag{2.6}$$

with acceleration due to gravity g, energy E_m, speed v, elevation z, pressure p, and the kinetic energy factor α (Cimbala and Çengel (2008)).

The Venturi effect describes the pressure reduction at a constriction in a fluid. Along a streamline of the fluid with constant density ρ, the change in pressure between a wider area of the valley (with fluid speed v_1 and cross section A_1) and a narrow area (v_2 and A_2) is given by

$$p_1 - p_2 = \frac{\rho}{2}\left(v_2^2 - v_1^2\right) \tag{2.7}$$

The volumetric flow rate Q is the volume of an incompressible fluid, which passes per unit time and gives a relation of the wind speed to the diameter of the pipe/change in valley width:

$$Q = v_1 A_1 = v_2 A_2 \tag{2.8}$$

The Mistral accelerates downstream of Valence, where the constriction is located (Barry (2008)). Garcia (2014) surveyed the acceleration and deceleration of Mistral flow in a simple pipe model with friction at the ground of the valley and could reproduce the observed changes in wind speed along the Mistral flow including the acceleration at the constriction and deceleration at the valley opening.

After exiting the valley, an air parcel follows an inertial path with a radius of curvature $R_c = -v/f$ with wind speed v, and Coriolis parameter f. If a low-level jet emerging

from a gap is tangential to a convex surface, it may remain attached to that surface for some distance downstream, despite the increasing deflection of the flow (Barry (2008)). This phenomenon is the Coandă or wall attachment effect, which probably causes Mistral to stay attached to the Alps when reaching the exit of the Rhône Valley. Less air is available for entrainment at the Alpine side of the Mistral flow, as a consequence, a low-pressure area emerges, and the Mistral is attracted to the Alps (Figure 2.5 a-c). This effect is assumed to be present in the Carpathian Mountains and the Transylvanian Alps as well (Giles (1977)).

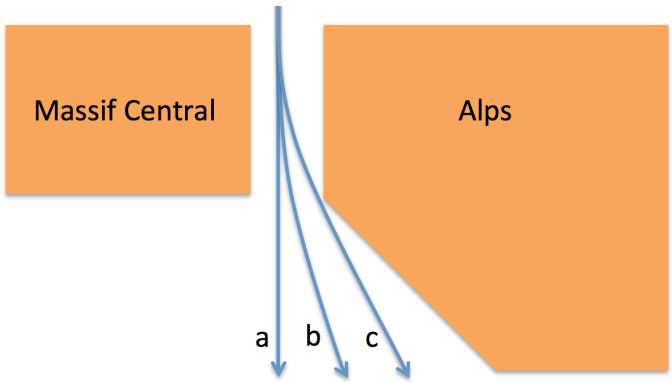

Figure 2.5.: Mistral affected by Coandă effect. The northerly flow (a) moves closer to the Alpine mountain range (b, c) (adapted from Giles (1977)).

2.5. Hydraulic Jumps

At some locations in low-level jets, a drop in wind speed might occur together with an increase of the wind layer depth. These so-called hydraulic jumps are due to the transition from a tranquil fast flow to a slower turbulent flow regime (Cimbala and Çengel (2008)). Figure 2.6 shows a schematic of a hydraulic jump.

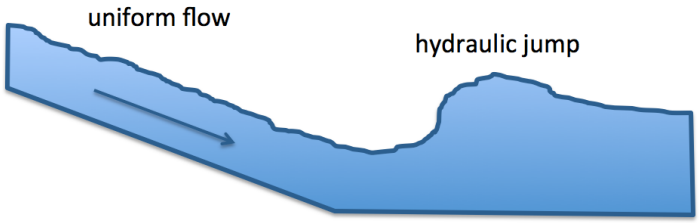

Figure 2.6.: Hydraulic jump schematic (adapted from Cimbala and Çengel (2008)).

Hydraulic jumps of Mistral occur where the Rhône Valley widens (Drobinski et al. (2005)) and downstream of a hill close to the coast in Tramontane (Drobinski et al. (2001)). Figure 2.7 shows the approximate location of the hydraulic jumps. A hydraulic jump in the lee of Mount Lozére, a mountain in the southern Massif Central causes a wake which separates Mistral and Tramontane (Guénard et al. (2006))

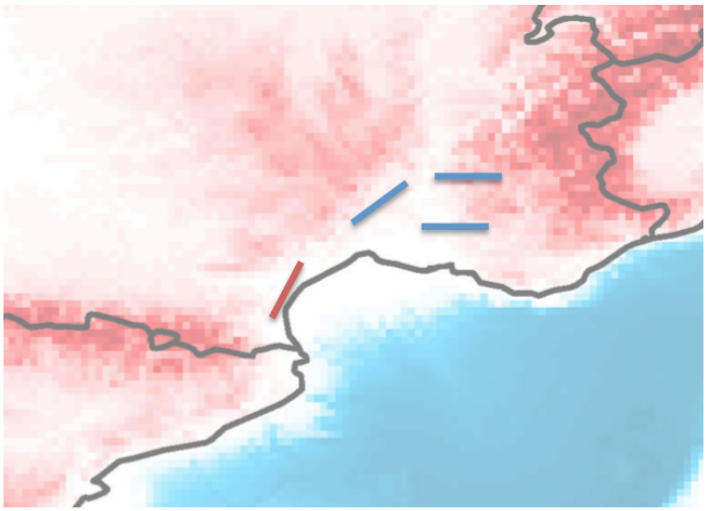

Figure 2.7.: Locations of observed hydraulic jumps of Mistral (blue) and Tramontane (red) (adapted from Drobinski et al. (2001, 2005)).

3. Data

The evaluation of climate models relies on observation data. Observations are done either in-situ (i.a., at surface stations) or remotely (e.g., using satellites). This chapter introduces the database of this work, which includes surface observation and scatterometer data, as well as reanalysis products. Furthermore, the five global circulation models and six regional climate models used in this thesis are presented.

3.1. Observational Datasets

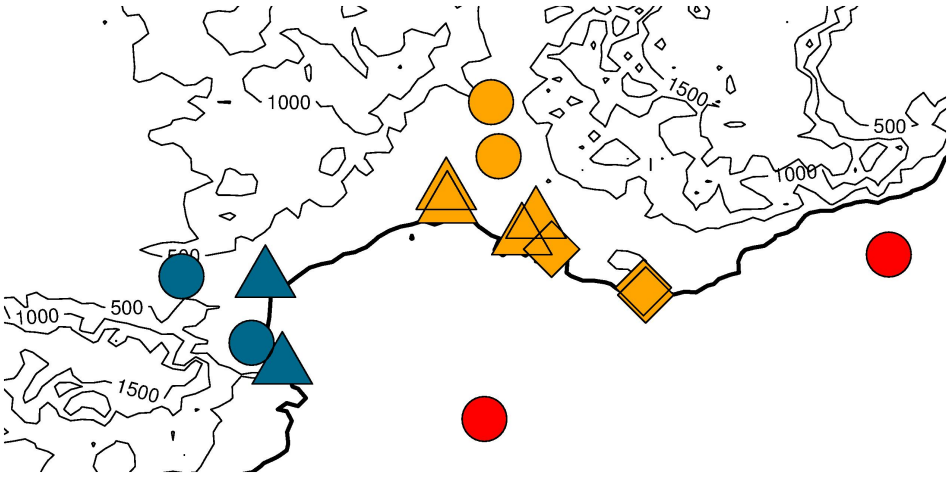

Figure 3.1.: Location of stations in Mistral area (orange symbols), Tramontane area (blue symbols) and buoys (red circles). Thick black line indicates coastline.

3.1.1. Station Data

Daily gust time series are available from 13 stations in the Mistral and Tramontane region. The time series includes the information, if gusts greater than 16 m/s from the dominant Mistral/Tramontane wind direction occurred for each day in 1981–2010. The

Data was provided by V. Jacq, Météo-France (Jacq et al. (2005); Jacq (2011)). Figure 3.1 shows the location of the surface stations. A description of the station locations and corresponding wind directions can be found in Tables 3.1 and 3.2. In this thesis, the station gust observations are used to create a reference time series of Mistral and Tramontane days.

Table 3.1.: Stations in the Mistral Area.

Station Name	Longitude (°E)	Latitude (°N)	Direction of Gusts (°)
Valley stations			
Montélimar	4.75	44.56	320–040
Orange	4.81	44.14	320–030
Plains stations			
Nimes-Courbessac	4.40	43.86	320–040
Nimes-Garons	4.41	43.76	320–040
Istres	4.99	43.51	330–010
Salon	5.10	43.64	330–010
Coastal stations			
Marignane	5.22	43.42	330–010
Toulon	5.93	43.12	260–340
Cap Cepet	5.95	43.07	260–340

Table 3.2.: Stations in the Tramontane area.

Station Name	Longitude (°E)	Latitude (°N)	Direction of Gusts (°)
Valley stations			
Carcassonne	2.35	43.21	260–320
Perpignan	2.90	42.70	300–360
Coastal stations			
Cap Bear	3.13	42.52	300–360
Narbonne	3.00	43.18	260–320

Table 3.3.: Buoys in the Mistral and Tramontane area.

Buoy Name	Longitude (°E)	Latitude
Lion	4.7	42.1
Azur	7.8	43.4

3.1.2. Buoy Data

Two stationary buoys exist in the Mistral and Tramontane area. Table 3.3 lists their coordinates. The Lion buoy is located in the Gulf of Lion, in the area where Mistral and Tramontane merge. The Azur buoy is placed close to the French-Italian border. Both buoys measure wind speed and wind direction every hour. Figure 3.1 shows the location of the buoys.

3.1.3. QuikSCAT

The QuikSCAT scatterometer data provides wind speed and wind direction information on a 25 km grid over the oceans for the period 1999–2009. The wind speed measurement accuracies are 2 m/s for wind speeds of 3–20 m/s and 10 % for wind speeds of 20–30 m/s. The corresponding value for wind direction is 20° (Lungu et al. (2006)). Since the satellite is in a polar orbit, the data was retrieved twice a day, at about 6 a.m. and 6 p.m. local time. Due to the satellites swath, each day only part of the western Mediterranean area is observed (see, e.g. in Figure 1.3).

In this thesis, the simulated daily wind speeds from RCMs are evaluated using the average of the two QuikSCAT measurements for each day. Figure 3.2 shows the resulting numbers of QuikSCAT observations in 2000-2008. Close to the shore, only a few observations are available, which limits the information on the wind in this area. Accadia et al. (2007) and Ruti et al. (2008) validated QuikSCAT winds with buoy observations. They found an overestimation of 0.4–0.9 m/s in QuikSCAT, with higher wind speeds showing a stronger deviation from buoy observations.

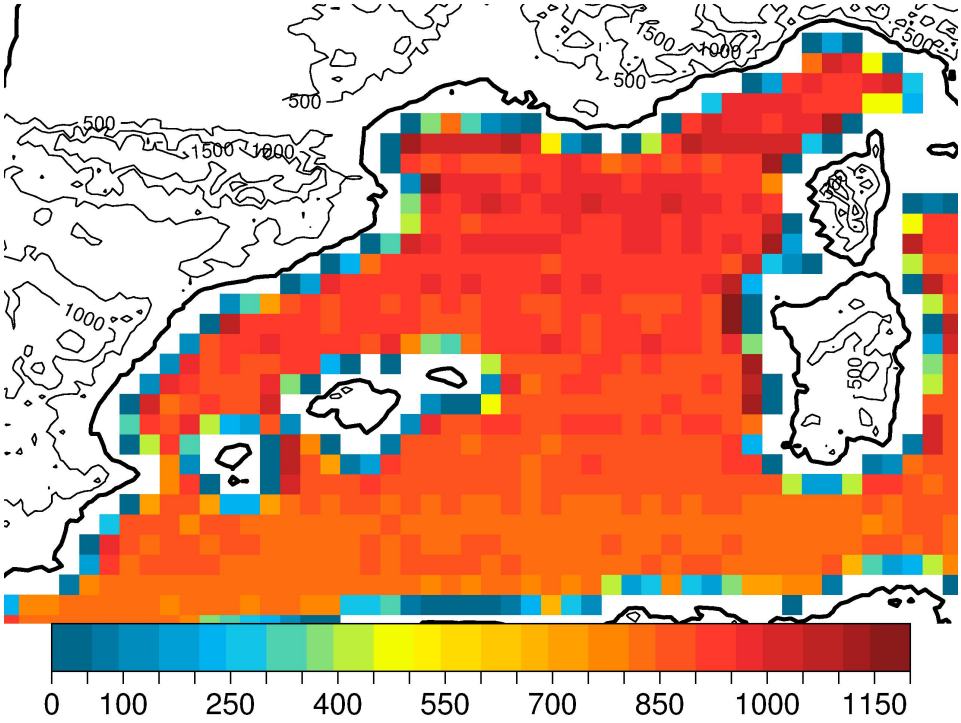

Figure 3.2.: Number of QuikSCAT observations.

3.2. Reanalysis Data

Reanalysis datasets consist of a model in combination with observations. Both are combined using a data assimilation scheme leading to an analysis of the atmospheric state at a given time.

3.2.1. SAFRAN

Wind speed data from the "Système d'Analyse Fournissant des Renseignements Atmosphériques à la Neige" (analysis system to provide data for snow models, SAFRAN) on a 0.1° grid is used as a reference for evaluating the performance of RCMs regarding Mistral and Tramontane wind patterns over France. SAFRAN is a reanalysis product, consisting of a gauge based analysis system using an optimal interpolation method (Vidal et al. (2010); Quintana-Seguí et al. (2008)). Together with the QuikSCAT data, SAFRAN covers most of the Mistral and Tramontane area (Figure 1.3).

3.2.2. ERA-Interim

ERA-Interim is a reanalysis data set provided by the European Centre for Medium-Range Weather Forecasts (ECMWF). It is calculated on a 80 km grid from 1979 to today (Dee et al. (2011)). In this thesis, ERA-Interim sea-level pressure fields are used to identify patterns that favor Mistral and Tramontane events. Surface wind speed and direction data are used to evaluate the quality of wind pattern simulation. Furthermore, ERA-Interim is used to provide lateral boundary information for RCM simulations.

3.3. Climate Simulations

3.3.1. Global Circulation Models

Climate simulations require models, which simulate the time evolution of the atmosphere, ocean, and other parts of the climate system. Global circulation models (GCMs) span the whole globe using a three-dimensional grid with a horizontal resolution of about hundred kilometers. A system of differential equations based on the basic laws of physics is solved for each grid cell. Fine-scale structures and small-scale physical processes which occur inside a grid cell need to be parameterized or averaged.

Table 3.4 gives an overview of the GCMs evaluated in this thesis. The GCMs belong to the fifth phase of the Climate Model Intercomparison Project (CMIP5, Taylor et al. (2012)). Depending on the emission of greenhouse gases, several future states of the atmosphere are possible. This thesis focuses on two scenarios, the representative concentration pathways (RCPs) (Moss et al. (2010)) RCP4.5 and RCP8.5, which assume a radiative forcing of +4.5 and +8.5 W/m^2 in the year 2100 compared to the pre-industrial value. GCMs can be used either directly to do climate studies or to provide the lateral boundary conditions for regional climate models (RCMs). The RCMs can simulate the atmosphere of a particular area on denser grid spacing than the GCMs.

Table 3.4.: GCM simulations discussed in this thesis and modeling groups. Acronyms are explained in the text.

Name	Group
MPI-ESM-LR	MPI-M
CMCC-CM	CMCC
MPI-ESM-MR	MPI-M
HadGEM2-ES	MOHC/INPE
CNRM-CM5	CNRM-CERFACS

MPI-ESM

The Earth System Model MPI-ESM consists of the atmosphere component ECHAM6 (Stevens et al. (2013)) and the ocean component MPIOM (Jungclaus et al. (2013)). Simulations were done by the Max-Planck-Institut für Meteorologie (MPI-M) in two model configurations with low (LR) and medium (MR) resolution (Mauritsen et al. (2012); Giorgetta et al. (2013)).

CMCC-CM

The Centro Euro-Mediterraneo sui Cambiamenti Climatici (CMCC) Climate Model (CMCC-CM) comprises the atmosphere component ECHAM5, (Roeckner et al. (2003)) and the ocean component OPA 8.2 (Madec et al. (1997)). CMCC also did the simulations with CMCC-CM used in this thesis.

HadGEM2-ES

The Met Office Hadley Centre (MOHC) and Instituto Nacional de Pesquisas Espaciais (INPE) developed the earth system version of the Hadley Centre Global Environment Model version 2 HadGEM2-ES (Martin et al. (2011)).

CNRM-CM5

ARPEGE-climat v5.2 (Météo-France (2009)) and NEMO v3.2 (Madec (2008)) are the atmosphere and ocean components of CNRM-CM5 (Voldoire et al. (2013)). The Centre National de Recherches Météorologiques/Centre Européen de Recherche et Formation Avancée en Calcul Scientifique (CNRM-CERFACS) produced the simulations used here.

3.3.2. Regional Climate Models

The regional climate model (RCM) simulations evaluated in this thesis come from the Med-CORDEX framework (www.medcordex.eu), the Mediterranean part of the coordinated regional climate downscaling experiment (CORDEX, www.cordex.org). Med-CORDEX aims at understanding processes responsible for climate variability and trends in the Mediterranean region. RCMs including atmosphere, ocean, land surface and river models are used to increase the reliability of past and future climate information (Ruti et al. (2016)). The simulations were performed on the Med-CORDEX domain (Figure 1.1) on a 0.44° grid. Lateral boundary data came from the GCMs mentioned above and from ERA-Interim. For some of the models, a second simulation with a smaller grid spacing is available for the ERA-Interim period. Table 3.5 gives an overview of the RCM simulations evaluated in this thesis.

ALADIN

The Centre National de Recherches Météorologiques (CNRM) performed the ALADIN 5.2 simulations used in this thesis (Colin et al. (2010); Herrmann et al. (2011)). The ERA-Interim driven runs are available on two resolutions (0.44° and 0.11°). CNRM provided the simulations driven by CNRM-CM5 for RCP4.5 and RCP8.5.

WRF

The National Center for Atmospheric Research (NCAR) developed the Weather Research and Forecasting (WRF) model (Skamarock et al. (2008)). The Institut Pierre Simon Laplace (IPSL) performed simulations on 0.44° and 0.18° grids driven by ERA-Interim data using WRF 3.1.1.

PROMES

Universidad de Castilla-La Mancha (UCLM) developed the RCM PROMES (Domínguez et al. (2010)). This study includes two ERA-Interim driven simulations with PROMES. They were performed by RCLM on 0.44° and 0.22° grids.

COSMO-CLM

Simulations with the COSMO-CLM (CCLM) model (Rockel et al. (2008)) were performed by Goethe Universität Frankfurt (GUF) with CCLM 4-8-18 and by Centro EuroMediterraneo sui Cambiamenti Climatici (CMCC) with CCLM 4-8-19. For both setups, simulations on 0.44° grids with ERA-Interim and GCM lateral boundaries are available. An additional ERA-Interim driven simulation on a 0.088° grid is available from GUF.

Sensitivity tests with GUF-CCLM 4-8-18 on the surface roughness parameterization were done on a simulation domain of 1140 $\times$ 800 km^2 on a 0.088° grid encompassing Southern France and a large part of the western Mediterranean Sea. The simulation covers the year 2005 using boundary data from an ERA-Interim driven GUF-CCLM 4-8-18 simulation on a 0.088° grid. One way nesting with three boundary lines (i.e. about 30 km) was used. The boundary data were updated every three hours and interim time steps were linearly interpolated (Edelmann (2015)).

Chapter 4 gives details on the simulation strategy of idealized COSMO-CLM 5-7 simulations done within the scope of this thesis.

RegCM4-3

The International Center for Theoretical Physics (ICTP) performed a simulation with RegCM4-3 (Giorgi et al. (2012)) with ERA-Interim as driving data. Two other simulations with RegCM4-3 were using MPI-ESM-MR and HadGEM2-ES boundary information. The Agenzia nazionale per le nuove tecnologie, l'energia e lo sviluppo economico sostenibile (ENEA) also did a simulation with RegCM4-3 and ERA-Interim boundary data.

LMDZ

Laboratoire de Météorologie Dynamique (LMD) developed the LMDZ4 model (Hourdin et al. (2006)) and performed simulations for ERA-Interim lateral boundaries. The Z in LMDZ stands for the models' ability to zoom, enabling it to perform both global and regional climate simulations.

Table 3.5.: RCM simulations and forcing data used in this thesis.

RCM	Group	ERA-Interim	GCM	historical	RCP 4.5	RCP 8.5
ALADIN52	CNRM	1979–2011	CNRM-CM5	1950–2005	2011–2100	2006–2100
WRF3.1.1	IPSL	2000-2008				
PROMES	UCLM	2000-2008				
CCLM4-8-18	GUF	1979–2011	MPI-ESM-LR	1949–2005	2006–2100	2006–2100
CCLM4-8-19	CMCC	1979–2012	CMCC-CM	1950–2005	2006–2100	2006–2100
RegCM4-3	ENEA	2000-2008				
	ICTP	1979-2008	MPI-ESM-MR	1970–2004		2007–2099
			HadGEM2-ES	1970–2005	2006–2098	2006–2098
LMDZ4	LMD	2000-2008				

4. Methods

This chapter describes the methods used to derive Mistral and Tramontane time series and the classification algorithm. Furthermore, it presents the procedures for idealized simulations and the evaluation methods.

4.1. Time Series of observed Mistral and Tramontane Events

To compare simulations and observations of Mistral and Tramontane events, days on which both wind systems occurred, had to be identified. The gust time series in the Mistral and Tramontane area were combined to determine days with a contiguous Mistral and Tramontane flow. Each station belongs to one of five geographical regions (3 for Mistral, Table 3.1 and 2 for Tramontane, Table 3.2). A Mistral day occurred when at least one station in each of the three areas (valley, plains, and coast) showed gusts on that day. On a Tramontane day, the gusts had to emerge at one coastal station and one station located in the Aude Valley. Table 4.1 gives the percentage of days on which Mistral and Tramontane occurred according to the combined station time series.

Table 4.1.: Observed percentage of Mistral and Tramontane days in 1981–2010.

1981–2010	Tramontane	No Tramontane	Sum
Mistral	12.6	3.4	16.0
No Mistral	19.4	64.6	84.0
Sum	32.0	68.0	100

4.2. Classification Algorithm for sea-level Pressure Patterns

A classification algorithm, which measures the quality of simulated sea-level pressure fields, was developed. It is based on an empirical orthogonal function (EOF) analysis (von Storch and Zwiers (2001)) and a Bayesian network (Scutari (2010)) to identify sea-level pressure patterns which are likely to produce a Mistral and Tramontane flow. This thesis includes results from two configurations of the classification algorithm (Table 4.2). Configuration A included 100 EOFs and nine years of training data. For the second configuration used, configuration B, 50 EOFs and 30 years of data were employed.

Optimized for evaluation of Mistral and Tramontane patterns with observation data as the reference, Configuration A has a high accuracy in identifying Mistral and Tramontane events in the years 2000–2008. With its longer training period, configuration B performs better in the classification of longer time series, e.g., projection simulations. In tests with different numbers of EOFs, these settings reached the highest accuracy. The following sections describe the general structure of the classification algorithm. Appendices A.4.2 and D.3 give a detailed description of the two configurations.

Table 4.2.: The two configurations of the classification algorithm.

Configuration	A	B
Number of EOFs	100	50
Training period	2000–2008	1981–2010
Training period length (years)	9	30

4.2.1. EOF Analysis

An EOF analysis was applied to the ERA-Interim daily mean sea-level pressure fields of the training period in the area –20–20° E and 25–55° N. The sea-level pressure fields of the simulations were also projected on the ERA-Interim EOFs. The resulting principal components indicate how much each EOF contributes to the sea-level pressure field on a given day.

The first EOF explains a large part of the observed variance, while the succeeding EOFs explain a decreasing part of the variance. The first EOF of the ERA-Interim data set shows a high-pressure system over England. The second and third EOF show dipole patterns, while the fourth and fifth EOF already show quadrupole patterns.

4.2.2. Training of the Bayesian Network

The Bayesian network was trained with the observed Mistral and Tramontane time series and the ERA-Interim principal components using a hill-climbing algorithm (Tsamardinos et al. (2006)). The training algorithm identifies connections between principal components and the presence of a Mistral and Tramontane event. Only the first 100 (50) principal components of the years 2000–2008 (1981–2010) are used to train the Bayesian network because they already cover most of the variance and the large-scale patterns.

4.2.3. Output Processing

If the trained Bayesian network now is given a set of principal components from an RCM or GCM, it will assign a number to this input data, which correlates to the likeliness of this day being a Mistral or Tramontane day. High values of this output indicate that a day is likely to show a Mistral and Tramontane permitting sea-level pressure pattern. A threshold value is needed to map this continuous output variable to a TRUE/FALSE variable. The requirement that the number of days with values above the threshold is the same as the number of observed Mistral and Tramontane days in the same period determines its value.

4.3. Idealized Simulations with COSMO-CLM

The idealized simulations presented in this thesis cover a $10^\circ \times 10^\circ$ domain at 38–48° N with 601×601 grid cells and 40 vertical levels using the idealized setup of the non-hydrostatical climate model COSMO5-CLM7 (Rockel et al. (2008); Blahak (2015)). Open boundary conditions (wave-absorbing conditions) were used with an overlay of a constant 5 m/s inflow from the north.

In the lowest 12 km the atmosphere has a stable constant temperature gradient of -6.5 K/km, a typical value for the European region. Above that level, the temperature of the idealized setup is 210.15 K. The grid spacing was $\approx$1.3 km on a non-rotated longitude-latitude grid, which corresponds to the native resolution of the orography dataset ETOPO1 at about 45°N (Amante and Eakins (2009)).

The altitude of the Mediterranean Islands (the Balearic Islands, Sardinia, and Corsica) was set to 0 m and their surface was treated as water surface. Furthermore, the orography at the northern border was linearly interpolated to 0 m. In this study, the orography was smoothed by factors 2–34 using linear interpolation, while keeping the numerical grid spacing constant at one arc minute.

Four different simulation setups, differing in whether or not they regard Coriolis force, surface fluxes, and subgrid-scale orography (SSO, Schulz (2008)) were tested. The simplest setup did not include any of Coriolis force, surface fluxes or SSO. The next more complex simulation included Coriolis force in the f-plane approximation with $f = 2\sin(45^\circ)$. Since the idealized setup does not have a geostrophic pressure initialization, the wind field needs some time to adjust to an equilibrium flow (Blahak (2015)), and during the adjustment phase, some boundary effects might occur. Therefore, the simulations run for 14 days and the evaluation applies to days 11 to 14.

The next simulation included Coriolis force and surface transfer coefficients and, therefore, a momentum transfer in the ground with a constant roughness length of 0.01 m over the land area. Over sea surface, the Charnock formula (Charnock (1955)) parameterizes the surface roughness length depending on the local wind speed. In COSMO-CLM, a constant Charnock parameter of $\alpha = 0.0123$ is used (Doms et al. (2011)). The fourth and most complex setup added SSO to Coriolis force and surface transfer coefficients. Including SSO leads to increased surface fluxes and, therefore, to lower wind speeds near the surface. In this setup, the SSO parameters were calculated for each grid cell of the smoothed orography, not that of the numerical grid of the simulation.

4.4. Evaluation

4.4.1. Proportional Correct Score

The proportional correct (PC) score gives the percentage of days, on which observation and simulation agree on a Mistral and Tramontane event being present. Table 4.3 shows the possible outcomes of a forecast. If an event was predicted and observed, the forecast was correct (hit). If an event was predicted, but not observed, a false alarm occurred. A miss happened if the event occurred, but was not predicted. If no event was predicted and it did not occur, the forecast is called correct negative. The PC score then is the number of hits and correct negative divided by all cases, i.e., the percentage of cases on which forecast and observation agree.

Table 4.3.: Possible cases for agreement of prediction and observation

	observed	not observed
predicted	hit	false alarm
not predicted	miss	correct negative

4.4.2. Fetch

Fetch is defined as the distance, which an air parcel has traveled above the sea before reaching its current position. To account for the uncertainties in the path of the air parcel, the effective fetch can be estimated by calculating the weighted average of the distance to the coast $d(\phi_i)$:

$$fetch(\phi) = \frac{1}{90} \sum_{\phi_i=\phi-90^\circ}^{\phi+90^\circ} \left[cos^2(\phi - \phi_i) \cdot d(\phi_i)\right] \tag{4.1}$$

Here, the interval $\phi{-}90^\circ \leq \phi_i \leq \phi{+}90^\circ$ of the current wind direction ϕ at the grid cell is used (Lange et al. (2001)) with ϕ_i increasing in 1° steps.

4.4.3. Bias and RMSE

For scalar quantities x as wind speed and sea-level pressure, bias and root mean square error (RMSE) can be calculated as

$$bias_x = \frac{1}{N}\sum_{t=1}^{N}\left(x_{sim}(t) - x_{obs}(t)\right) \tag{4.2}$$

and

$$RMSE_x = \sqrt{\frac{1}{N}\sum_{t=1}^{N}\left(x_{sim}(t) - x_{obs}(t)\right)^2} \tag{4.3}$$

The calculation for wind direction is more complicated because the wind direction difference has to be in the interval of $\pm 180°$. The difference between an observation (β_{obs}) and a simulation (β_{sim}) at time t is $\beta_t = \beta_{sim}(t) - \beta_{obs}(t)$. Bias and RMSE can be calculated as

$$bias_\beta = \frac{1}{N}\sum_{t=1}^{N}\begin{cases} \beta_t & , \quad |\beta_t| \leq 180° \\ (|\beta_t| - 360°)\cdot\frac{\beta_t}{|\beta_t|} & , \quad |\beta_t| > 180° \end{cases} \tag{4.4}$$

and

$$RMSE_\beta = \sqrt{\frac{1}{N}\sum_{t=1}^{N}\begin{cases} \beta_t^2 & , \quad |\beta_t| \leq 180° \\ (|\beta_t| - 360°)^2 & , \quad |\beta_t| > 180° \end{cases}} \tag{4.5}$$

4.4.4. Main Flow Area

In this study, the main flow area of Mistral and Tramontane is determined as the longitudinal location of the maximum surface wind speed for each latitude. If no global maximum can be determined, the average longitude of all local maxima with the highest wind speed is used as the location of the maximum wind speed.

5. Results and Discussion

Following the four research questions introduced in Chapter 1, this section presents and summarizes the results of the four peer-reviewed publications which contributed to this thesis. Appendices A to D contain the four publications and give more details on the results.

5.1. How well do RCMs simulate the Mistral and Tramontane permitting sea-level Pressure Patterns?

Certain large scale pressure patterns initiate Mistral and Tramontane events (Section 2.1). Therefore, a first step in evaluating Mistral and Tramontane days is determining the days on which the simulations represent the large-scale flow well. Furthermore, the correct representation of sea-level pressure patterns is necessary to enable RCMs and GCMs to simulate wind fields during Mistral and Tramontane events. If the large-scale pattern is reproduced erroneous, the Mistral or Tramontane event might be missed completely, simulated at the wrong day, or with inaccurate intensity. This section discusses the percentage of days on which the RCMs agree with the observations regarding large-scale patterns and other Mistral and Tramontane statistics.

5.1.1. Representation of Mistral and Tramontane Days

The classification algorithm described in Section 4.2 classifies the daily mean sea-level pressure fields from RCM simulations regarding similarity to the ERA-Interim patterns of days with observed Mistral and Tramontane. The classification algorithm has two different configurations, configuration A for a nine-year training period (see Appendix A) and configuration B for a 30-year training period (see Appendix D).

Table 5.1 lists the proportion correct (PC) score, which is the percentage of days on which the observation and simulations agree on a Mistral and Tramontane permitting

sea-level pressure pattern being present or not (Section 4.4.1). The PC scores of configuration A were about 9 % higher than for configuration B.

This difference could be due to the more diverse Mistral and Tramontane events which occurred during the 30-year period than in the nine-year period, and more varied climate conditions. Furthermore, a high PC score is more relevant for the 2000-2008 period of configuration A, because in this period the simulations can be compared directly to observations (Section 5.2). The longer training period of configuration B is suitable for estimating the number of Mistral and Tramontane events in climate projections of the 21st century, for which a diverse training database is beneficial, even if the accuracy in the training period decreases (Section 5.4).

Table 5.1.: Proportion correct (PC) score of days with wind systems correctly predicted by the classification algorithm for ERA-Interim and ERA-Interim-driven RCMs (1981 to 2008 for RegCM4-3) in days.

Simulation	Grid (°)	PC score	
		A (2000–2008)	B (1981–2010)
CNRM-ALADIN	0.44	76.7	68.3
	0.11	77.0	–
IPSL-WRF	0.44	79.1	–
	0.18	79.0	–
UCLM-PROMES	0.44	75.6	–
	0.22	74.5	–
GUF-CCLM4-8-18	0.44	77.3	68.8
	0.088	75.1	–
CMCC-CCLM4-8-19	0.44	76.0	68.5
LMD-LMDZ	0.44	75.9	–
RegCM4-3	0.44	–	66.6
ERA-Interim		82.0	70.6

Even though it was the training data, ERA-Interim achieves a PC score of less than 100 % in both configurations of the classification algorithm for several reasons. The classification algorithm did not regard all EOFs. In combination with inaccuracies in the station derived Mistral and Tramontane time series, this leads to a loss of information and increases the probability of false alarms and misses.

For both configurations, the simulations reached about 92–96 % of the corresponding ERA-Interim result. The RCMs of this study, therefore, can reproduce the Mistral and Tramontane permitting large-scale pressure patterns when provided with ERA-Interim boundary data. Even though the identification of Mistral and Tramontane days does not work flawlessly for RCMs, a high amount of days has well-simulated sea-level pressure patterns resulting in a correct identification of Mistral and Tramontane situations.

5.1.2. Number of Mistral and Tramontane Days per Year

Besides identifying Mistral and Tramontane events on the correct dates, climate models should be able to reproduce the Mistral and Tramontane climatology. For the climate projection studies discussed below the accuracy in predicting the number of Mistral and Tramontane days per year is of interest.

Table 5.2 lists the correlation of Mistral and Tramontane days/year of the RCM simulations and observations for the 30year training period (configuration B, Appendix D). RCMs can identify years with little and abundant Mistral and Tramontane events. However, the correlation of observed and simulated Tramontane days is higher than that of Mistral days. This finding could be due to the smaller number of Mistral days which occurred during the training period. There were twice as much Tramontane days than Mistral days observed.

Table 5.2.: Correlation of days/year of Mistral and Tramontane events from ERA-Interim and ERA-Interim-driven RCMs for the years 1982 to 2010 (1982 to 2008 for RegCM4-3) in days.

	Correlation days/year	
Simulation	Mistral	Tramontane
ALADIN52	0.57	0.67
CCLM4-8-18	0.47	0.72
CCLM4-8-19	0.44	0.67
RegCM4-3	0.55	0.77
ERA-Interim	0.61	0.78
Observation	1.00	1.00

5.1.3. Average Mistral and Tramontane Duration

Table 5.3 lists the average Mistral and Tramontane period length of the RCM simulations and observations for the 30year training period (configuration B, Appendix D). All models show 24 % higher values than observed. A possibly erroneous simulation of blocking situations could cause this overestimation.

Table 5.3.: As Table 5.2 but for average period length.

	Average period length	
Simulation	Mistral	Tramontane
ALADIN52	2.2	2.9
CCLM4-8-18	2.0	2.9
CCLM4-8-19	2.0	2.9
RegCM4-3	2.3	3.5
ERA-Interim	2.1	3.3
Observation	1.7	2.5

5.2. How well are the Wind Speed and Wind Direction Patterns represented?

Figure 5.1 presents the mean wind patterns sorted according to the combined station time series for 2000–2008 (Section 4.1), the period for which QuikSCAT data is available. During days with both Mistral and Tramontane (left upper panel of Figure 5.1), increased wind speeds in both the Rhône Valley and Aude Valley are present. During Mistral only (right upper panel) and Tramontane only (left lower panel) events the wind speed increases only in one of the valleys. The wind speed over the sea also increases close to exit of the valleys. The strongest growth is present when both winds occur.

This section summarizes the results from Appendix A. Thus, the focus is on days on which either both Mistral and Tramontane or none of them occurred. Days with only Mistral or only Tramontane were excluded from this analysis because only a small number of Mistral only events occurred (12 %, see Table 4.1). Furthermore, the interpretation focuses on days for which simulations and observations agree on a Mistral and Tramontane event being present or not, which holds true for about 74 to 82 % of the days in the years 2000-2008 (configuration A in Table 5.1). This choice excludes the errors due to wrongly simulated large-scale pressure fields discussed in the previous section.

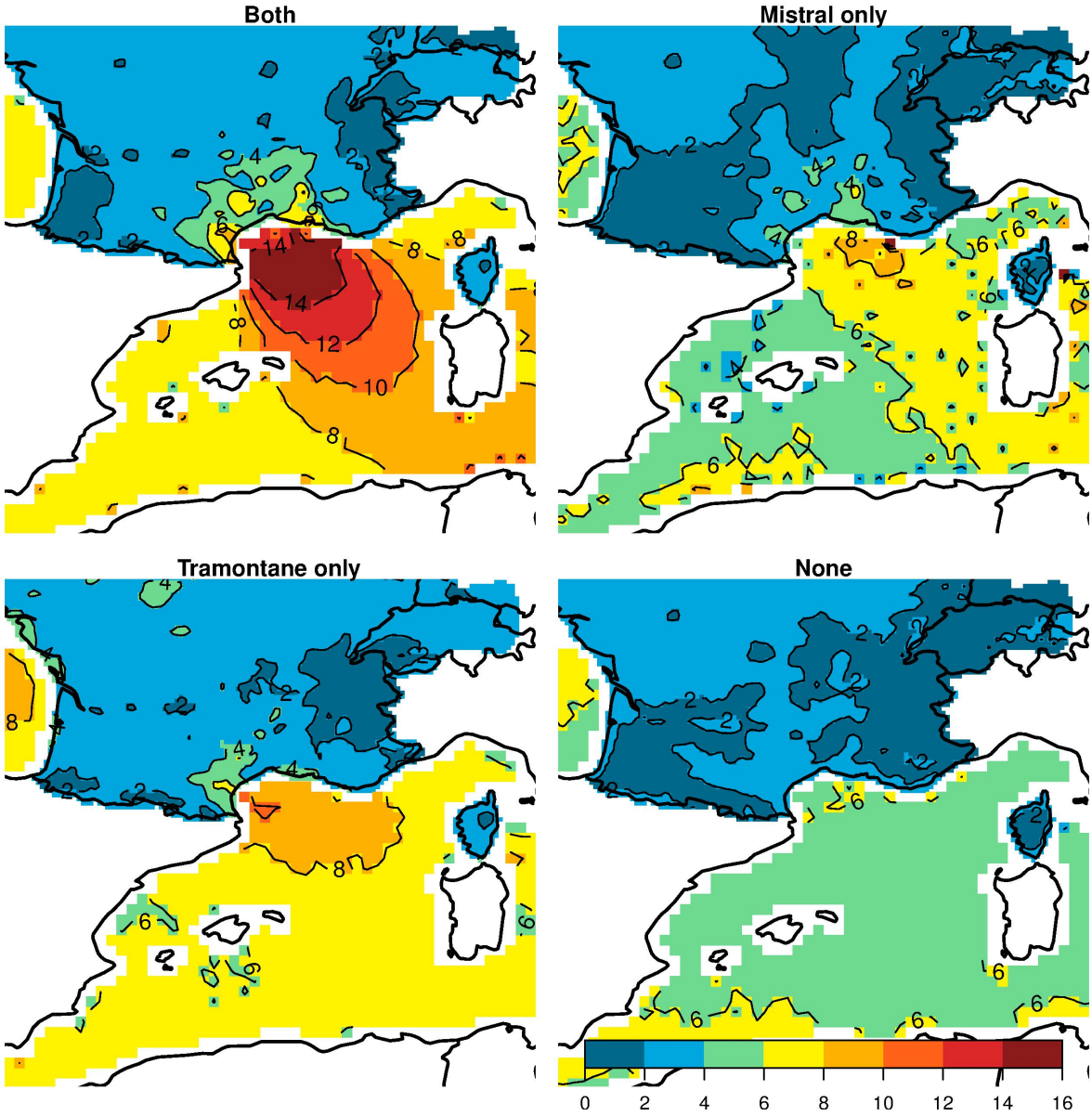

Figure 5.1.: Wind speed (m/s) from QuikSCAT and SAFRAN data.

5.2.1. Spatial Patterns

Figure 5.2 displays the wind speed bias of the GUF-CCLM4-8-18 simulations with QuikSCAT and SAFRAN data as the reference. The 0.44° simulation underestimates the wind speeds in the Gulf of Lion by about –0.5 to –3 m/s. The bias is stronger at the borders of the main flow (close to the coast). This underestimation also occurs on days with neither Mistral nor Tramontane but is less pronounced. The other evaluated RCMs show similar patterns (Appendix A.5.2). The 0.088° simulation shows higher wind speeds and also a small positive bias in some areas of the Gulf of Lion. This increase of wind speed with increased horizontal resolution also is present for the other three RCMs of this study for which simulations with two different resolutions were available (Figures A.9 and A.10).

All RCM simulations show a clockwise bias in the wind direction fields during Mistral and Tramontane events in the Gulf of Lion. Figure 5.3 displays the results for GUF-CCLM4-8-18 simulations with QuikSCAT as reference. The wind direction shows a positive (i.e. clockwise) bias in large parts of the Gulf of Lions. However, the patterns of days with and without Mistral and Tramontane differ. During days with neither Mistral nor Tramontane, the wind direction bias is stronger than on Mistral and Tramontane days. The wind speed RMSE is higher during Mistral and Tramontane days than the other days. In contrast, the wind direction RMSE is lower (Figures A.11 and A.14).

The underestimation of wind speed over the Gulf of Lions could be partially canceled out by the overestimation of wind speed in QuikSCAT. QuikSCAT overestimates the wind speeds by 0.5 m/s at the Gulf of Lion buoy and 0.59 m/s at the Azur buoy on average. The RMSE is 1.44 m/s and 1.50 m/s, respectively (Ruti et al. (2008)). Furthermore, less QuikSCAT observations are available close to the coast, which could influence the pattern found.

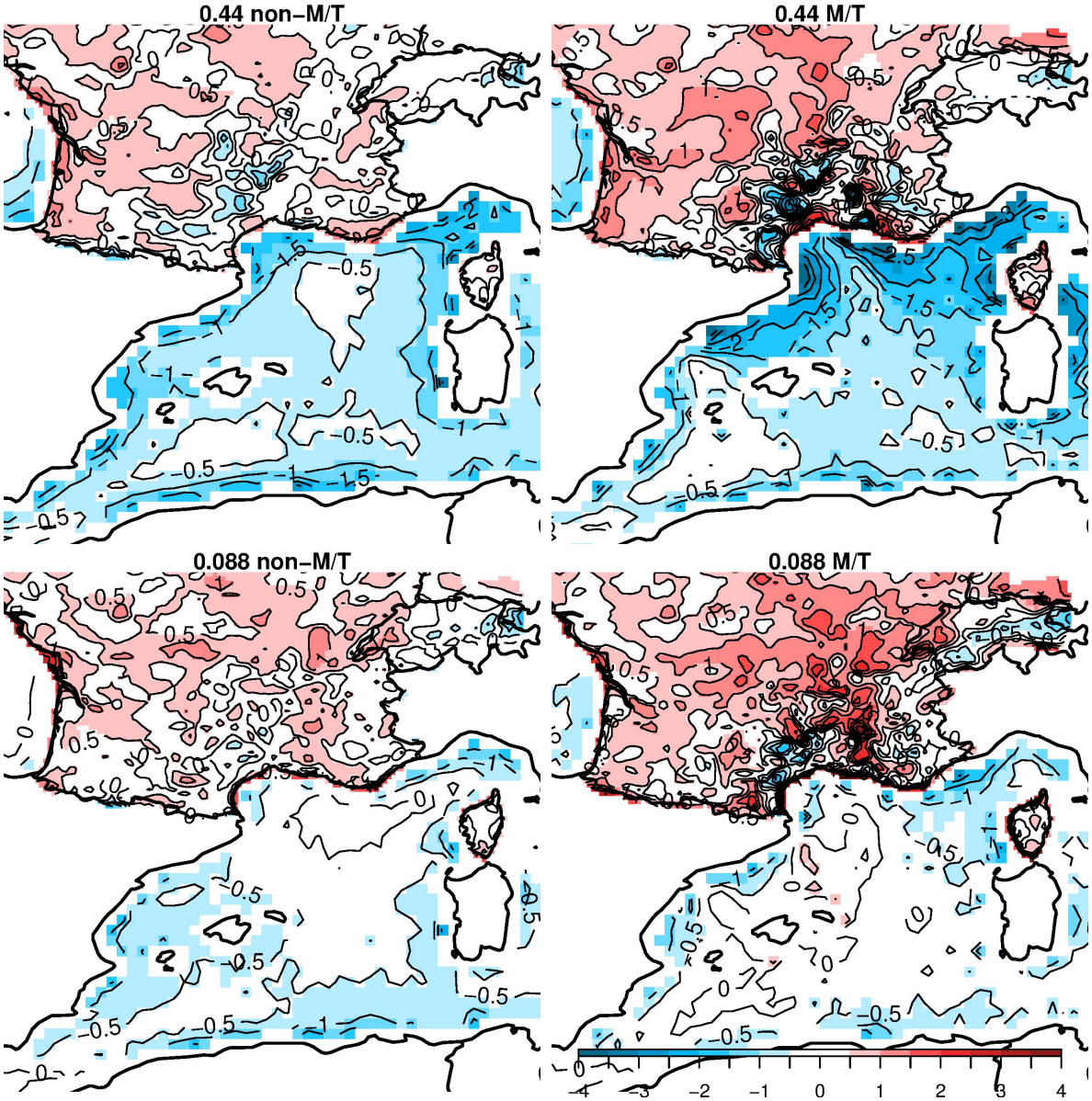

Figure 5.2.: Wind speed bias (m/s) with respect to QuikSCAT and SAFRAN data for GUF-CCLM4-8-18 simulations with 0.44° (upper row) and 0.088° (lower row) grid spacings for days with neither Mistral nor Tramontane (non-M/T, left) and days with both winds (M/T, right).

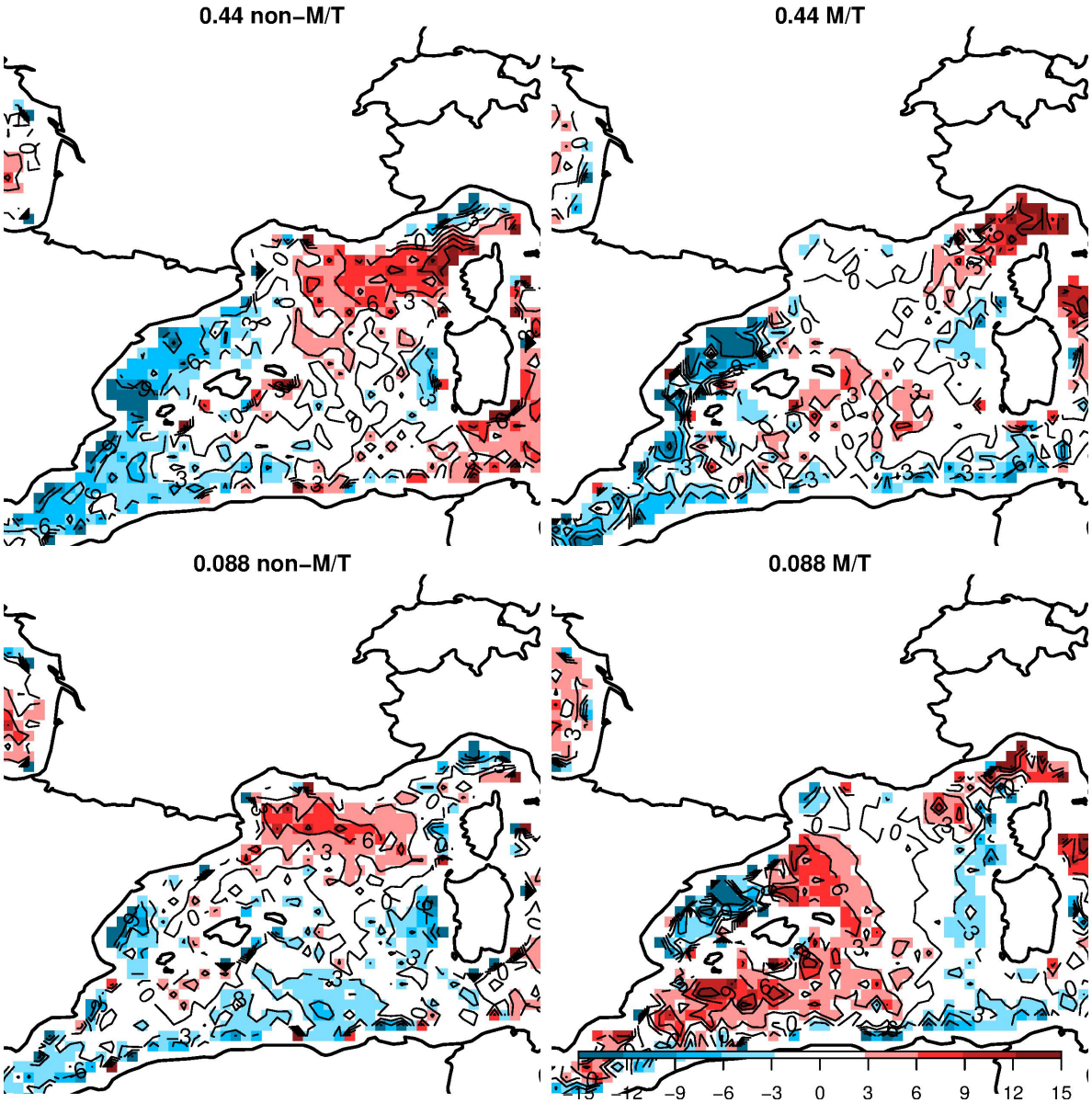

Figure 5.3.: As Figure 5.2, but for wind direction bias (°) with respect to QuikSCAT. Positive (negative) values denote a clockwise rotated (counter-clockwise rotated) wind direction.

5.2.2. Along-Flow Development

In the Rhône Valley, the SAFRAN dataset shows two wind speed maxima. One at the narrowest part of the valley and one close to the opening of the valley. The simulations show an increase in wind speed at the narrowest part of the valley, but not on the valley opening. The models perform better in simulating the continuous wind speed increase in the Aude Valley. The interpolation between valley and mountain grid cells can be difficult for the simulations, especially in confined parts of the valleys. Also, hydraulic jumps can occur in both Mistral and Tramontane flows (Drobinski et al. (2001, 2005)), which causes additional difficulties for modeling.

When approaching the Mediterranean Sea, all simulations show higher wind speeds than the SAFRAN dataset and almost reach the wind speeds observed by QuikSCAT. The simulations reproduce the overall fetch dependence of the wind speed over the Gulf of Lion, but errors are highest close to the coast.

The wind direction information is only available for the QuikSCAT observational data set. The bias in wind direction is positive (clockwise rotated) for small fetch, and turns to negative (counter-clockwise rotated) values after about 300 km for all simulations. Appendix A.5.3 presents a detailed analysis of the along-flow development of Mistral and Tramontane.

5.3. Which Factors determine the Mistral and Tramontane Representation in Simulations?

As seen above, the simulations show a particular pattern in wind speed and wind direction bias. Several processes are involved in the Mistral and Tramontane simulation: from the pressure gradient along the valleys, over the acceleration in the valleys due to inclination and constriction, to the surface roughness. Additionally, the horizontal grid spacing has an impact on the pattern.

5.3.1. Charnock Parameterization

As seen in Figure 5.2, the GUF-CCLM4-8-18 simulation with smaller grid spacing and, therefore, higher resolution shows higher wind speeds than its counterpart on a coarser grid. The surface wind speed depends on the surface roughness length, which in the case of a sea surface depends on the wave height and therefore in turn on the wind speed. This dependency is described by the Charnock formula (Charnock (1955)) and discussed in Section 2.2.

The sensitivity study presented here focuses on the year 2005 because it had a high number of Mistral days. Simulations were performed on a domain over the western Mediterranean area with one-way nesting in the GUF-CCLM4-8-18 simulation with 0.088° grid spacing (Edelmann (2015)). In the Charnock formula, the values α=0.0123 (standard in COSMO-CLM, Doms et al. (2011)), α=0.025, and α=0.05 were tested.

The changes during the Mistral events of 2005 included lower wind speeds mainly in the central Mistral and Tramontane flow area. A counter-clockwise rotation occurred in the southwestern part of the domain. Therefore, a higher value of α improved the Mistral and Tramontane representation in the GUF-CCLM4-8-18 0.088° simulation, which showed slightly too high wind speeds and a clockwise wind direction bias (Figure 5.2). Appendix B.3.2 and Edelmann (2015) give more information on this sensitivity test and the changes due to further modifications of the Charnock parameterization in GUF-CCLM4-8-18.

5.3.2. Balance of Forces

As described in section 2.3, the main contributing forces to Mistral and Tramontane are pressure gradient force, Coriolis force, and friction. To identify the impact of these forces on the simulations, they were switched on and off in idealized simulations. In this thesis, four idealized setups with increasing complexity are used (Section 4.3 and Appendix C).

Figure 5.4 presents the wind speed, wind direction, and sea-level pressure for the idealized simulation setups with orography information smoothed by a factor of 2. In the simplest setup oro2$_{none}$, Mistral and Tramontane accelerate in the valleys and show a northerly to northwesterly wind direction (left upper panel). The sea-level pressure is lower at the sides of the main flow than on its center. Pressure gradient force and channeling effects drive the flow. This setup neglects Coriolis and friction force.

When including Coriolis force, the wind speeds increase by about 5 m/s and the wind comes from a more northerly direction (oro2$_{cori}$, right upper panel). At the same time, an east-west pressure gradient develops due to Coriolis force and the counteracting pressure gradient force. When surface momentum transfer and, therefore, surface friction, is introduced the wind speed decreases by about 10 m/s (oro2$_{flux}$, left lower panel). Adding SSO to the calculation of surface friction in oro2$_{SSO}$ leads to reduced wind speeds in most areas and changes in wind direction and sea-level pressure (right lower panel).

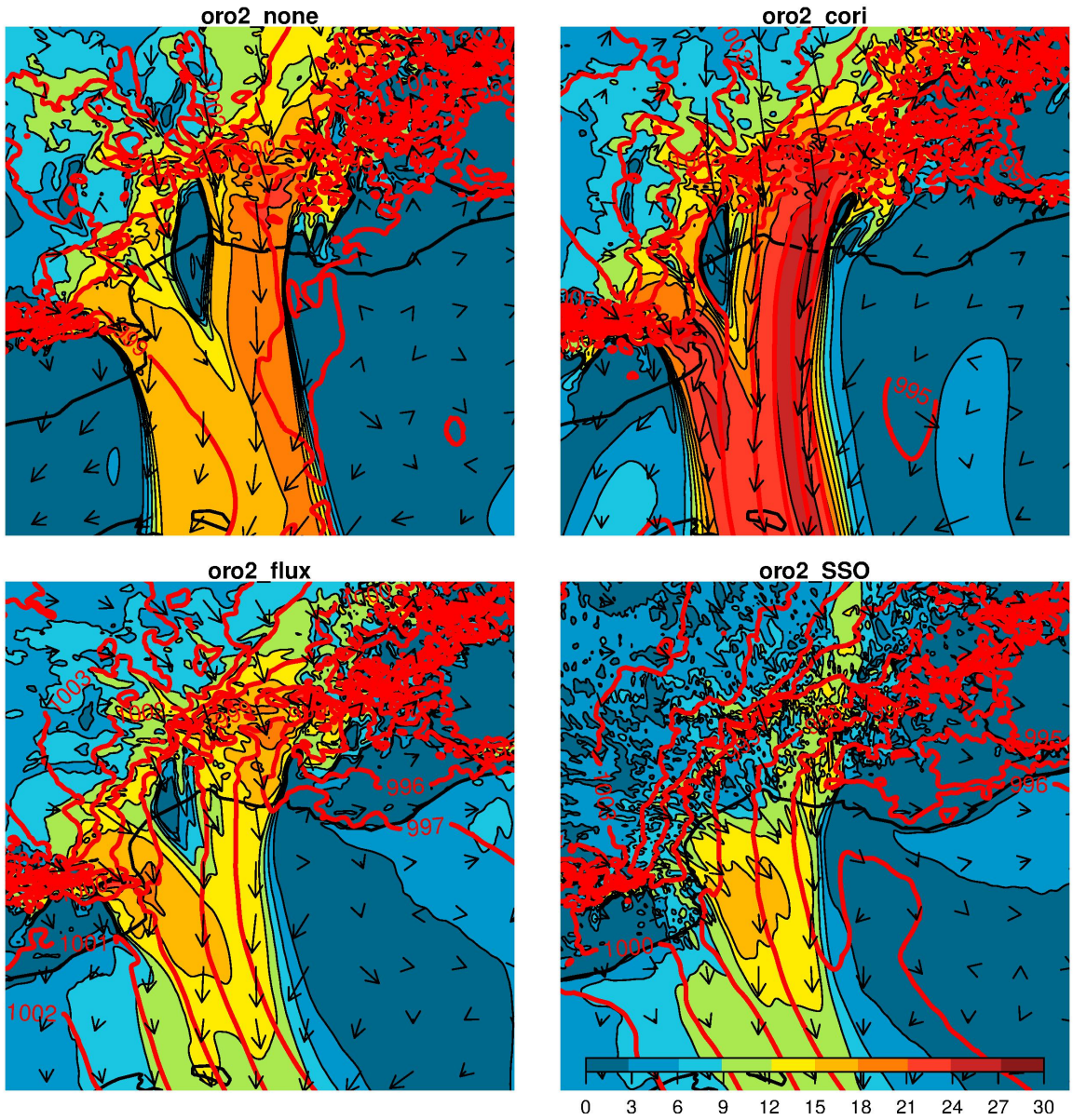

Figure 5.4.: Mean wind speed (m/s, color scale) direction (arrows) at the lowest model level and mean sea-level pressure (hPa, red) of day 11-14 for idealized simulations. Coastline is shown in bold.

5.3.3. Resolution of the Orography

Another possible reason for differences between the RCM simulations discussed above is the orographic resolution. This section summarizes the results described in Appendix C. Figure 5.5 displays the wind speed change for smoothed orography simulations in comparison to the oro2 simulation of the same setup. The area east of Mistral shows lower wind speeds, while west of Tramontane higher wind speed occurs in oron_{none}, and oron_{cori} simulations, hinting to a westward shift of the wind systems. oron_{flux} shows a similar, but a weaker pattern, while oron_{SSO} shows decreasing wind speeds at both sides of the flow. In the area where both winds merge, the changes are smaller.

Figure 5.6 shows the change in wind direction analog to Figure 5.5. Strong changes in wind speed mainly occur at the borders of the flow, while the main flow wind direction does not change. This further hints to a change in the affected area with decreasing orographic resolution. The largest changes occur in the oron_{none} and oron_{cori} simulations. Including surface fluxes in oron_{flux} simulations reduces this resolution dependence. Including an SSO parameterization in oron_{SSO} simulations reduces the change in wind direction due to smoothing of the orography.

The results of this study show that a wind speed decrease is present when smoothing the orography, but keeping the simulation grid spacing constant. Parameterizing the small scale features of the smoothed orography reduces these effects. This resolution dependence could explain part of the pattern in wind speed bias described in Section 5.2.1 and Appendix A, where not all models included SSO effects. The longitudinal position of the wind speed maximum also changed depending on the orographic resolution by 10 to 45 km. This change is in the same order of magnitude as the vortex diameter in the Gulf of Lion found by Allou et al. (2010) (12 to 28 km). A misplacement of Mistral wind speeds could influence the development of the vortices in coupled simulations.

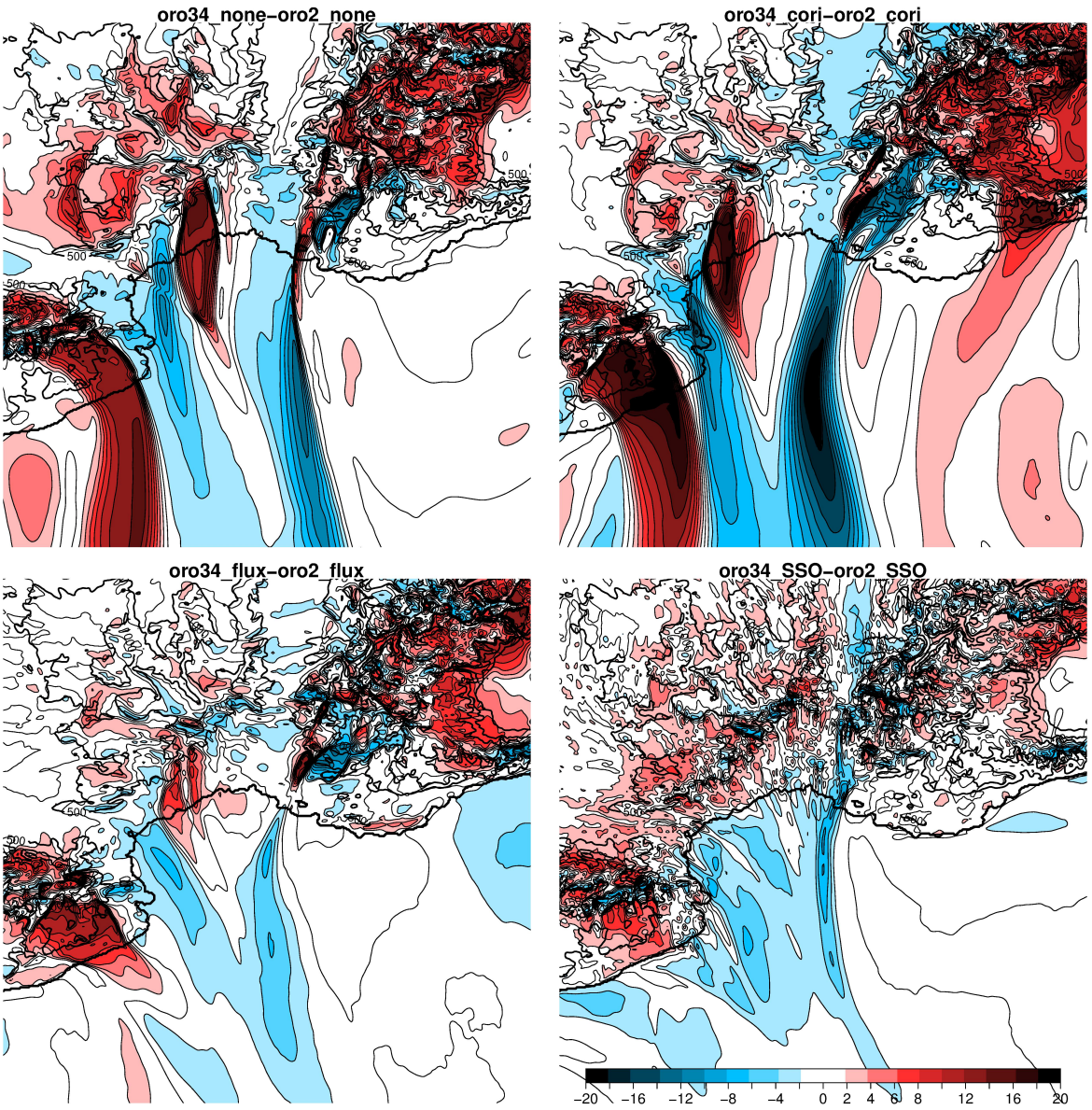

Figure 5.5.: Change in wind speed (m/s) at lowest model level when orography is smoothed from $n = 2$ to $n = 34$. Bold line indicates coastline.

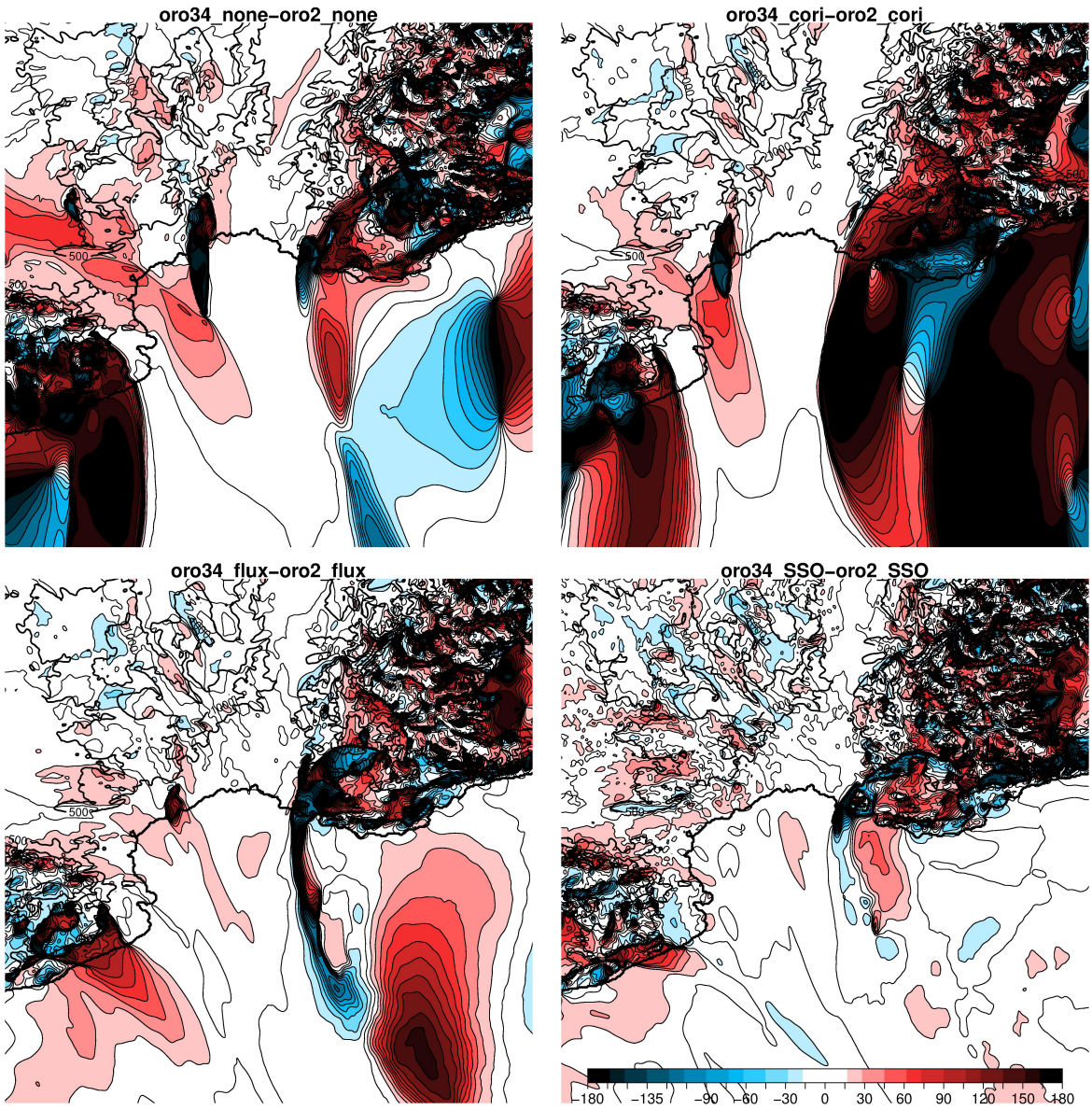

Figure 5.6.: As Figure C.3 but for wind direction (°) at lowest model level. Positive (negative) values indicate a clockwise (counter-clockwise) shift.

5.4. Which Changes in Mistral and Tramontane can be found in Climate Projections?

To identify days with Mistral and Tramontane permitting sea-level pressure patterns, a threshold for the classification algorithm presented in this thesis has to be chosen. It was set in a way that each model showed the observed number of Mistral and Tramontane days during the reference period (the observation period 1981–2010). The same value was used as a threshold for the historical and projection simulations (Appendix D).

5.4.1. Mistral and Tramontane Frequencies

Figures 5.7 and 5.8 present the average number of Mistral and Tramontane days per year identified by the classification algorithm (Tables D.4 to D.7 in the appendix). The simulations with both GCMs and RCMs show only small changes in Mistral frequency in both RCP4.5 and RCP8.5 scenarios, while the changes in Tramontane frequency were significant on the 95% level for some simulations.

A significant reduction for Tramontane days per year was found in CMCC-CM, MPI-ESM-MR, and CNRM-CM5 for the last 30 years of the 21st century in the RCP8.5 projections. CMCC-CM also showed a significant decrease during 2041–2070, while the reduction in MPI-ESM-MC and CNRM-CM5 is significant for 2011–2040.

The RCMs indicate a decrease in Tramontane events in RCP8.5 for the years 2041 to 2070 (MPI-ESM-LR-CCLM4-8-18, CMCC-CM-CCLM4-8-19) as well as 2071 to 2100 (MPI-ESM-LR-CCLM4-8-18, CMCC-CM-CCLM4-8-19, and MPI-ESM-MR-RegCM4-3). CMCC-CM-CCLM4-8-19 also shows a significant lessening of Tramontane events during 2071-2100 for RCP4.5. None of the simulations showed a significant increase in Mistral or Tramontane events during the 21st century.

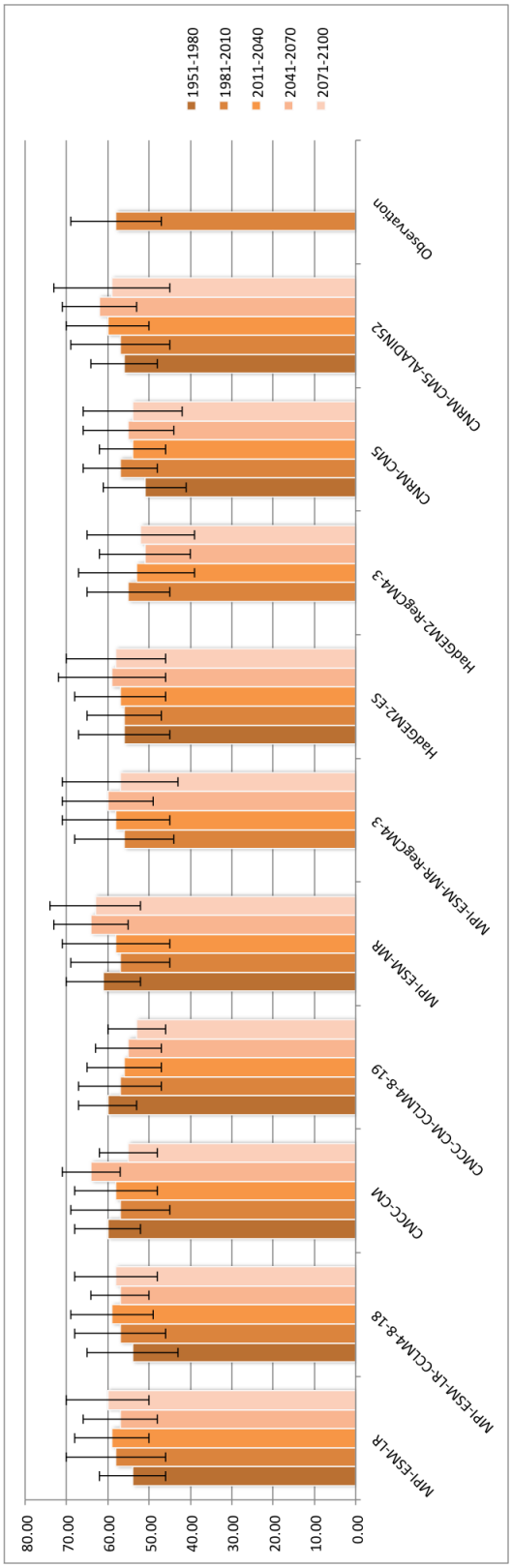

Figure 5.7.: Average number of Mistral days per year for historical and RCP8.5 simulations. Black bars indicate standard deviation.

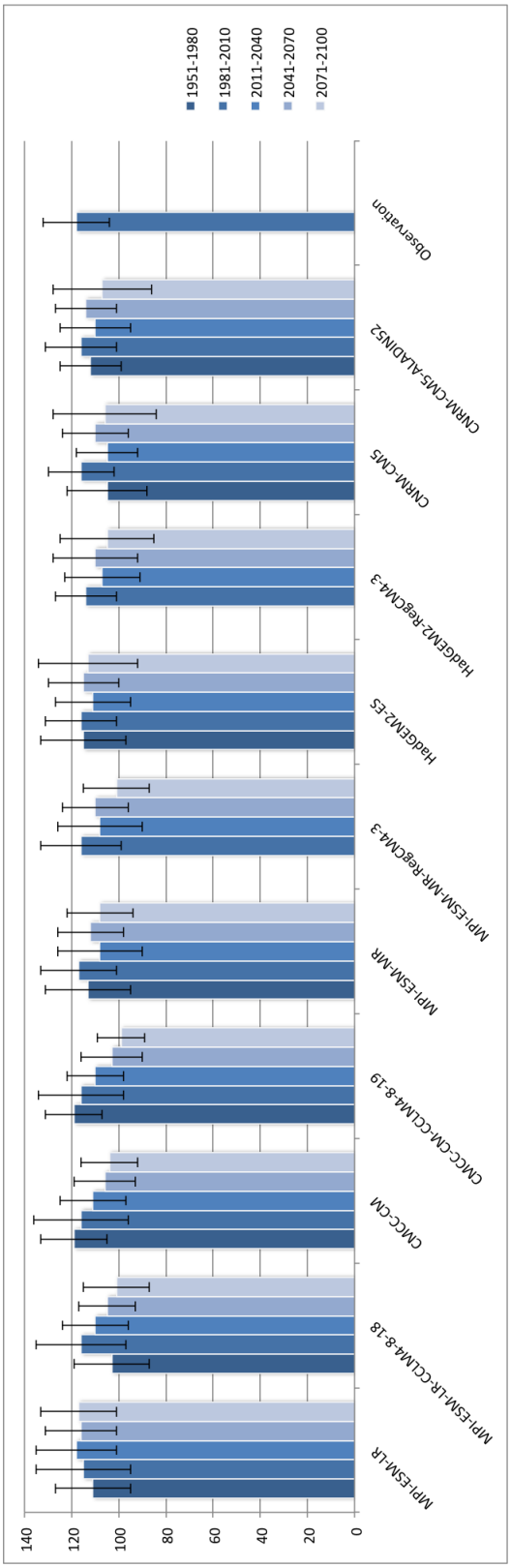

Figure 5.8.: As Figure 5.7 but for Tramontane.

5.4.2. Wind Speed Changes

The 90th percentiles of wind speed also decrease in parts of the Gulf of Lions area. The decline is stronger for simulations which show higher significant changes in Tramontane days per year. Figure 5.9 shows the changes for MPI-ESM-LR-CCLM, the results for the other simulations can be found in Appendix D.4. The wind speed on the classified Mistral and Tramontane days in the projections shows significantly higher wind speeds in the Mistral and Tramontane area than the days classified as non-Mistral and Tramontane days. The wind speeds during Mistral and Tramontane events stay at about the same value as during the reference period.

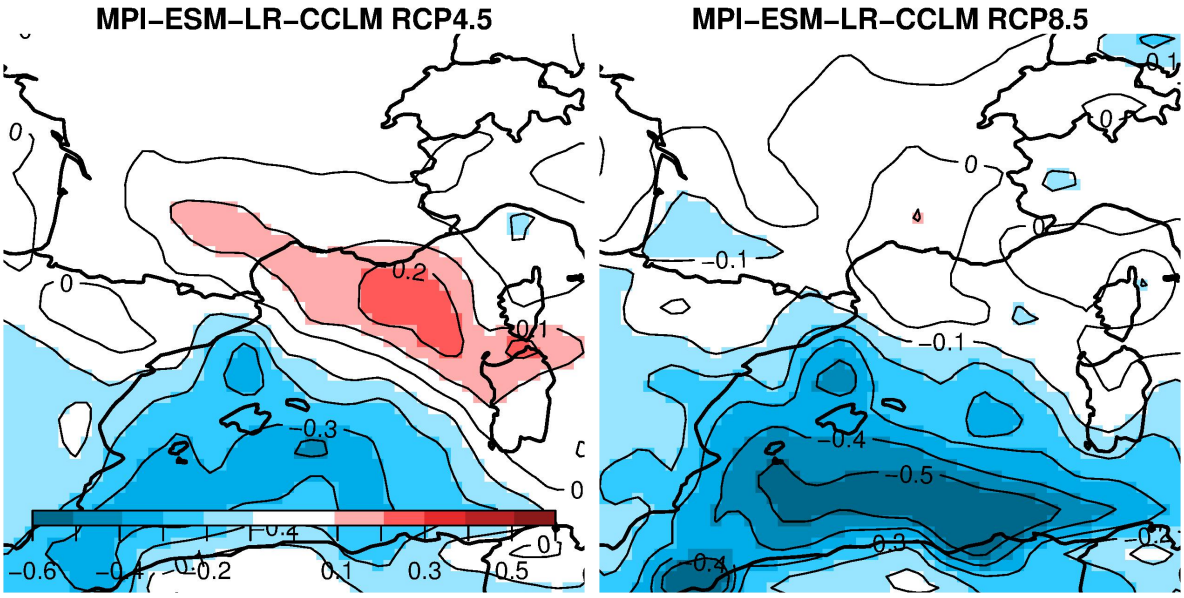

Figure 5.9.: Change in 90th percentile during 2071–2100 compared to 1981–1970 (m/s).

6. Conclusion

This thesis focused on the representation of Mistral and Tramontane in climate simulations. Starting from observational data and simulation results from regional climate models (RCMs) of the MedCORDEX framework, the ability of climate simulations to simulate Mistral and Tramontane was evaluated. This chapter presents the most important findings of the previous chapter and conclusions.

When the large-scale patterns are represented well in the boundary data, RCMs with a grid spacing of 0.088–0.44° could simulate Mistral and Tramontane at the correct dates, as well. Sea-level pressure patterns from climate projections of the 21st century with RCMs and global circulation models (GCMs) indicated a decrease in Tramontane events per year but no conclusive evidence was found for significant change in Mistral events. The agreement of RCMs and the GCM which provided the boundary data was about 80 %. Since each RCM in this study was driven by a different GCM, the sensitivity of the RCMs on the boundary data in comparison to the impact of e.g. internal physics schemes could not be determined in greater detail. For such a study, an ensemble with several RCMs driven by the same GCM and ideally also several GCMs driving the same RCM would be necessary. This is computationally expensive and probably would be needed to be coordinated between several modeling groups.

For Mistral and Tramontane events, most studied RCMs underestimated the wind speed over the Mediterranean Sea. However, they showed better agreement with the observations than ERA-Interim, which provided the boundary data. RCMs, therefore, are able to add value to coarser simulation results in terms of wind speed and wind direction information. Higher resolution simulations (0.088–0.22° grid spacing) showed smaller wind field biases than their 0.44° counterparts. Thus, an advantage of using RCMs with small grid spacing is in the improved representation of wind fields. This applies not only to areas with small-scale orographic features like the valleys and mountainous areas but also to the Mediterranean Sea. On one hand, this is surprising because the Gulf of Lions does not show orographic features, on the other hand, an improved representation in the valleys should lead to an improved representation further downwind.

The studied higher resolution simulations showed higher wind speeds than their coarse counterparts. The studied Med-CORDEX simulation with the smallest grid spacing (0.088°) showed even an overestimation of wind speed in some areas of the Gulf of Lion.

Further increasing the resolution could result in an even stronger overestimation of wind speeds. As presented in a case study with COSMO-CLM, this could be compensated by modifying the parameterization of the sea surface roughness length. The studied RCM simulations calculate the roughness length depending on the wind speed. Including further information about the sea state, e.g. from coupled ocean and wave models, might improve the simulation of mesoscale winds and could be surveyed in future studies.

Another important finding was that the simulated wind field does not only depend on the grid spacing, but also on the orographic resolution. The longitudinal position of the wind speed maximum in idealized simulations changed depending on the orographic resolution. Increasing the grid spacing from 2.6 km to more than 40 km in steps of about 10 km, lead to a shift of up to 45 km. A misplacement of Mistral in that order of magnitude could influence the development of the Mediterranean Sea vortices in coupled simulations. Using an SSO parameterization can compensate the effect only partially: The shift decreased to about 20 km and did less depend on the resolution. Furthermore, a systematic underestimation due to channeling effects remained present even with SSO. Therefore, a high-resolution orography appears to be beneficial for regional climate simulations, especially with coupled models.

In summary, RCMs have proven to be a useful tool to simulate the wind fields of mesoscale wind systems in a geographically complex area. However, climate studies on mesoscale winds need to make a compromise between the desired resolution and resolved processes on one hand and the available computational resources on the other hand. With increasing computing resources, simulations with smaller grid spacing and a coupled ocean can be performed over longer time intervals. Thus, the benefit for mesoscale winds in coupled and high-resolution climate simulations could be studied. Besides surveying RCM simulations in terms of other Mediterranean Winds like Bora, and Etesians for climate change studies, it also would be interesting to survey mesoscale winds in other areas, e.g. the Oroshi in Japan or Piteraq in Greenland.

A. Paper 1: Mistral and Tramontane Wind Speed and Wind Direction Patterns in Regional Climate Simulations

published as

Anika Obermann, Sophie Bastin, Sophie Belamari, Dario Conte, Miguel Angel Gaertner, Laurent Li, and Bodo Ahrens, *Mistral and Tramontane Wind Speed and Wind Direction Patterns in Regional Climate Simulations*, Climate Dynamics (2016), 1–18.

Abstract

The Mistral and Tramontane are important wind phenomena that occur over southern France and the northwestern Mediterranean Sea. Both winds travel through constricting valleys before flowing out towards the Mediterranean Sea. The Mistral and Tramontane are thus interesting phenomena, and represent an opportunity to study channeling effects, as well as the interactions between the atmosphere and land/ocean surfaces.

This study investigates Mistral and Tramontane simulations using five regional climate models with grid spacing of about 50 km and smaller. All simulations are driven by ERA-Interim reanalysis data. Spatial patterns of surface wind, as well as wind development and error propagation along the wind tracks from inland France to offshore during Mistral and Tramontane events, are presented and discussed. To disentangle the results from large-scale error sources in Mistral and Tramontane simulations, only days with well simulated large-scale sea level pressure field patterns are evaluated.

Comparisons with the observations show that the large-scale pressure patterns are well simulated by the considered models, but the orographic modifications to the wind systems are not well simulated by the coarse-grid simulations (with a grid spacing of about 50 km), and are reproduced slightly better by the higher resolution simulations. On days with Mistral and/or Tramontane events, most simulations underestimate (by

13 % on average) the wind speed over the Mediterranean Sea. This effect is strongest at the lateral borders of the main flow – the flow width is underestimated. All simulations of this study show a clockwise wind direction bias over the sea during Mistral and Tramontane events. Simulations with smaller grid spacing show smaller biases than their coarse-grid counterparts.

Keywords Regional climate models, Evaluation, Model intercomparison, Mistral, Tramontane, Bayesian network

A.1. Introduction

The Mistral and Tramontane are mesoscale winds in the Mediterranean region that travel through valleys in southern France. The cold and dry Mistral blows from the north to northwest, and travels down the Rhône valley, between the Alps and Massif Central, which opens to the Gulf of Lion. The Tramontane travels the Aude valley between the Massif Central and Pyrenees. Both valleys (areas outlined in blue in Figure A.1) form a constriction before opening towards the Mediterranean Sea, and are therefore interesting areas for studying channeling effects. Over the sea, these winds cause deep-water generation, and thus impact the hydrological cycle of the Mediterranean Sea (Schott et al. (1996); Béranger et al. (2010)). Accurate forecasting of wind speeds is important for assessing the risk of damage from strong winds, to evaluate possible sites for wind energy production, and many other purposes. The Mistral and Tramontane occur in similar synoptic situations, and consequently often occur at the same time (Georgelin et al. (1994); Guenard et al. (2005)). They are most likely to occur in winter (Jacq et al. (2005)).

In this study, nine years (2000–2008) of surface wind simulations using five regional climate models were evaluated. Simulations driven by ERA-Interim at several resolutions were conducted within the Med-CORDEX project (Ruti et al. (2016)) and HyMeX programme (Drobinski et al. (2014)). The grid spacings of the simulations (0.44° and smaller) are appropriate for modeling mesoscale winds such as the Mistral and Tramontane, which can extend several 100 km over the Mediterranean Sea. However, the constrictions and channeling effects in the Rhône and Aude valleys have too complex topography to be well represented in 0.44° simulations.

To the authors' knowledge, this is the first multi-model evaluation of regional climate models in terms of Mistral and Tramontane events covering several years. Several case studies have been performed on Mistral events (Guenard et al. (2005); Drobinski et al. (2005)) and their interaction with sea breezes (Bastin et al. (2006)) and heavy precipitation events (Berthou et al. (2014, 2015)). Tramontane events have also been studied (Drobinski et al. (2001)). An introduction to other phenomena connected to the Mistral and Tramontane is given in Drobinski et al. (2005) and references therein.

This study surveys the Mistral and Tramontane spatial patterns as well as the error propagation along the valleys and over the Mediterranean Sea. Errors that occur far up in the valleys might increase or counteract errors that occur further downstream. Three possible sources of errors are surveyed: large-scale pressure patterns, processes in the valleys, and processes above the Mediterranean Sea. Surface wind speed and direction (i.e., of winds 10 m above ground), as well as sea level pressure over southern France and the western Mediterranean Sea, are compared to gridded observation data sets and reanalysis data. To obtain an objective comparison, and to exclude days on which

the large-scale sea level pressure fields are not well simulated, the days that are used for comparison are determined by a classification algorithm.

This paper is structured as follows. The measurement and simulation data are discussed in Sections A.2 and A.3. Then, the methods used are explained in Section A.4, followed by the results in Section A.5 and a discussion in Section A.6. The last section contains a summary and conclusion.

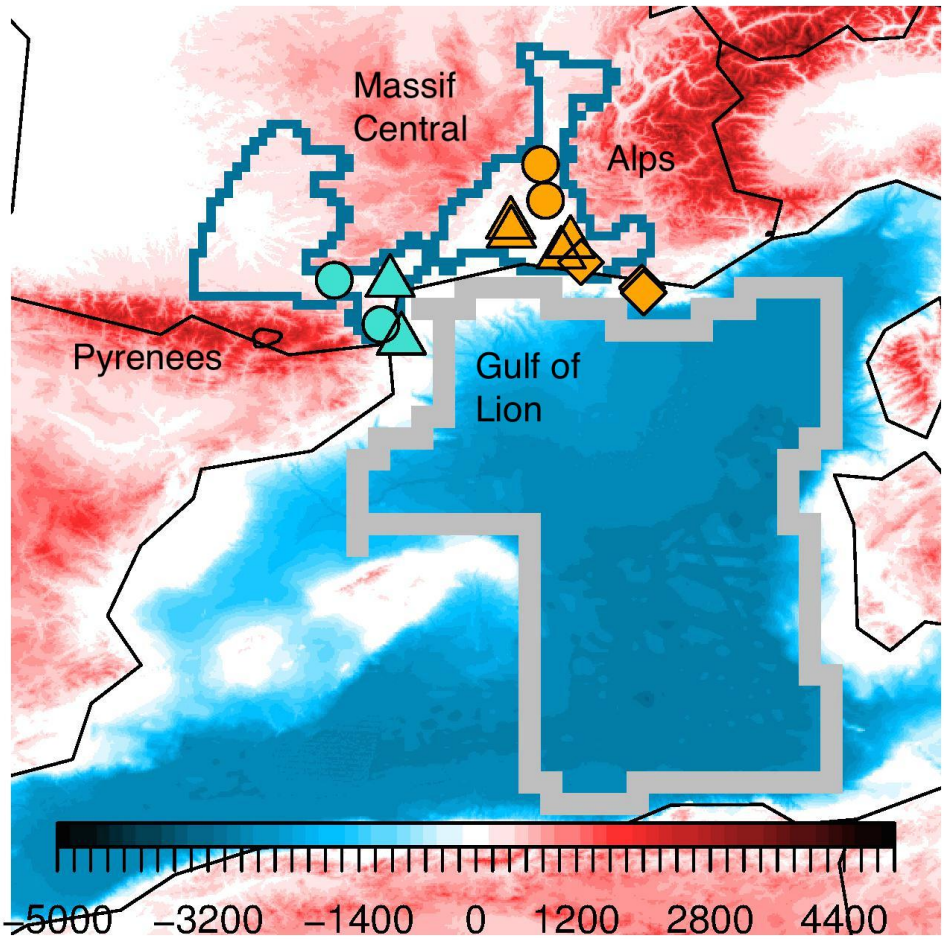

Figure A.1.: Orography (shaded in red) and bathymetry (shaded in blue) from ETOPO1 (Amante and Eakins (2009)) in Mistral and Tramontane regions (in m). Analysis areas in Mistral and Tramontane valleys (outlined in blue) and Mediterranean Sea (outlined in gray), location of stations for gust time series in Mistral area (orange symbols) and Tramontane area (turquoise symbols) in the valleys (circles), in the plains (triangles), and close to the coast (squares).

A.2. Observational Data

Mistral and Tramontane time series and two gridded observational surface wind data sets are used in this study, one for evaluation over France, and one for evaluation over the Mediterranean Sea.

A.2.1. Mistral and Tramontane Areas

Figure A.1 shows the western Mediterranean Sea area. Altitudes and distances to the coast are used to identify Mistral and Tramontane-affected regions in France and over the Mediterranean Sea, as explained below.

This study deals with areas below 600 m altitude in the Rhône and Aude valleys, which are less than 270 km away from the coast of the Mediterranean Sea (outlined in blue in Figure A.1). The altitude information came from ETOPO1, a 1 arc-minute global relief model of Earth's surface (Amante and Eakins (2009)), interpolated to a 0.1° grid. The distance to the coast was calculated for each land grid cell within this area. The narrowest parts of both valleys are about 40 km wide, which is close to the grid spacing of the 0.44° simulations. The area outlined in gray in Figure A.1 indicates the part of the Mediterranean Sea that is of interest in this study. It includes the main parts of the western Mediterranean Basin that are influenced by Mistral and Tramontane winds. The areas south of the Balearic Islands and southeast of Corsica and Sardinia were excluded because the islands modify the wind speed by changes in surface roughness and orographic effects.

A.2.2. Mistral and Tramontane Time Series

The daily gust time series in the Mistral and Tramontane areas provide data of gusts from the dominant Mistral and Tramontane direction, with velocities greater than 16 m/s, observed at each station. Jacq et al. (2005) used this threshold to identify Mistral days. Gusts above this value have been found to cause damage to forests in complex terrain (Jungo et al. (2002) and Schmidtke and Scherrer (1997)). Gust observations from 13 stations are available for the period 2000–2008. Table A.1 indicates the station locations, and the Mistral or Tramontane wind direction at each station. Figure A.1 shows the locations of the stations.

Table A.1.: List of stations used for time series generation.

Station Name	Longitude (°E)	Latitude (°N)	Direction of Gusts (°)
Mistral			
Montélimar	4.75	44.56	320–040
Orange	4.81	44.14	320–030
Nimes-Courbessac	4.40	43.86	320–040
Nimes-Garons	4.41	43.76	320–040
Istres	4.99	43.51	330–010
Salon	5.10	43.64	330–010
Marignane	5.22	43.42	330–010
Toulon	5.93	43.12	260–340
Cap Cepet	5.95	43.07	260–340
Tramontane			
Carcassonne	2.35	43.21	260–320
Perpignan	2.90	42.70	300–360
Cap Bear	3.13	42.52	300–360
Narbonne	3.00	43.18	260–320

The days of the period from 2000–2008 were partitioned into four classes depending on which wind system occurred: Neither Mistral nor Tramontane ("non-M/T days"), only Mistral, only Tramontane, or Mistral and Tramontane ("M/T days"). A day was considered an observed Mistral day if gusts from the directions given in Table A.1 were observed at least at one station in each of the following parts of the Mistral area:

- Rhône valley: at Montélimar or Orange (orange circles in Figure A.1)
- Plains: at Nimes-Courbessac, Nimes-Garons, Istres, or Salon (orange triangles)
- Coast: at Marignane, Toulon, or Cap Cepet (orange squares).

For an observed Tramontane day, gusts must have been present at least at one station in each of two areas:

- Carcassonne or Perpignan (turquoise circles in Figure A.1)
- Cap Bear or Narbonne (turquoise triangles).

These strong criteria for distinction was used to ensure that only days with contiguous flow stretching along the entire valley and reaching the coast were taken into account,

while days with an interfering sea breeze or valley winds on smaller scales were omitted. Table A.2 shows the resulting numbers of days for each class.

Table A.2.: Numbers of days with Mistral and Tramontane occurrence.

2000–2008	Tramontane	no Tramontane	
Mistral	565	66	631
no Mistral	844	1813	2657
	1409	1879	3288

Table A.3 shows the Pearson correlation coefficient for indicator time series of days with Mistral only (M), Tramontane only (T), both at same time (B) and none of both (N). For binary variables, this coefficient – also called phi-coefficent – can not neccessarily reach 1 (-1) for perfect (anti-)correlation. The maximum possible correlation depends on the number of TRUE and FALSE values in both time series to be correlated (Warrens (2008)). Therefore, the correlation values of Mistral only cases (66 in the time period of this study) are generally lower than those of the other situations. The Pearson correlation coefficient is positive (negative) if a situation occurs more (less) often after another situation than expected for a random distribution of N, M, T, and B situations. All four situations are positively correlated with the same time series shifted by one day (diagonal in Table A.3), but for Mistral this correlation is very low. Mistral situations are preceded by a day with neither Mistral nor Tramontane in 75.76 % of the cases and followed by a day with both Mistral and Tramontane in 37.88 % of the cases. Days with both winds occuring are often followed by Tramontane only days (37.35 %) or days with both winds (49.91 %).

Table A.3.: Pearson correlation coefficient for observed time series of days with Mistral only (M), Tramontane only (T), both at same day (B) and none of both (N).

	N(t-1)	M(t-1)	T(t-1)	B(t-1)
N(t)	+0.46	–0.06	–0.16	–0.40
M(t)	+0.06	+0.04	–0.05	–0.03
T(t)	–0.27	–0.01	+0.20	+0.12
B(t)	–0.32	+0.08	–0.01	+0.40

A.2.3. SAFRAN Data Set

The "Système d'Analyse Fournissant des Renseignements Atmosphériques à la Neige" (analysis system to provide data for snow models, SAFRAN) is a reanalysis product over France (Vidal et al. (2010); Quintana-Seguí et al. (2008)). It consists of a gauge-based analysis system utilizing an optimal interpolation method with 615 climatically homogeneous zones covering France. SAFRAN includes information on variables such as precipitation, mean air temperature, and wind speed - but not wind direction - which are calculated every 6 hours. For this analysis, daily mean surface wind speed data on a 0.1° grid for the period 2000–2008 are used.

A.2.4. QuikSCAT Data Set

QuikSCAT is a satellite instrument measuring wind speed and wind direction over the oceans. It was operational from 1999 to 2009. Full years of data are available for 2000–2008 on a 25 km grid. The QuikSCAT technical mission requirements included wind speed measurement accuracies of 2 m/s for wind speeds between 3 and 20 m/s, and an accuracy of 10 % for wind speeds between 20 and 30 m/s (Lungu et al. (2006)). The wind direction ambiguity was 20°. Surface wind speeds and wind directions in the area of interest of this study were retrieved up to twice a day, around 6 a.m. and 6 p.m. local time. To compute the daily means, the two daily measurements at the same location are averaged. Data contaminated by rain events are omitted.

QuikSCAT has been used for wind speed analysis in the Mediterranean (e.g., Accadia et al. (2007); Ruti et al. (2008)), as well as in many other regions (Dorman et al. (2013); Risien and Chelton (2006)). QuikSCAT data have been validated with buoy data in the Gulf of Lion for the period 2000–2005 (Accadia et al. (2007); Ruti et al. (2008)), showing a bias of about 0.4–0.9 m/s, and an RMSE of about 1.5 m/s. Ruti et al. (2008) found the bias of QuikSCAT compared to buoys to be higher for high wind speeds. This is consistent with results for the time interval of this study (not shown).

A.2.5. Observed Daily Mean Surface Wind Speed

Figure A.2 shows the mean surface wind speed in 2000–2008 calculated from SAFRAN data over France and QuikSCAT data over the western Mediterranean Sea, sorted according to the Mistral and Tramontane occurrences in the observed time series described in Section A.2.2. On non-M/T days, the mean wind speed over France is less than 5 m/s, and 4–8 m/s over the Mediterranean Sea. On Mistral days, the mean wind speed in Southern France (mainly in the Rhône valley) is greater than 4 m/s. The wind speed in the eastern Gulf of Lion also increases, and reaches 8–12 m/s. On Tramontane

days, the mean wind speed in the Aude valley reaches values of 4–8 m/s, and in the Gulf of Lion, it reaches values greater than 10 m/s. If both Mistral and Tramontane winds occur simultaneously, the wind speed in southern France and the Mediterranean Sea increases to more than 15 m/s.

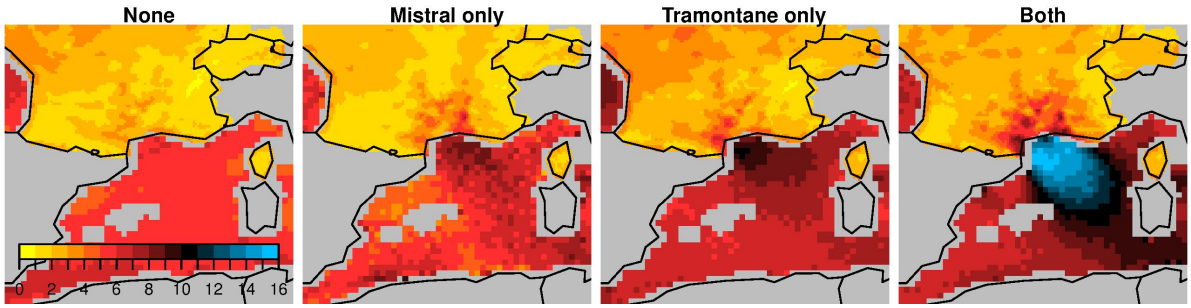

Figure A.2.: Mean wind speed (m/s) from SAFRAN and QuikSCAT data on days in 2000–2008 with neither Mistral nor Tramontane (left), only Mistral (second from left), only Tramontane (third from left) and Mistral and Tramontane together (right). The number of days in each category is given in Table A.2.

A.3. Simulations

All the regional climate simulations in this study are part of the Med-CORDEX framework (Ruti et al. (2016)) and the HyMeX programme (Drobinski et al. (2014)). Simulations were performed on the Med-CORDEX domain covering the Mediterranean Sea and Black Sea, as well as the surrounding land areas, with ERA-Interim as the driving data. For each model within this study, a simulation on a 0.44° grid is available. For most models, a simulation with a higher resolution (i.e. a more dense grid spacing of 0.088–0.22°) is available as well. Some basic properties of the models are described in this section. The simulations are identified by the name of the institution where the simulation was performed, followed by the name of the model employed.

A.3.1. ERA-Interim

In this study, ERA-Interim is used as a reference for classifying days based on the occurrence of Mistral and Tramontane-permitting sea level pressure patterns, and is also used as the forcing for all the regional climate simulations within this study. ERA-Interim is a reanalysis product (Dee et al. (2011)) calculated with a resolution of about 80 km. ERA-Interim data for sea level pressures, surface wind speeds, and surface wind directions were obtained from the European Centre for Medium-Range Weather Forecasts (ECMWF) database.

A.3.2. Regional Climate Models

ALADIN is the limited-area version of ARPEGE, a global spectral model which is used operationally at Météo-France. The ALADIN simulations in this study were performed by the Centre National de Recherches Météorologiques (CNRM) with ALADIN version 5.2 on 0.44° and 0.11° grids. A detailed description of the model can be found in Colin et al. (2010) and Herrmann et al. (2011), who studied the influence of the model configuration on wind speed over the Mediterranean Sea.

The Weather Research and Forecasting (WRF) model developed by the National Center for Atmospheric Research (NCAR) is the only model in this study that is nudged to wind, temperature, and humidity ERA-Interim fields above the boundary layer. Another notable point is that no subgrid-scale orography is considered in this version of WRF. Within this study, WRF simulations with 0.44° and 0.18° grid spacing were performed by Institut Pierre Simon Laplace (IPSL) using WRF 3.1.1. An introduction to WRF 3 is given in Skamarock et al. (2008). More details about the configuration and set of parameterizations can be found in Flaounas et al. (2013) or Stéfanon et al. (2014).

PROMES simulations with 0.44° and 0.22° grid spacing were performed by Universidad de Castilla-La Mancha (UCLM), where the model also was developed. The PROMES model is described in Domínguez et al. (2010).

The COSMO-CLM (CCLM) model (Rockel et al. (2008); Kothe et al. (2014)) is the climate version of the COSMO model, which is used by the German Weather Service for operational weather forecasts. Simulations were performed by Goethe Universität Frankfurt (GUF) with CCLM 4-8-18 on 0.44° and 0.088° grids, and by Centro Euro-Mediterraneo sui Cambiamenti Climatici (CMCC) with CCLM 4-8-19 on a 0.44° grid.

The LMDZ simulation with 0.44° grid spacing was performed by Laboratoire de Météorologie Dynamique (LMD), where the model was developed. The model version LMDZ 4 is described in Hourdin et al. (2006).

A.3.3. Roughness Length Parameterizations

The roughness length, z_0, is a key parameter for surface wind parameterizations. Over land surfaces, it depends on the land use and annual cycle of vegetation (Lawrence and Slingo (2004a,b)), as well as sub-grid scale orography (Georgelin et al. (1994)). The z_0 calculation differs in regional climate models. The roughness length varies depending on waves – and therefore on wind speed – over the sea surface. A classical parameterization of sea surface roughness was introduced by Charnock (1955). The Charnock formula is

$$z_0 = \frac{\alpha}{g} \cdot u_*^2 \tag{A.1}$$

Here, α denotes the Charnock parameter, g the gravity constant, and u_* the friction velocity. The numerical value of α varies between models. GUF-CCLM uses the rather small value of α=0.0123, while the value used by UCLM-PROMES is almost three times as large (α=0.032). CNRM-ALADIN (α=0.021) and IPSL-WRF (α=0.0185) use values in between these extremes. To avoid a zero roughness length, the Charnock formula is slightly modified in numerical calculations. A constant value of $1.59{\cdot}10^{-5}$ m is added to the roughness length, e.g., in IPSL-WRF, while CCLM uses the maximum value of u_* or free convection scaling velocity w_* (whichever is larger) in the Charnock formula (Doms et al. (2011)). Several versions of this formula have been discussed (e.g., Powell et al. (2003); Donelan et al. (1993)), taking into account further effects, such as those of fetch (Lange et al. (2001)), seafloor depth (Jiménez and Dudhia (2014)), spray (Andreas (2004); Golbraikh and Shtemler (2013)), and swell (Potter (2015)). Cavaleri et al. (2012) give an overview of the influence of waves on air–sea exchanges.

The friction velocity u_* depends on momentum fluxes at the surface τ_s and density ρ:

$$u_* = \sqrt{\frac{\tau_s}{\rho}} \tag{A.2}$$

Through τ_s, the friction velocity depends on the roughness length and needs to be calculated iteratively. The procedure of calculating u_* varies between models.

A.3.4. Spatial and Temporal Interpolation of Simulation Data Sets

All simulated sea level pressure data sets were bilinear-interpolated to a common 0.25° grid, while surface wind data sets were bilinear-interpolated to the SAFRAN grid for evaluation over France, and to the QuikSCAT grid for evaluation over the Mediterranean Sea. The daily means of simulation data were optained directly from the MedCORDEX data base. Thus, the simulation daily means are means over the whole day, while QuikSCAT daily means are the average of two measurements per day.

A.4. Methods

The main focus of this study is the evaluation of surface wind patterns during Mistral and Tramontane events. Therefore, the days of interest are those on which both the simulation and observation agreed on whether or not an M/T occurred. Mistral and Tramontane are driven by large scale flow settings that favor the channeling of winds in the Rhône and Aude valleys. A pressure low in the Genoa area is a known feature of these events. Therefore, one way to identify Mistral and Tramontane days could be using the minimum sea level pressure in the Genoa area. When regarding the 631 (1409) days with lowest ERA-Interim sea level pressure in this area in 2000—2008 as Mistral (Tramontane) days, the agreement with the observed M/T time series is 55 %. To improve this value, an alternative way was used to identify M/T days from sea level pressure fields: A classifying algorithm, including Empirical Orthogonal Function (EOF) analysis and a Bayesian network, was used to decide on which days the large-scale sea level pressure fields were well represented in the simulations, and thus identify the large-scale M/T candidates. An introduction to EOF analysis can be found in, e.g., von Storch and Zwiers (2001). For an introduction to Bayesian networks, see e.g., Scutari (2010).

A.4.1. EOF Analysis

To compare the large-scale features, an EOF analysis of the ERA-Interim daily mean sea level pressure field in the area –20–20° East and 25–55° North are carried out for the period 2000–2008. This area is chosen because it includes the Mistral and Tramontane regions, as well as the surrounding areas, which are most important for the development of a Mistral and Tramontane-permitting pressure system, while other parts (especially the eastern region of the Med-CORDEX domain) would mainly add noise to the EOFs.

EOF Patterns

Figure A.3 shows the mean sea level pressure in the western Mediterranean region for ERA-Interim, and the simulation biases with respect to ERA-Interim. All biases are calculated as simulation minus reference. The simulations done with IPSL-WRF, UCLM-PROMES, and LMD-LMDZ show a mostly negative bias, while the biases of both GUF-CCLM and CMCC-CCLM are mostly positive. CNRM-ALADIN has a positive bias at the Mediterranean Sea, but a negative bias in parts of Europe and Africa.

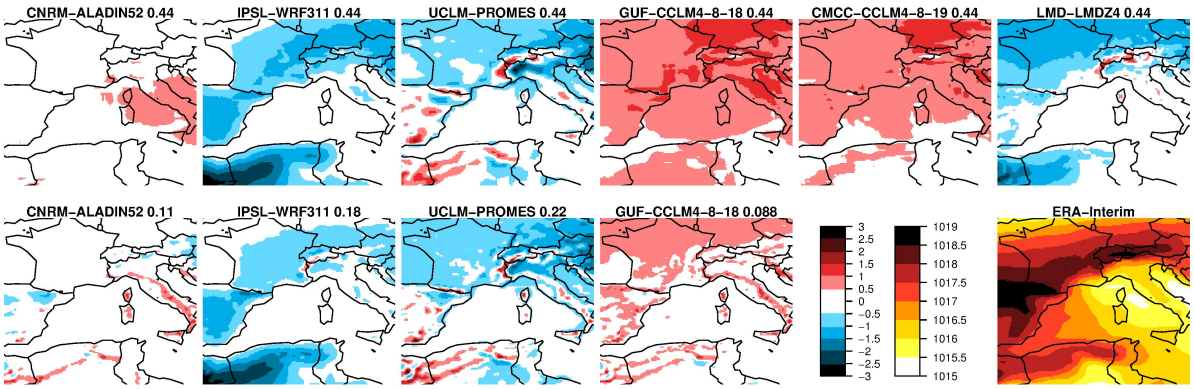

Figure A.3.: Sea level pressure bias of simulations and mean sea level pressure of ERA-Interim in 2000–2008 (hPa). Left color scale is for the bias plots, right color scale is for the ERA-Interim plot.

Figure A.4 shows the first five EOFs from ERA-Interim. The first EOF explaines 43.15 % of the variance and features a high pressure system over southern England. The second and third EOFs show dipole patterns and explain 24.80 % and 14.28 % of the variance. The fourth and fifth EOFs already feature quadrupole patterns and explain 5.28 % and 3.55 % of the variance.

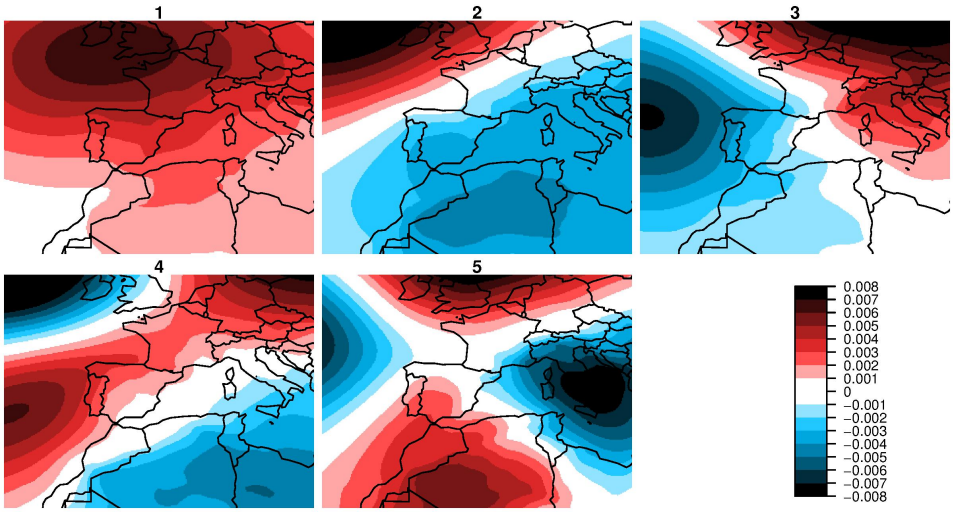

Figure A.4.: First five EOFs calculated from ERA-Interim daily mean sea level pressure fields 2000–2008 (arbitrary units).

Principal Components

The principal components (PCs) of the first 100 EOFs were calculated for ERA-Interim (which is the reference data set), as well as for each of the simulation data sets (i.e., simulation data are projected to the reference EOFs). This number of EOFs is chosen because it is high enough to cover a large part of the variance (99.97 %) and sufficiently convenient to work with. A loss-less description of the sea level pressure fields of all 3288 days in the years 2000–2008 would need 3288 EOFs. Additionally, this choice reduces the noise caused by small-scale variations represented by higher-order EOFs.

Figure A.5 shows the annual cycle of the first five ERA-Interim principal components. The first principal component shows a positive value during winter and a negative or almost zero value during the rest of the year. The second principal component shows an inverse annual cycle with negative values from October till March and positive values from April to September. The higher order principal components show a less pronounced annual cycle. Both the first and second principal component correlate with the Mistral and Tramontane time series, while the third principal component anti-correlates with the Mistral and Tramontane time series.

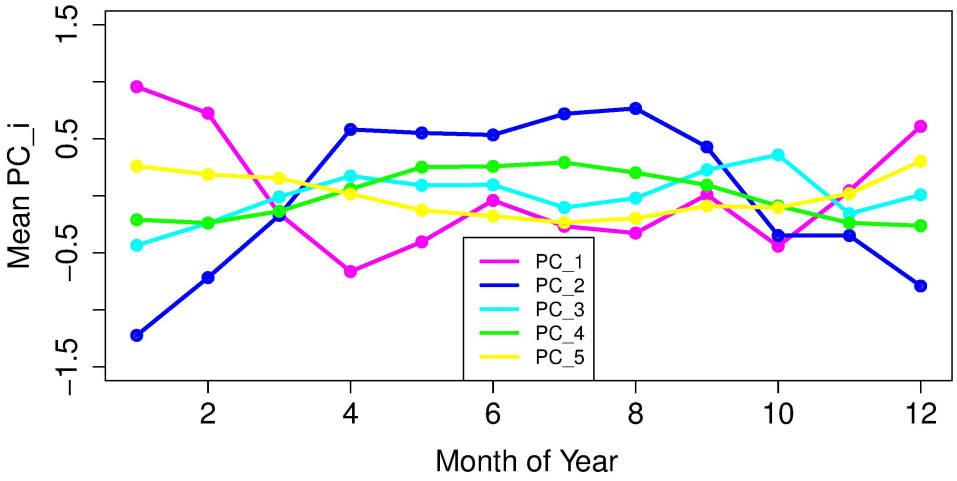

Figure A.5.: Monthly means of first five ERA-Interim principal components.

Figure A.6 shows the correlations between the first 20 ERA-Interim principal components and simulated principal components. The first principal component has the highest correlation for all simulations, while the correlation decreases for higher-order principal components.

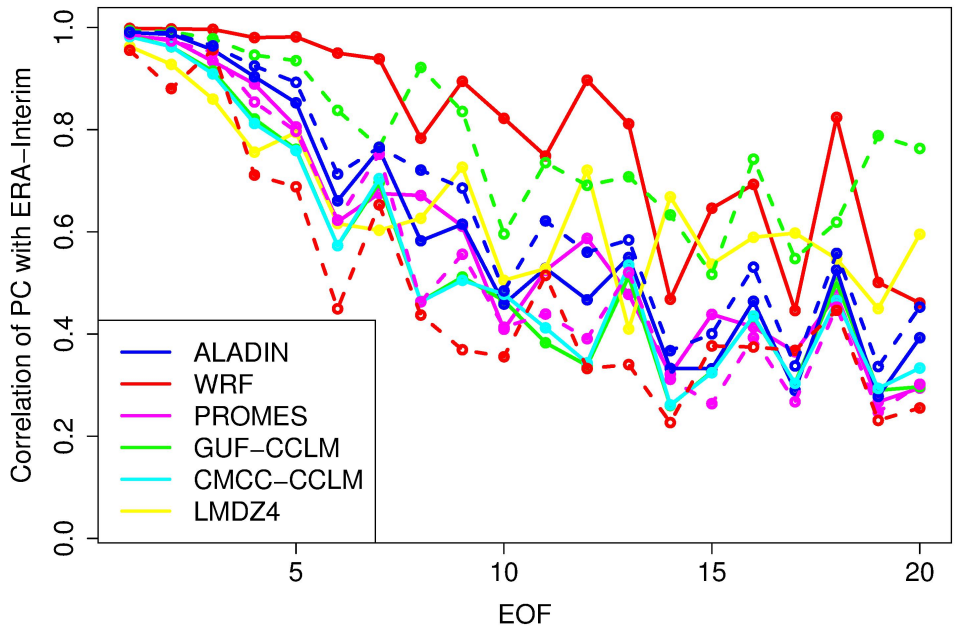

Figure A.6.: Correlation of simulation and ERA-Interim principal components. Solid lines indicate 0.44° runs, dashed lines indicate smaller grid spacing runs.

A.4.2. Classifying Sea Level Pressure Patterns

The classifying algorithm consists of three parts: preparation of input data, structure learning and training, and output processing.

Preparation of Input Data

Reference and simulation principal components were normalized (indicated by exponent n) to compensate for different amplitudes and mean values:

$$PC_i^n(t) = \frac{PC_i(t) - \mu_i}{\sigma_i} \tag{A.3}$$

Here, μ_i denotes the mean, and σ_i the standard deviation of the ith principal component PC_i. The day is denoted by t. The normalization allowed the Bayesian network to assign a realistic weight to all the principal component time series.

Structure Learning and Training

The Bayesian network is trained using the normalized ERA-Interim principal components and the observed time series of Mistral and Tramontane days as training data.

The Bayesian network obtained its structure using a hill-climbing algorithm (Tsamardinos et al. (2006)). The TRUE/FALSE time series were transformed to 1 (TRUE) and 0 (FALSE) values. Figure A.7 shows the Bayesian network after structure learning. During the training procedure, weights were given to the connections (arcs) between input nodes PC_i and the output node M/T. Additionally, some arcs might have been removed during training if the Bayesian network did not find a connection between a principal component and the time series.

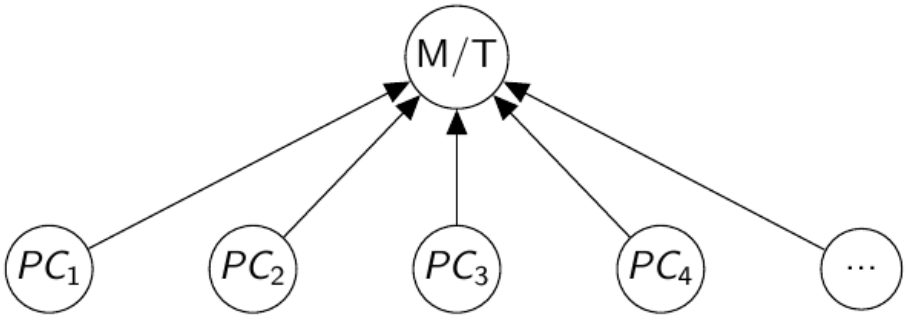

Figure A.7.: Structure of the Bayesian network. The normalized principal components (PC) are used as inputs for the lower row of nodes. The upper node M/T denotes the output, a number which can be related to the probability of a M/T situation being present or not.

Output Processing

After the training, the Bayesian network determines on which days the simulations' sea level pressure fields show a Mistral and Tramontane-permitting pattern. When using a simulation's normalized principal components for one day as input for nodes PC_i, the trained Bayesian network assigns a score value to node M/T. Higher values correlate with an increasing probability of a Mistral or Tramontane event on that day. The transformation from a continuous output variable to a TRUE/FALSE variable was done by keeping the total number of Mistral and Tramontane days in the time interval 2000–2008 the same as that in the observed time series. Therefore, for each simulation, the 631 days with highest Mistral probability and 1409 days with highest Tramontane probability were regarded as Mistral and Tramontane days, respectively (see Table A.2).

After the classification procedure, a time series of M/T patterns is available for each simulation. It consists of the information of whether or not a Mistral and/or Tramontane-

permitting sea level pressure pattern was present in the simulation on that day. In subsequent steps of this discussion, the only days considered are those days on which the time series produced by the classification algorithm and the observed time series agree on whether or not an M/T pattern was present.

Length of Training Period

To verify that the training period 2000–2008 contains enough Mistral and Tramontane cases to reach a sufficient level of training, the observed M/T time series and the ERA-Interim principal components are split in two parts – the training data set and the validation data set. The days are randomly chosen to belong to one of the two data sets. The Bayesian network is trained with the training data set. Then, the output of the Bayesian network is compared to observations for both training and validation data set. When using 7 or 8 years of training data, the Bayesian networks performs almost equally well for both the training and the evaluation data set (Figure A.8). Longer training periods have been tested for the years 1981–2010, and do not significantly improve the percentage of correctly predicted patterns (not shown).

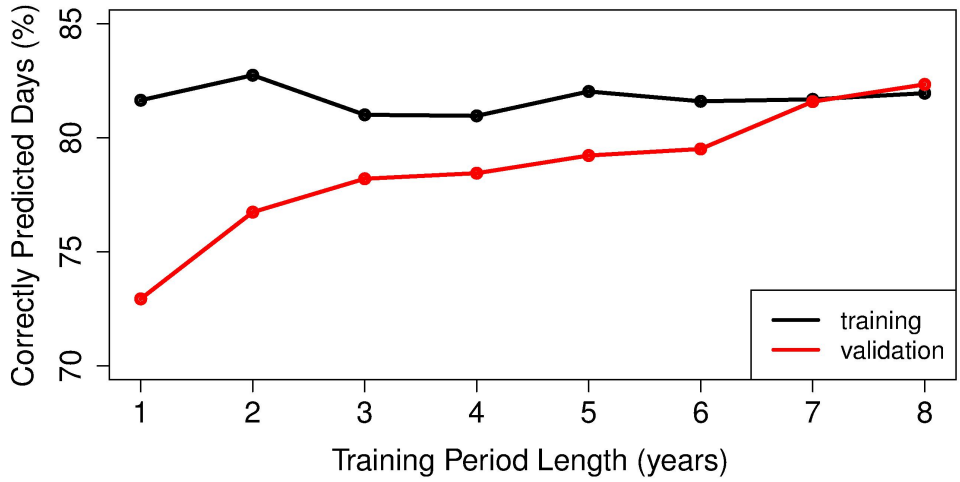

Figure A.8.: Percentage of corretly predicted M/T situations from ERA-Interim sea level pressure fields as function of training period length for the years 2000-2008. The validation data set consists of all days in this time interval, which are not included in the training data set.

A.4.3. Wind Direction Bias and RMSE over the Mediterranean Sea

To evaluate the simulations in terms of surface wind direction, QuikSCAT was chosen as reference (no gridded wind direction data over France is available). For each grid cell, the average wind direction of the simulation ($\beta_{sim,t}$) and QuikSCAT ($\beta_{obs,t}$) were calculated from zonal (u) and meridional (v) wind speed. Only data points with two measurements per day were taken into account to minimize the effects of land–sea wind systems. The wind direction difference between the simulation and QuikSCAT was calculated for each day t:

$$\beta_t = \beta_{sim,t} - \beta_{obs,t} \tag{A.4}$$

The average of the daily differences is the wind direction bias β_{bias}:

$$\beta_{bias} = \frac{1}{N}\sum_{t=1}^{N}\begin{cases} \beta_t & , \quad |\beta_t| \leq 180^\circ \\ (|\beta_t| - 360^\circ)\cdot\frac{\beta_t}{|\beta_t|} & , \quad |\beta_t| > 180^\circ \end{cases} \tag{A.5}$$

This formula takes into account that the difference in wind direction has to be less than $\pm 180^\circ$. The wind direction root mean square error (RMSE) β_{RMSE} is calculated accordingly:

$$\beta_{RMSE} = \sqrt{\frac{1}{N}\sum_{t=1}^{N}\begin{cases} \beta_t^2 & , \quad |\beta_t| \leq 180^\circ \\ (|\beta_t| - 360^\circ)^2 & , \quad |\beta_t| > 180^\circ \end{cases}} \tag{A.6}$$

A.4.4. Fetch

Within this study, the evolution of errors along the wind track is of interest. To perform this evaluation over the Mediterranean Sea - where Mistral and Tramontane are not channeled through valleys - a fetch calculation was performed. Fetch in this sense is defined as the distance an air parcel traveled above the sea surface before reaching its current position.

To calculate an estimated fetch from the daily mean wind speed and direction, uncertainties in the exact path of the air parcel have to be taken into account. Therefore, the average fetch of a grid cell with a given daily mean wind direction ϕ was calculated in two steps, following the approach for calculating the effective fetch in Lange et al. (2001). In the first step, the distance $d(\phi_i)$ to the next coastal grid cell in each direction was calculated for all directions in 1° intervals. In the second step, the average fetch

of wind coming from direction ϕ was calculated by a weighted average of the interval $\phi \pm 90°$:

$$fetch(\phi) = \frac{1}{90} \sum_{\phi_i = \phi - 90°}^{\phi + 90°} \left[cos^2(\phi - \phi_i) \cdot d(\phi_i) \right] \tag{A.7}$$

A.5. Results

A.5.1. Classifying Tramontane and Mistral Days

Table A.5 shows the number and percentage of days on which the observed time series and the simulation time series produced by the Bayesian network are in agreement. All the simulation time series agree with the observed time series on more than 74 % of the days. ERA-interim, which was used as training data, shows the highest percentage of correctly predicted days (82 %). IPSL-WRF shows the highest percentage of correct days of all the simulations. The observed time series includes 1813 non-M/T days. The classifying algorithm finds a non-M/T pattern on more than 85 % of these days in all the simulations. Non-M/T days are identified correctly in 85.3–91.2 % of the cases. The rare Mistral-only events are identified correctly in less than 20 % of the days, while the numerous Tramontane-only events are identified correctly in 55.6–64.0 % of the cases. M/T patterns are identified correctly in 69.6–79.8 % of the cases. This leads to a false alarm ratio (either Mistral or Tramontane or both winds were predicted, but none of them observed) of 8.8–14.7 % of the non-M/T cases, which corresponds to 4.9–8.1 % of all days. Only M/T and non-M/T days on which the simulation and observed time series agree on the occurring wind systems are taken into account in subsequent steps of this study.

Table A.4 shows the Pearson correlation coefficient for M/T time series as Table A.3, but for GUF-CCLM 4-8-18 at 0.088°. The other simulations show similar Pearson correlation coefficients for most cases, while the value for the persistence of Mistral only days varies between simulations. CNRM-ALADIN 0.44°, IPSL-WRF 0.18°, and ERA-Interim show a small negative value, while the other simulations show positive values.

Table A.4.: Pearson correlation coefficient for time series of Mistral only (M), Tramontane only (T), both at same day (B) and none of both (N) for GUF-CCLM 4-8-18 at 0.088°.

	N$(t-1)$	M$(t-1)$	T$(t-1)$	B$(t-1)$
N(t)	$+0.51$	-0.08	-0.20	-0.42
M(t)	$+0.03$	$+0.15$	-0.05	-0.03
T(t)	-0.32	-0.02	$+0.28$	$+0.11$
B(t)	-0.31	$+0.08$	-0.05	$+0.43$

Table A.5.: Number of days with wind systems correctly predicted by Bayesian network.

Simulation	Grid (°)	None		Mistral		Tramontane		Both		Sum	
		Days	%	Days	%	Days	%	Days	%	Days	%
CNRM-ALADIN	0.44	1601	88.3	3	4.5	486	57.6	432	76.5	2522	76.7
	0.11	1589	87.6	10	15.2	504	59.7	429	75.9	2532	77.0
IPSL-WRF	0.44	1611	88.9	10	15.2	540	64.0	439	77.7	2600	79.1
	0.18	1626	89.7	5	7.6	514	60.9	451	79.8	2596	79.0
UCLM-PROMES	0.44	1585	87.4	8	12.1	482	57.1	410	72.6	2485	75.6
	0.22	1561	86.1	10	15.2	469	55.6	409	72.4	2449	74.5
GUF-CCLM	0.44	1601	88.3	10	15.2	510	60.4	420	74.3	2541	77.3
	0.088	1546	85.3	13	19.7	507	60.1	403	71.3	2469	75.1
CMCC-CCLM	0.44	1580	87.1	11	16.7	493	58.4	414	73.3	2498	76.0
LMD-LMDZ	0.44	1594	87.9	8	12.1	501	59.4	393	69.6	2496	75.9
ERA-Interim		1654	91.2	12	18.2	580	68.7	449	79.5	2695	82.0
observed time series		1813	-	66	-	844	-	565	-	3288	-

A.5.2. Spatial Wind Patterns

Wind Speed

Figures A.9 and A.10 show the wind speed bias of the simulations with respect to SAFRAN and QuikSCAT, for days on which observation and simulation agree on an M/T situation being present or not.

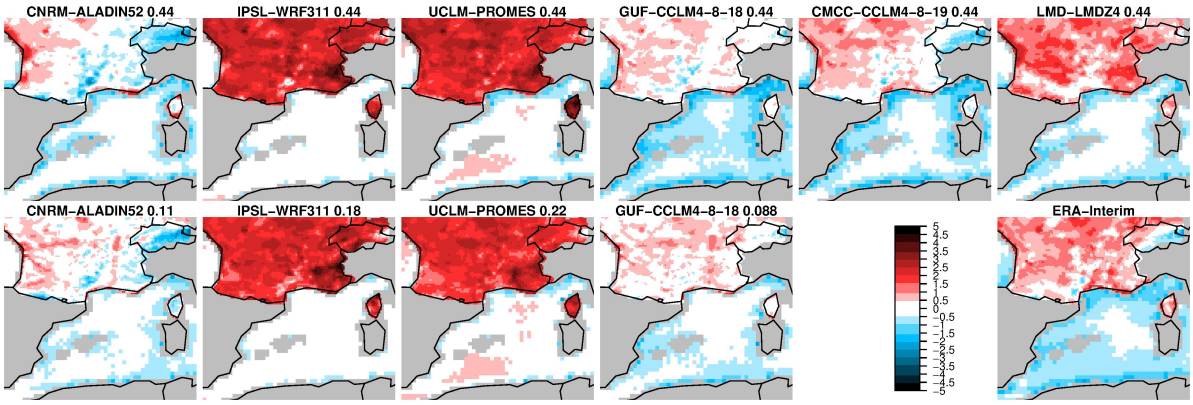

Figure A.9.: Wind speed bias (m/s) for non-M/T days.

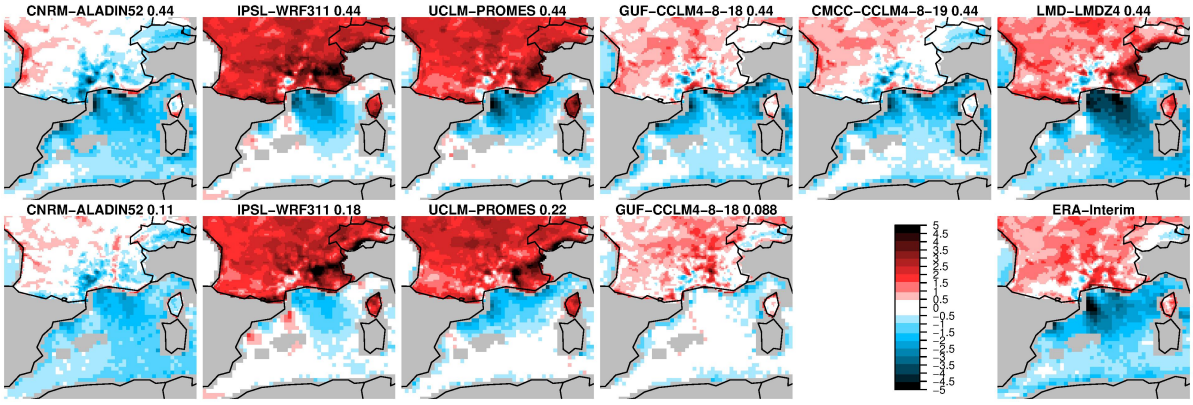

Figure A.10.: Wind speed bias (m/s) for M/T days.

On non-M/T days (Figure A.9), all simulations show a more negative bias over the Mediterranean Sea close to the coast, than over the open sea. The bias of simulations with the smaller grid spacing is smaller in this area. Additionally, these runs show higher wind speeds than their coarser counterparts over large areas.

On M/T days (Figure A.10), all simulations show a negative bias in the Gulf of Lion. The bias is larger at the sides of the main flow than at its center. Here, the runs with the smaller grid spacing show a smaller absolute bias. The bias is more negative on winter M/T days than on summer M/T days. At the same time, the observed winter M/T wind speed is higher than the summer M/T wind speed (not shown). Interpolation effects in the valleys make it difficult to evaluate wind speeds. Therefore, processes in the valleys will be discussed in more detail in the next section. Furthermore, IPSL-WRF and UCLM-PROMES overestimate the wind speed over France, which makes a discussion of spatial patterns in comparison to the other models difficult.

Figure A.11 shows the wind speed RMSEs of GUF-CCLM with respect to QuikSCAT and SAFRAN. The overall pattern is similar for all simulations. Over France, the RMSEs of IPSL-WRF and UCLM-PROMES are higher than those of the other simulations. Over the Mediterranean Sea, IPSL-WRF has the smallest RMSE, while UCLM-PROMES has the largest (not shown). On M/T days, the highest RMSE occurs at the sides of the main flow – also the area of the largest bias – in the Gulf of Lion for all simulations. The simulations with smaller grid spacing have a smaller RMSE than their coarser counterparts.

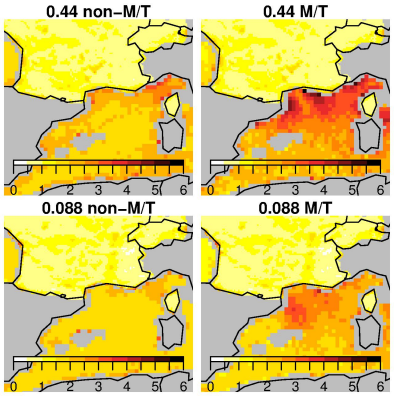

Figure A.11.: Wind speed RMSE (m/s) for non-M/T and M/T days simulated with GUF-CCLM 4-8-18 at 0.44 and 0.088° grid spacing.

Wind Direction

Figures A.12 and A.13 show the wind direction biases. On non-M/T days (Figure A.12), IPSL-WRF, UCLM-PROMES, LMD-LMDZ, and ERA-Interim show a mainly positive wind direction bias (indicating that the wind comes from a direction that is too far clockwise). For CNRM-ALADIN, GUF-CCLM, and CMCC-CCLM, the absolute bias is smaller. On M/T days, the bias of CNRM-ALADIN and GUF-CCLM at 0.088° grid spacing is slightly

positive in the southwestern part of the Gulf of Lion. The bias of UCLM-PROMES and IPSL-WRF is positive in the north, and becomes more negative in the south. Figure A.13 shows that the highest biases occur on the sides of the main flow and in the area where the Mistral enters the region over the Mediterranean Sea.

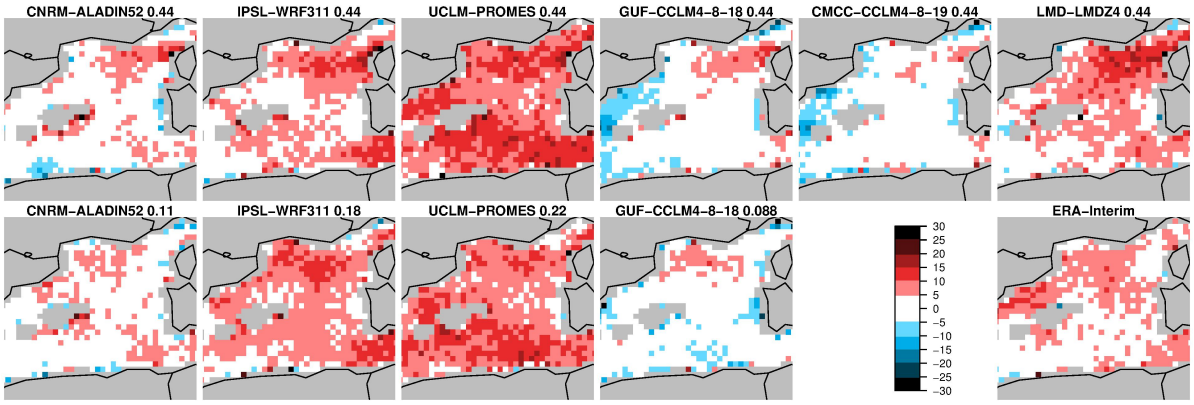

Figure A.12.: Wind direction bias (°) for non-M/T days.

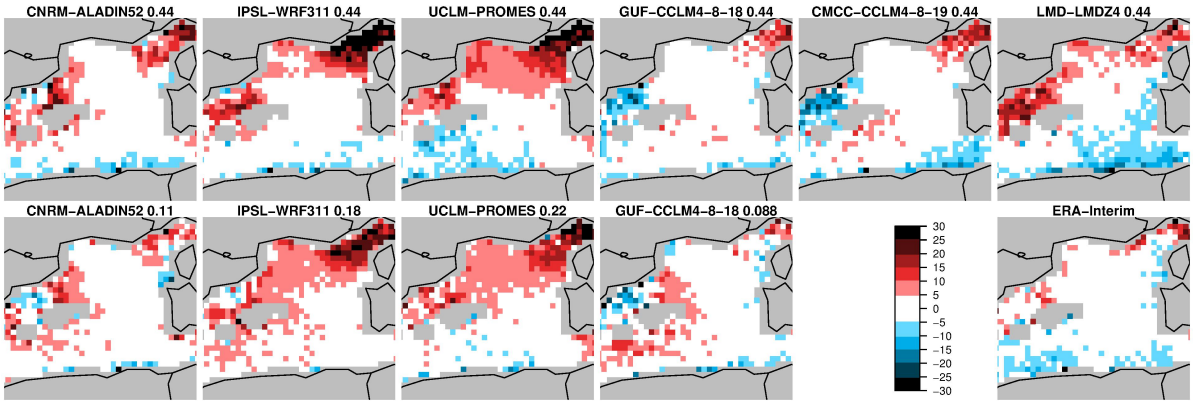

Figure A.13.: Wind direction bias (°) for M/T days.

The surface wind direction RMSE of GUF-CCLM at 0.088° grid spacing is shown in Figure A.14. The other simulations show similar RMSE patterns (not shown). On non-M/T days, the RMSE does not have much structure. On M/T days, the wind direction is reproduced better in the main flow area, but the RMSE increases compared to non-M/T days in the areas close to the Spanish coast.

Table A.6 shows the RMSE within the Gulf of Lion region for all the simulations. ER-A-Interim has the lowest RMSE for both cases, followed by IPSL-WRF. UCLM-PROMES

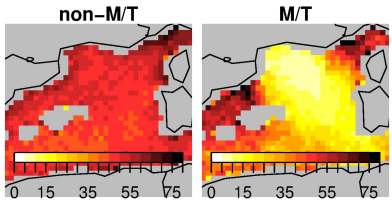

Figure A.14.: Wind direction RMSE (°) of GUF-CCLM4-8-18 at 0.088° grid spacing.

and LMD-LMDZ have higher RMSEs in both cases. The surface wind direction RMSE is smaller on M/T days than on non-M/T days for all the simulations.

Table A.6.: RMSE of wind direction (°) in the Gulf of Lion region.

Model	Grid (°)	non-M/T	M/T
CNRM-ALADIN	0.44	50.02	27.81
	0.11	48.88	28.93
IPSL-WRF	0.44	37.70	24.28
	0.18	37.15	25.96
UCLM-PROMES	0.44	54.60	29.00
	0.22	52.42	28.40
GUF-CCLM	0.44	52.01	26.68
	0.088	49.83	26.08
CMCC-CCLM	0.44	51.68	27.66
LMD-LMDZ	0.44	57.57	33.00
ERA-Interim		36.16	19.47

Influence of Forcing Data

The influence of the forcing data can be estimated by comparing errors during days when ERA-Interim sea level pressure fields agree with observations on M/T situations and days when the simulations sea level pressure patterns agree with observations. When taking into account all days of 2000–2008, the RMSE of ERA-Interim wind speed with respect to QuikSCAT in the Gulf of Lion region is 1.92 m/s. When considering only days on which ERA-Interim pressure fields and observed time series agree on M/T situations, the RMSE stays at about the same value (1.93 m/s). For GUF-CCLM at 0.088° grid spacing, the results are similar: considering all days yields a wind speed RMSE of 2.01 m/s, considering ERA-Interim correct days yields 2.02 m/s, and considering

days with correct model pressure fields yields 1.96 m/s. The other simulations behave similarly – they all show a smaller wind speed RMSE when considering only days on which the simulation M/T situation agree with the observations than when considering days with correct ERA-Interim M/T situations.

When comparing the wind speed RMSE of each simulation of days with M/T situations correctly predicted by ERA-Interim ($RMSE_{ERA}$) and by the simulations ($RMSE_{sim}$), the influence of the forcing data can be estimated by the relative difference in RMSE between both sets of days:

$$d_r = \frac{RMSE_{ERA} - RMSE_{sim}}{RMSE_{ERA}} \tag{A.8}$$

A positive value of d_r indicates an improvement by choosing the days with correctly simulated M/T situations instead of ERA-Interim M/T situations. The relative difference d_r varies between 0.47 % (IPSL-WRF 0.18°) and 4.03 % (GUF-CCLM 0.44°) over the Mediterranean Sea. In the valley areas, d_r varies between –0.61 % (IPSL-WRF 0.44°) and 1.94 % (GUF-CCLM 0.44°).

A.5.3. Along-flow Development

Wind Speed

Figure A.15 shows the observed and simulated mean wind speeds along the wind track in the Tramontane and Mistral valleys and above the Mediterranean Sea (blue and gray areas in Figure A.1) on M/T days and non-M/T days. The observed Mistral wind speed (left column of Figure A.15) has two local maxima. The first local maximum is located in the narrowest part of the valley, about 180 km away from the coast, and the second local maximum is located 100 km away from the coast, where the valley opens. None of the simulations is able to reproduce both maxima. All simulations show an increase in wind speed close to the constriction, but most of the simulations miss the downstream decrease and the second local maximum.

The Tramontane (middle column of Figure A.15) accelerates more continuously until the observed wind speed reaches 6–7 m/s. In both valleys, most simulations show a higher increase in wind speed than SAFRAN when approaching the coast, and almost reach the wind speed measured by QuikSCAT. UCLM-PROMES and IPSL-WRF overestimate the wind speed in both valleys, but do not show an overestimation over the sea. Most simulations show a better agreement with the observations than ERA-Interim. Above the Mediterranean Sea (right column of Figure A.15), the observed wind speed is higher, reaching almost 12 m/s at a distance of 100–300 km away from the coast on M/T days.

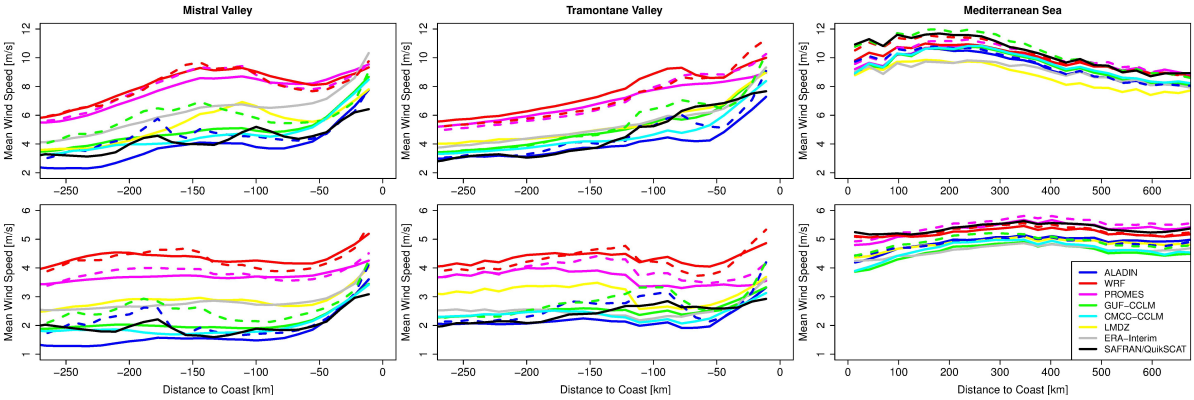

Figure A.15.: Mean SAFRAN/QuikSCAT and simulated wind speed (m/s) in Mistral (left column) and Tramontane (middle column) valleys and above the Mediterranean Sea (right column) on M/T days (upper row) and non-M/T days (lower row).

All simulations except GUF-CCLM at 0.088° grid spacing underestimate the wind speed over the Mediterranean Sea on M/T days as well as on non-M/T days, but are able to reproduce the overall shape of fetch dependence. All simulations except LMD-LMDZ show better agreement with QuikSCAT than ERA-Interim, which also underestimates the wind speed.

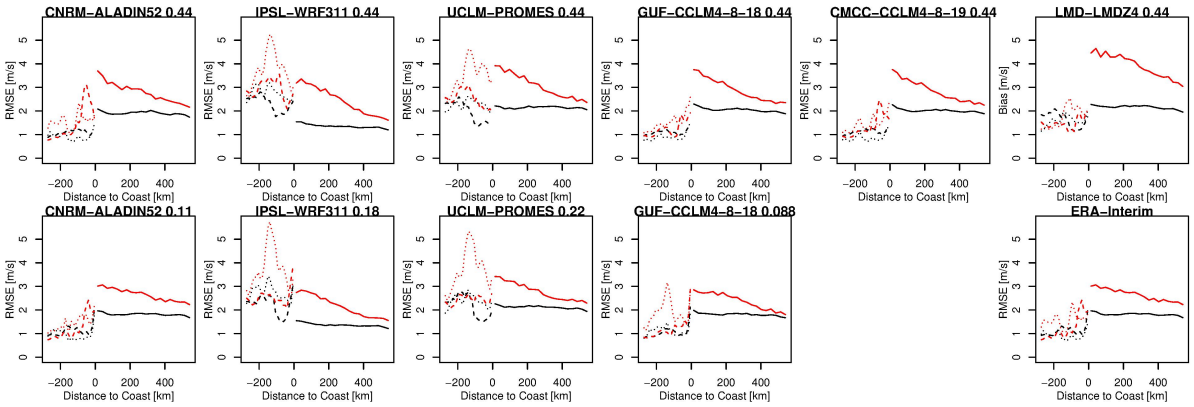

Figure A.16.: Wind speed RMSE (m/s) as function of distance to the coast. On M/T days (red) and non-M/T days (black) in the Mistral valley (dotted line) and Tramontane valley (dashed line), as well as over the Mediterranean Sea (solid line).

Figure A.16 shows the RMSE of simulated wind speed with SAFRAN and QuikSCAT as reference. The highest RMSEs of IPSL-WRF, UCLM-PROMES, and GUF-CCLM at 0.088° grid spacing in the Mistral valley are located 140 km away from the coast at the position of a local minimum in the observed wind speed. The RMSE is also higher in the valleys for UCLM-PROMES and IPSL-WRF than the other models. Above the

Mediterranean Sea, RMSE decreases with increasing distance to the coast, and reaches values close to 2 m/s on non-M/T days. Meanwhile, on M/T days, the RMSE is higher for all simulations.

Wind Direction

Figure A.17 shows the fetch dependence of the wind direction bias. The bias shows a different fetch-dependent behavior on M/T and non-M/T days. To quantify the development of wind direction bias, a linear fit is employed. Table A.7 shows the parameters of the linear fit

$$\beta(x) = \beta_0 + a \cdot fetch. \tag{A.9}$$

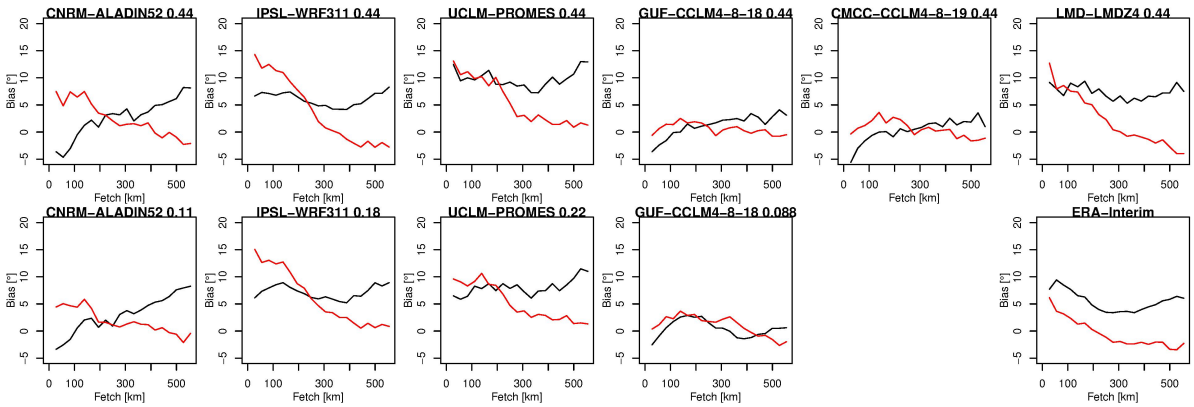

Figure A.17.: Wind direction bias (°) as function of fetch. See Figure A.16 for legend.

On non-M/T days, the fit function shows a positive slope a (indicating a change from counterclockwise to clockwise-rotated wind bias) for most simulations. On M/T days, the slope is negative for all simulations (indicating a change from clockwise to counterclockwise-rotated wind). The intercept β_0 varies strongly between simulations. On M/T days, all simulations show a positive intercept, with UCLM-PROMES and IPSL-WRF reaching values greater than 10°.

Figure A.18 shows the fetch dependence of the wind direction RMSE for GUF-CCLM. All simulations within this study show a similar dependence on fetch (not shown). The RMSE on non-M/T days is higher than on M/T days for all simulations. The RMSE on M/T days decreases strongly with increasing fetch for distances up to 250 km away from the coast, but does not get much better than 20°.

Table A.7.: Fit parameters, intercept (β_0) and slope (a), of wind direction bias (Figure A.17).

		non-M/T		M/T	
Model	Grid (°)	β_0 (°)	a (°/100 km)	β_0 (°)	a (°/100 km)
CNRM-ALADIN	0.44	–2.90	+2.01	+7.49	–1.84
	0.11	–2.39	+1.96	+5.21	–1.22
IPSL-WRF	0.44	+6.44	–0.12	+13.72	–3.58
	0.18	+7.09	+0.02	+14.30	–2.96
UCLM-PROMES	0.44	+9.49	+0.11	+12.01	–2.38
	0.22	+6.44	+0.58	+10.29	–1.87
GUF-CCLM	0.44	–1.68	+1.06	+1.51	–0.33
	0.088	+0.97	–0.19	+3.32	–0.83
CMCC-CCLM	0.44	–2.53	+1.03	+2.22	–0.60
LMD-LMDZ	0.44	+8.01	–0.26	+9.96	–2.82
ERA-Interim		+6.92	–0.52	+3.56	–1.46

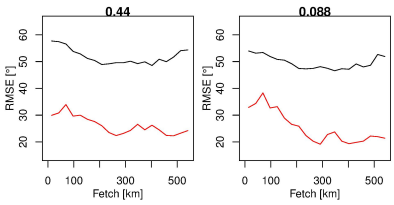

Figure A.18.: Wind direction RMSE (°) as function of fetch for GUF-CCLM 4-8-18 simulations with 0.44 and 0.088 ° grid spacing. See Figure A.16 for legend.

A.6. Discussion

The results presented in the previous section are discussed here. Three types of error sources are identified: large scale pressure patterns, valley effects, and effects over the Mediterranean Sea. Furthermore, the influence of grid spacing is discussed.

A.6.1. Large-Scale Sea Level Pressure Patterns

ERA-Interim shows an agreement of 82 % with the observations' M/T situations, which can be explained by the fact that ERA-Interim was used as training data for the Bayesian network employed in the classification algorithm. ERA-Interim achieves less than 100 % of correctly predicted days, which could partly be explained by the fact that not all EOFs were used for the classification algorithm to eliminate noise. This leads to loss of information needed to reach a perfect score. Additionally, errors in station measurements can cause ambiguities in the training data. The very small number of cases (66 days) in the training data set could explain the low percentage of correctly modeled Mistral-only days. Even though more training data are available for Tramontane-only cases, their percentage of correctly predicted days is lower than that of M/T and non-M/T cases. This could be due to more complex sea level pressure patterns during the Tramontane-only cases. The effect of over training the Bayesian network is unlikely to be present because increasing the number of training days did not reduce the number of correctly predicted days.

When the number of correctly reproduced days from the training data (2695 days) is used as reference, the simulations predict more than 90 % of these days correctly. All models are therefore able to reproduce the M/T-permitting patterns in most cases when ERA-Interim is used as the driving model. Besides ERA-Interim, IPSL-WRF has the highest number of days with correctly represented M/T patterns. It is the only model included in this study that is nudged to ERA-Interim over the planetary boundary layer for temperature humidity and wind, and therefore has an advantage in terms of large-scale pressure fields.

A.6.2. Effects in the Valleys

A possible source of errors in the valleys is the interpolations between valley and mountain grid cells, especially in narrow parts of the valley, for the simulations. The high wind speeds over France in IPSL-WRF simulations could be due to the Yonsei University (YSU) parameterization (Hong et al. (2006)) used in WRF 3.1.1. Draxl et al. (2014) showed that WRF 3.1.1 with YSU tends to produce wind profiles typical for

neutral conditions in the majority of cases. This leads to larger wind speed biases over land than over the sea, where neutral conditions occur more often. UCLM-PROMES also features a positive wind bias over land surfaces in both simulations, which has been found in other areas as well (Domínguez et al. (2010)).

Mistral wind speeds show two local maxima where several hydraulic jumps have been observed in the lower Rhône valley (Drobinski et al. (2005)). In the Tramontane flow, a hydraulic jump has been observed very close to the coast (Drobinski et al. (2001)). At the location of a hydraulic jump, the wind speed drops rapidly. This effect is not represented neither in the regional climate simulations nor in ERA-Interim. Nevertheless, most simulations perform better than ERA-Interim in the valley areas.

A.6.3. Effects over the Mediterranean Sea

The RMSE of wind speed over the Mediterranean Sea could be reduced in most simulations by choosing only days with correctly predicted M/T pressure patterns. Therefore, the spatial patterns over the Mediterranean Sea can be evaluated in greater detail when regarding only those days.

When the wind enters the region over the Mediterranean Sea, it shows a negative bias in all simulations. Accadia et al. (2007) and Ruti et al. (2008) found QuikSCAT to show higher wind speeds than observations from two buoys in the Gulf of Lion area. Therefore, part of the simulation bias could be explained by an overestimation of wind speed by QuikSCAT. Even simulations with a high overestimation of land surface wind speed do not overestimate surface wind speed over the Mediterranean Sea. Indeed, the sea surface wind speed is underestimated in those models as well. This hints that the simulations need several grid points to adjust to the situation above the sea surface. The effects at the coast are not yet understood. Since QuikSCAT observations are not available at the coast, but only at a distance of 25–50 km, the wind speed change at the coast cannot be evaluated.

From the Charnock formula one might expect that smaller α values lead to higher wind speeds, but the wind speed bias does not only depend on the roughness length parameterization used. In the area of interest in this study, the 0.44° simulations show no clear dependence of the bias on the α value. GUF-CCLM (α=0.0123) e.g. shows a by –0.22 m/s stronger bias than IPSL-WRF (α=0.0.185), while the bias of CNRM-ALADIN (α=0.021) is even more negative than that of GUF-CCLM by -0.25 m/s. Edelmann (2015) tested the influence of roughness length parameterization on wind speed in GUF-CCLM at 0.088° grid spacing. The bias of wind speed in the Gulf of Lion area was found to change by up to 0.5 m/s for different versions of the Charnock formula, which is smaller than the overall bias over the Mediterranean Sea.

In all models, the main flow area of Mistral and Tramontane seems to be too narrow close to the coast. Errors are higher close to the Gulf of Lion coast than in the main flow area. When taking into account that QuikSCAT shows higher wind speeds than the buoy in the Gulf of Lion, these spatial patterns are robust (tested with a wind speed dependent QuikSCAT bias, not shown). Close to the eastern coast of the Gulf of Lion, intensified cooling has been observed during Mistral events and in coupled simulations (Small et al. (2012); Schaeffer et al. (2011)). Renault et al. (2012) studied a Tramontane event in coupled simulations and found a decreasing sea surface temperature in the western part of the Gulf of Lion. Correct sea surface temperatures are important forcing data for the climate simulations. On one hand, sea surface temperature influences the momentum mixing of the atmospheric boundary layer, and therefore the wind speed. On the other hand, correct wind speed simulations are required to simulate the sea surface cooling during M/T events in coupled simulations (Chelton et al. (2004); Lebeaupin Brossier and Drobinski (2009)).

During M/T days, all simulations show a positive wind direction bias close to the coast and a negative slope in the fetch-dependent linear fit. This indicates wind that is rotated too far clockwise close to the coast, which turns in a counterclockwise direction while traveling over the Mediterranean Sea. About 220 km away from the coast, all models reach a wind direction RMSE close to the accuracy of the reference QuikSCAT product. Since the wind speed above the Mediterranean Sea is underestimated compared to QuikSCAT, the wind direction that is rotated too far clockwise is unlikely to be caused by Coriolis effects alone. The orographic features of the region (the Alps, Massif Central, and Pyrenees) also are important, and influence the wind direction. Giles (1977) stated that the Coanda effect causes the Mistral to stay attached to the Alps rather than blow straight over the Mediterranean Sea. This also changes the wind direction, causing the direction of gusts in the time series in Table A.1 to change from north in the valley and plain stations to west and northwest at the easterly coastal stations Toulon and Cap Cepet. The erroneous simulation of the Mistral and Tramontane's attachment to the mountain ranges might also cause the too narrow main flow area in the Gulf of Lion.

A.6.4. Influence of Grid Spacing

The higher resolution runs perform better in simulating small scale phenomena, such as the orographic features in mountainous areas. Thus, higher resolution simulations reach higher wind speeds in orography-induced winds (Mass et al. (2002); Louka et al. (2008)). This effect is present in the CNRM-ALADIN and GUF-CCLM simulations, where higher resolution simulations show higher wind speeds than the simulations with coarser resolution. Simulations with smaller grid spacing also show higher wind speeds over the Mediterranean Sea, and therefore smaller biases. They also adjust faster to the higher wind speeds and show less pronounced errors at the borders of the main flow.

A.7. Summary and Conclusion

The goal of this study was to evaluate five regional climate models (ALADIN, WRF, PROMES, CCLM, and LMDZ) in terms of the Mistral and Tramontane. The focus was on the effects when a Mistral and/or Tramontane event is simulated. Therefore, days on which simulated sea level pressure fields show a Mistral and Tramontane-permitting pattern were identified. After excluding errors due to the large-scale pressure fields, further error sources could be identified.

The results show that all five regional climate models used in this survey are able to correctly simulate Mistral and Tramontane situations 74–82 % of the time. Most models show smaller wind speed biases than ERA-Interim in the Mistral and Tramontane areas of southern France. However, the modeling of effects in the valleys is still erroneous. Wind speed changes in areas with small-scale orographic features are difficult to reproduce in simulations. During Mistral and Tramontane events, most simulations underestimate wind speed over the Mediterranean Sea, but show smaller biases than ERA-Interim. The bias is strongest at the borders of the main flow. All simulations of this study show a clockwise wind direction bias during Mistral and Tramontane events. Higher resolution simulations (0.088–0.22° grid spacing) show smaller biases than their 0.44° counterparts.

This leads to the conclusion that regional climate models are mostly able to simulate Mistral and Tramontane events at the correct dates, and with smaller biases than ERA-Interim. When the large scale is represented well in the driving model, regional climate models can simulate Mistral and Tramontane. Higher resolution simulations provide better results in the valleys, but the major improvement obtained by increasing the resolution occurs over the sea. This effect is not yet understood. To correct the wind speed underestimation over the sea, especially at the borders of the main flow, the reciprocal interference of the sea surface temperature and wind speed and the influence of the Coanda effect should be investigated in further studies.

Acknowledgements

This work is part of the Med-CORDEX initiative (www.medcordex.eu) supported by the HyMeX programme (www.hymex.org). This work is a contribution to the HyMeX program (HYdrological cycle in The Mediterranean EXperiment) through INSU-MISTRALS support and the MEDCORDEX program (COordinated Regional climate Downscaling EXperiment - Mediterranean region).

The simulations used in this work were downloaded from the Med-CORDEX database. Gust time series were provided by Valérie Jacq, Météo-France.

GUF simulations were performed at DKRZ and LOEWE-CSC. GUF acknowledges support from Senckenberg BiK-F.

This research has received funding from the French National Research Agency (ANR) projects REMEMBER (contract ANR-12-SENV-001). It was supported by the IPSL group for regional climate and environmental studies, with granted access to the HPC ressources of GENCI/IDRIS (under allocation i2011010227).

UCLM contribution has been partially funded by the Spanish Government and the European Regional Development Fund, through grants CGL2007-66440-C04-02, CGL 2010-18013 and CGL2013-47261-R.

B. Paper 2: Influence of Sea Surface Roughness Length Parameterization on Mistral and Tramontane Simulations

published as

Anika Obermann, Benedikt Edelmann, and Bodo Ahrens, *Influence of sea surface roughness length parameterization on mistral and tramontane simulations*, Advances in Science and Research (2016), 13, 107–112.

Abstract

The Mistral and Tramontane are mesoscale winds in southern France and above the Western Mediterranean Sea. They are phenomena well suited for studying channeling effects as well as atmosphere–land/ocean processes. This sensitivity study deals with the influence of the sea surface roughness length parameterizations on simulated Mistral and Tramontane wind speed and wind direction. Several simulations with the regional climate model COSMO-CLM were performed for the year 2005 with varying values for the Charnock parameter α. Above the western Mediterranean area, the simulated wind speed and wind direction pattern on Mistral days changes depending on the parameterization used. Higher values of α lead to lower simulated wind speeds. In areas, where the simulated wind speed does not change much, a counterclockwise rotation of the simulated wind direction is observed.

B.1. Introduction

The Mistral and Tramontane are winds in southern France, which are channeled by the Rhône and Aude valleys before blowing over the Mediterranean Sea. Since this winds are caused by similar synoptic situations, they often occur at the same time (Georgelin et al. (1994); Guenard et al. (2005)). They play a crucial role for deep water formation in the Gulf of Lion and for the understanding of the Mediterranean Sea circulation (Schott et al. (1996); Béranger et al. (2010)). On Mistral and Tramontane days, simulations with the regional climate model COSMO-CLM (CCLM) with 0.088° grid spacing were found to be able to simulate Mistral and Tramontane wind patterns slightly overestimating 10-m wind speed compared to satellite and buoy observations (Obermann et al. (2016a)).

This sensitivity study investigates the influence of the sea surface roughness length parameterization on the patterns of Mistral and Tramontane wind speeds and wind directions above the Mediterranean Sea in CCLM simulations. The aim of this study is not to find a better parameterization of surface roughness, but a discussion of the sensititvity of wind patterns of an atmospheric model on its parameterization. A complete description of the ocean-atmosphere interaction and, therefore, the sea surface roughness, also should account for ocean currents, waves, and interaction between these phenomena (Carniel et al. (2016); Ricchi et al. (2016)).

Three atmosphere only simulation runs with different parameterizations were performed for the year 2005 in which Mistral occurred at 88 days. 81 of which in coincidence with Tramontane (Edelmann (2015)). The Mistral and Tramontane days in 2005 were identified using 13 observation stations in Southern France which provided gust information along the dominant Mistral and Tramontane directions. An explanation of the full algorithm to identify Mistral and Tramontane days can be found in Obermann et al. (2016a).

B.2. Regional Climate Simulations

The CCLM model (Rockel et al. (2008); Kothe et al. (2014)) is the climate version of the nonhydrostatic atmospheric COSMO model, which is used by the German Weather Service for operational weather forecasts. It consists of the primitive thermo-hydrodynamical equations for a fully compressible flow in moist atmosphere formulated in rotated geographical coordinates and generalized terrain following height coordinates. The simulations of this study were performed by Goethe Universität Frankfurt (GUF) using the model version CCLM 5-0-2 with a turbulent kinetic energy (TKE) transfer scheme for surface fluxes and the soil model TERRA. A two time-level second-order Runge-Kutta scheme was used. Spectral nudging, condensation, convection and grid scale precipitation were enabled (Edelmann (2015)).

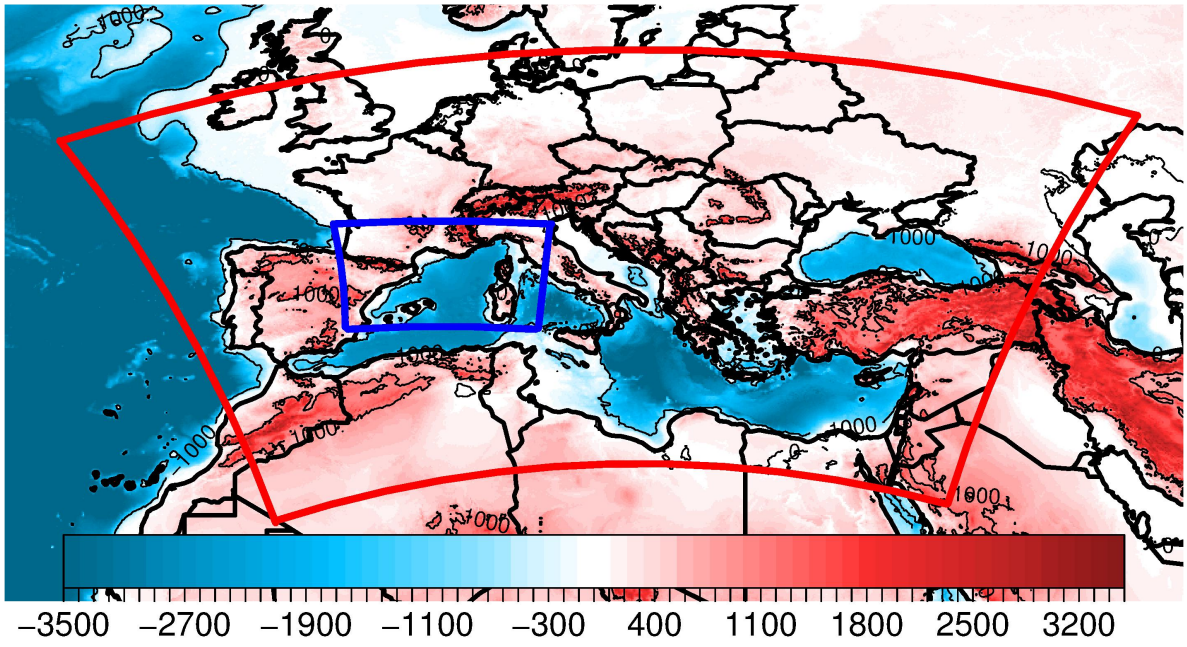

Figure B.1.: ETOPO1 (Amante and Eakins (2009)) orography and bathymetry data interpolated onto a 0.088° grid [m]. MedCORDEX domain in red, nested domain in blue.

B.2.1. Nesting Strategy

The simulations cover a domain of 1140 × 800 km^2 encompassing Southern France and a large part of the western Mediterranean Sea (area marked in blue in fig. B.1). The

simulations are nested into a CCLM simulation (model version CCLM 4-8-18) on the larger MedCORDEX domain which covers the Mediterranean Sea, the Black Sea, and the surrounding land areas (Ruti et al. (2016), area marked in blue in fig. B.1). The simulation on the outer domain was initialized at 01.01.1989, while the simulations on the inner domain cover 1 year, starting from 01.01.2005. Horizontal grid spacing for both domains is 0.088° with 40 vertical levels and a time step of 30 seconds. One way nesting with three boundary lines (i.e. about 30 km) is used. The boundary data are updated every three hours and interim time steps are linearly interpolated (Edelmann (2015)).

B.2.2. Forcing Data

The forcing data for the simulation on the MedCORDEX domain comes from ERA-Interim (Dee et al. (2011)). The information on sea surface temperature (SST) is provided as daily means and linearily interpolated to the CCLM grid.

B.2.3. Variation of Roughness Length

The roughness length z_0 depends on the properties of ocean waves and, therefore, on wind speeds over the sea surface. A classical parameterization of sea surface roughness was introduced by Charnock (1955):

$$z_0 = \frac{\alpha}{g} \times u_*^2 \tag{B.1}$$

The parameterization of sea surface roughness varies between regional climate models. For example, the Weather Research and Forecasting (WRF) model (Colin et al. (2010)) uses α=0.0185 and adds a constant of 1.59×10^{-5} m to avoid zero roughness length. Alternative versions of the Charnock formula from five regional climate models have been tested in CCLM. A detailed discussion of these parameterizations and comparison to observational data can be found in Edelmann (2015). In this study, the focus is on the variation of the CCLM parameterization of the Charnock formula. In CCLM (Doms et al. (2011)), the Charnock formula is implemented as

$$z_0 = \frac{\alpha}{g} \times \max\left(u_*^2, w_*^2\right) \tag{B.2}$$

Here, α denotes the Charnock parameter, g the gravity constant, u_* the friction velocity, and w_* the free convection scaling velocity. In the standard configuration, CCLM uses a value of α=0.0123. In this study, two larger values of the Charnock parameter (α=0.025 and α=0.05) have been tested because of the aforementioned overestimation

of wind speed in CCLM 0.088° simulations. Even though large values of α do not have a physical background, they give the possibility to test the sensitivity of wind patterns on α. Figure B.2 shows the roughness length as function of u_* for the three values of α tested in this study. All other parameters and the forcing data are the same for all three simulation runs.

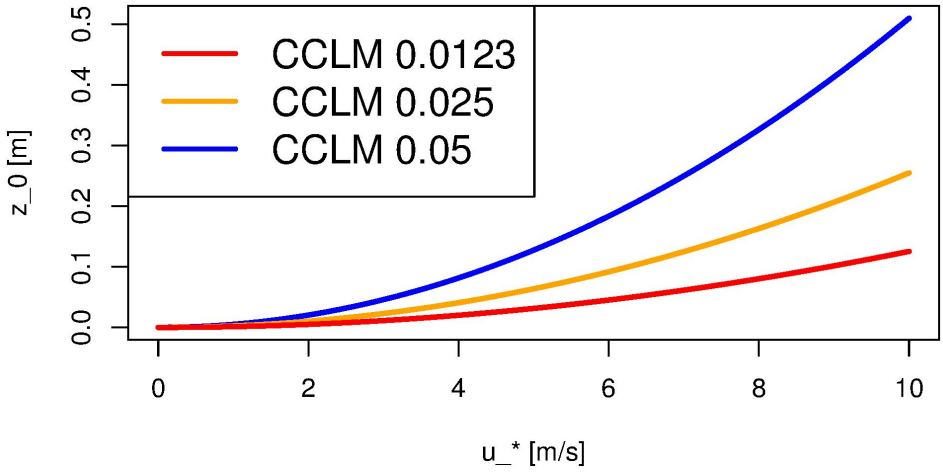

Figure B.2.: Roughness length as function of u_* for three values of Charnock parameter α.

B.3. Results

B.3.1. Reference Simulation

Figure B.3a shows the mean sea level pressure during the Mistral days in 2005 from the reference simulation (α=0.0123). The situation is characterized by a pressure low visible close to Corsica in the right part of the figure.

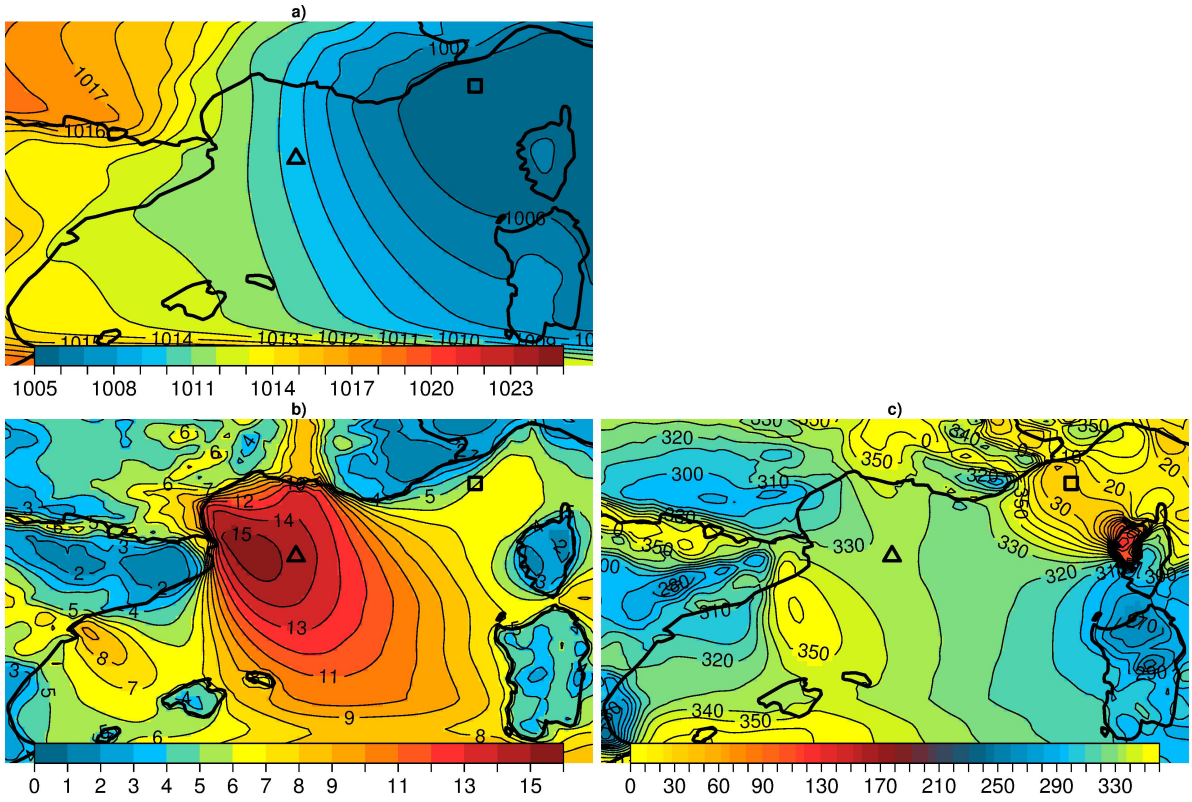

Figure B.3.: Mean sea level pressure (hPa) (a), mean 10-m wind speed (m/s) (b) and mean 10-m wind direction (°) (c) during Mistral events in the reference simulation (α=0.0123) in the Gulf of Lion area. Locations of Lion (triangle) and Azur (square) buoys.

Figure B.3b shows the mean 10-m wind speeds during the same days. The highest wind speeds occur over the Mediterranean Sea in the Gulf of Lions. The effect of channeling (i.e. the acceleration of wind in valleys) is visible in the Rhône and Aude valleys. Two more local wind phenomena are visible during Mistral days: In the Ebro valley south of the Pyrennes, the local wind Cierzo causes wind speeds up to 9 m/s

during Mistral days. The italian Tramontane between Alps and Apennines reaches up to 5 m/s. During Mistral and Tramontane events, the mean wind direction is north to northwest (fig. B.3c). In the Rhône valley, Mistral comes mainly from north, while the dominant Tramontane direction in the Aude valley is west-northwest.

B.3.2. Changes in Wind Speed and Direction along the Variation of α

Figure B.4 shows the bias of the simulation runs with α=0.025 and α=0.05 compared to the reference run (α=0.0123). A decrease in wind speeds is observed for increasing α (figs. B.4a and B.4c) in large parts of the modeling domain. The strongest decrease in wind speed for increasing α occurs in areas with high absolute wind speeds in the reference run (fig. B.3b).

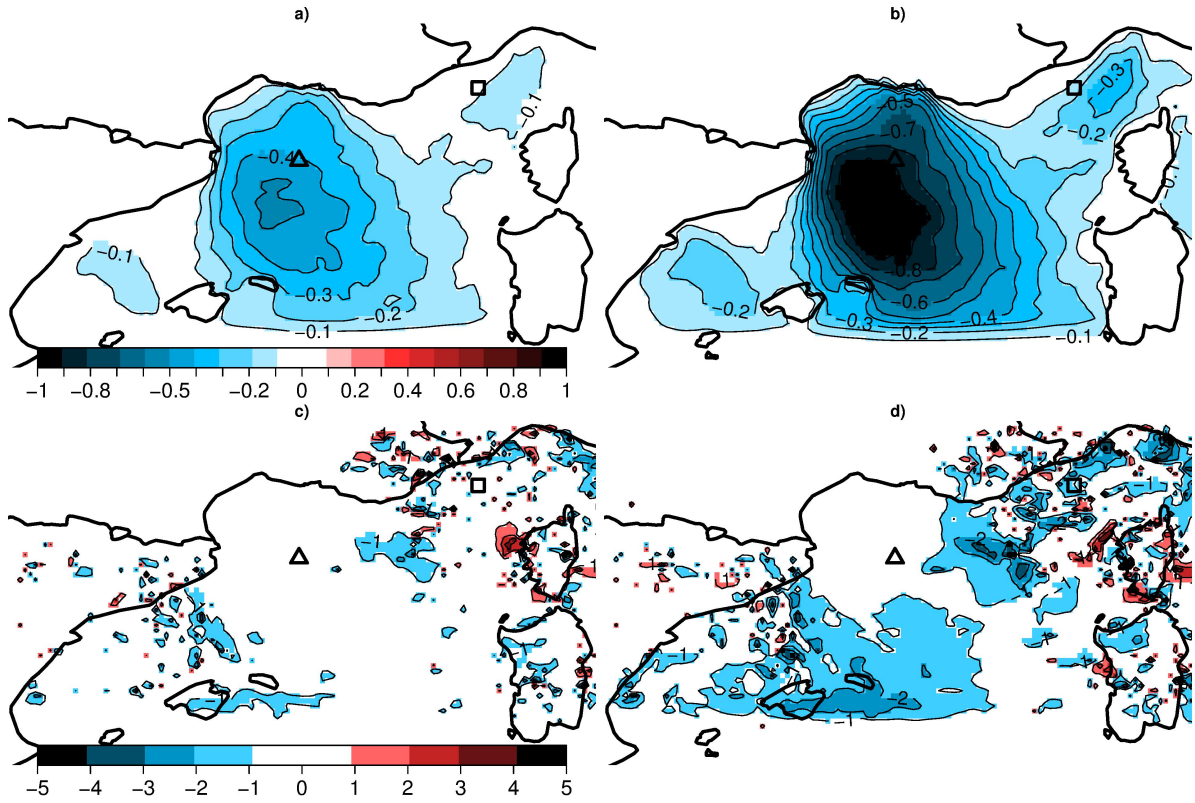

Figure B.4.: 10-m wind speed bias (m/s) (a and b) and 10-m wind direction bias (°) (c and d) for α=0.025 (a and c) and $\alpha = 0.05$ (b and d) with respect to reference (α=0.0123). Locations of Lion (triangle) and Azur (square) buoys.

With increasing α, the wind direction changes to a more counterclockwise rotated direction south of the Balearic Islands, between the Alps and Corsica, as well as from Corsica to the northern Apennines (figs. B.4c and B.4d)). In the residual areas around Corsica and at the coast close to Alps and Pyrenees, the wind is rotated clockwise. The variation of α exerts only a weak influence upon the sea level pressure field: On one hand the sea level pressures undergo only slight changes in general. On the other hand the position of the minimum sea level pressure within the domain does not move (not shown).

B.3.3. Buoy Observations

In the area of interest, two stationary buoys measure wind speed and wind direction (and further parameters) several times a day. The Lion buoy is located in the Gulf of Lion (42.1°N, 4.7°E), the Azur buoy is located close to the French-Italian border (43.4°N, 7.8°E). The buoy locations are marked in figs. B.3 and B.4. Figure B.5 shows wind speed density plots for both buoy locations. The wind speed is overestimated by all three simulations, with the reference (α=0.0123) having the largest bias.

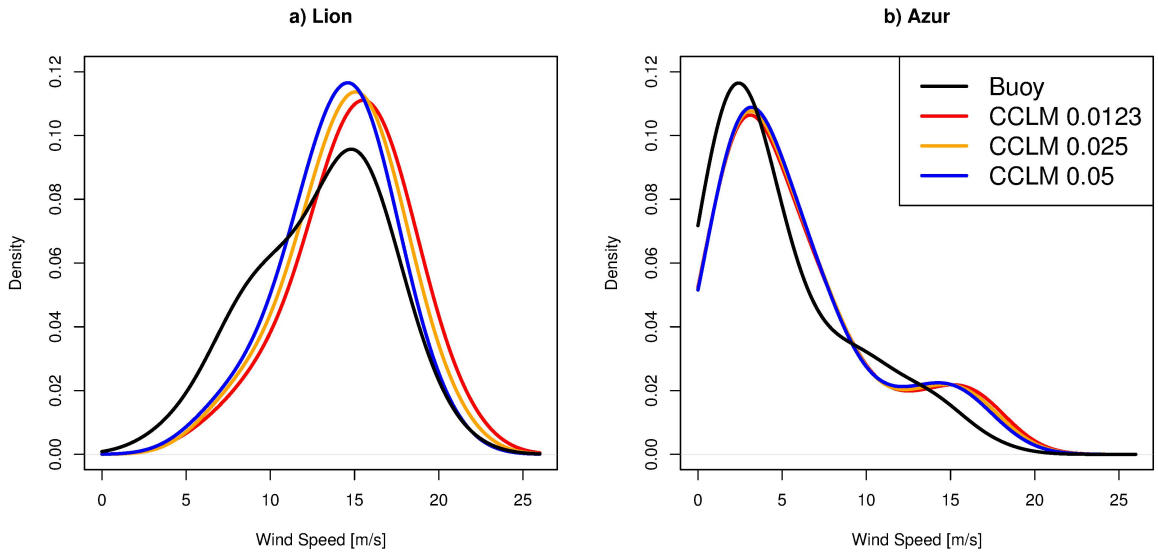

Figure B.5.: 10-m wind speed density distribution at Gulf of Lion buoy location (a) and Azur buoy location (b).

As can be seen from figure B.3c, the wind comes from a north-westerly direction at the Lion buoy location during Mistral days. The simulations show a small clockwise

rotated bias at this location. The main wind direction for the Azur buoy location is north-easterly. Here, the simulations show a counter-clockwise rotated bias. As can be seen from figure B.4c) and d), the wind direction differences between the three simulations at both buoy locations are small.

B.3.4. Interconnection of Wind Speed and Wind Direction Change

The Mistral events in 2005 are divided in two groups, depending on the observed wind speed at the Lion buoy. 32 days showed daily mean 10-m winds below 12 m/s, 52 showed wind speeds above 12 m/s. For the remaining 4 days no observations were available. For both the α=0.025 and the α=0.05 run, the wind speed decreased stronger on days with high wind speeds in the reference run. On days with lower wind speeds, the change in direction is stronger than for days with high wind speeds (not shown).

B.3.5. Influence of Sea Surface Temperature

The daily mean sea surface temperatur (SST) in the area 3–8° East and 38.5–43.5° North is used to divide the Mistral days in days with high SSTs (above 20° C) and days with low SSTs (below 14° C). 29 Mistral days of 2005 are in each of the groups. When calculating the biases as shown in fig. B.4, the influence of SST on wind speed and direction changes can be derived. The wind speed change compared to the reference is stronger during cold Mistral events, while the wind direction changes are more pronounced during warm events. The relative change in wind speed is of the same magnitude during cold and warm events, due to the stronger wind speeds during cold events (not shown).

B.4. Discussion

The 10-m wind speed decreases in large parts of the modeling domain for increasing α as expected from the u_*^2-dependence of eq. B.2. This result is in agreement with the findings of Thévenot et al. (2015), who showed that an increase in wave heigth (and a resulting increase in z_0) leads to lower wind speeds.

The largest differences are found for the Gulf of Lion, where the highest wind speeds are observed in the reference simulation. Another effect occurs in wind direction: Here, the bias is the largest in the area between the Alps and Corsica (that is, in the north-eastern part of the investigation domain) where only minor wind speed changes are observed. From the wind speed dependence of the Coriolis force one would expect that slower winds (as they are observed for higher values of α) come from a more counterclockwise rotated direction. Consequently, this effect should be stronger where the wind speed change is larger, but this is not present in the simulations.

Indeed, the change of wind speed and wind direction do not occur at the same time and location. The patterns found in this sensitivity study could be due to several phenomena. The counterclockwise rotation at the borders of the main flow could be due to the flow becoming more agestrophic with decreasing wind speed. Coriolis force decreases with decreasing wind speeds, and the counteracting pressure gradient force could cause the rotation. Giles (1977) discussed the Coanda effect resulting in the Mistral staying attached to the Alps. This counteracts the clockwise rotation of Mistral and Tramontane due to the Coriolis force. The increased α values could potentially result in a broadened Mistral and Tramontane flow, which would extend further to the east. A consequence of which would be a smaller bias in wind speed and a counter-clockwise rotated wind between Alps and Corsica. The situation east of Corsica could be similar in the case of the Italian Tramontane.

On days with higher SSTs, the wind direction changes are stronger than on days with low SSTs, while the wind speed changes are larger on days with low SSTs. An increased α parameter influences the winter and spring Mistral days (i.e., days with low SSTs) more in terms of wind speed, while the influence on wind direction is the strongest during summer and autumn (i.e. days with high SSTs).

B.5. Conclusions

Three values for the Charnock parameter α have been tested within the regional climate model COSMO-CLM. In the Western Mediterranean area, the wind pattern on Mistral days changes depending on the parameterization used. While the whole sea level pressure pattern does not change much, higher values of α lead to lower wind speeds in the main flow. The overestimation of wind speeds found in the reference simulation was reduced. A counterclockwise rotation of the wind on the left hand border of the flow is observed for higher valutes of α. This could be due to a change in the balance between the wind speed dependent Coriolis force and pressure gradient force as well as corner effects as the so called Coanda effect, which causes a flow to stay close to nearby mountain ranges. Further studies are needed to test these assumptions and to study the sensitivity to roughness length changes due to other phenomena (e.g., ocean currents and waves).

Author Contribution

Ben Edelmann carried out the experimental simulations. Anika Obermann prepared the figures and the manuscript with contributions from all co-authors.

Acknowledgements

This work is part of the Med-CORDEX initiative (www.medcordex.eu) supported by the HyMeX programme (www.hymex.org). Gust time series were provided by Valérie Jacq, Météo-France. Buoy data were provided by Marie-Noelle Bouin and Guy Caniaux, Météo-France. Simulations were performed at DKRZ and LOEWE-CSC. We acknowledge support from the German Federal Ministry of Education and Research (BMBF) under grant MiKliP II (FKZ 01LP1518C). B. Ahrens acknowledges support from Senckenberg BiK-F. We thank two anonymous reviewers.

C. Paper 3: Mistral and Tramontane Simulations with changing Resolution of Orography

submitted as

Anika Obermann-Hellhund and Bodo Ahrens, *Mistral and Tramontane Simulations with changing Resolution of Orography*, Atmospheric Science Letters (2017)

Abstract

Mistral and Tramontane are mesoscale winds in southern France. Both winds emerge in valleys and cause deep water formation in the Mediterranean Sea, which makes them interesting phenomena for studying several orographic effects and relevant for Earth system models. However, climate simulations are performed on a finite numerical grid with a coarse-gridded orography and processes on subgrid scales are parameterized. This study surveys the effect of orographic grid spacing (2.6–45 km) on Mistral and Tramontane by performing idealized simulations with a 1.3 km horizontal numerical grid. Reduction of the orographic detail leads to a wind pattern change and a wind speed reduction. If orographic features on smaller scales are parameterized, the effects of the smoothing are weaker, but a systematic decrease in channeling and wind speed still persists.

Keywords Mistral, Tramontane, COSMO-CLM, idealized simulations, orographic resolution

C.1. Introduction

Mistral and Tramontane are Mediterranean mesoscale winds. Mistral passes through the Rhône valley between the Alps and Massif Central from north to south, while Tramontane emerges in the Aude valley between Pyrenees and Massif Central. In the constricting valleys, both cold and dry winds accelerate before they reach the Mediterranean Sea at the Gulf of Lion. Since similar synoptic situations cause Mistral and Tramontane, they often occur simultaneously (Georgelin et al. (1994); Guenard et al. (2005)). Both winds impact the hydrological cycle of the Mediterranean Sea by causing deep-water formation (Marshall and Schott (1999); Somot et al. (2016)). They are connected to vortices, which are observed in the Gulf of Lion after episodes of high wind speeds (Allou et al. (2010)). Many case studies dealt with Mistral and Tramontane events (e.g., Drobinski et al. (2005); Berthou et al. (2016)) and involved processes like the Coanda effect (Giles (1977)) and the flow through a mountain gap (Gaberšek and Durran (2004, 2006)). Drobinski et al. (2017) surveyed the structure of Mistral using a Lagrangian analysis.

Regional climate models (RCMs) usually are run on grid spacings of 10 to 50 km, e.g. in the coordinated regional downscaling experiment CORDEX (Giorgi and Gutowski (2015)) and its Mediterranean branch Med-CORDEX (Ruti et al. (2016)). RCMs with these grid spacings can reproduce Mistral and Tramontane patterns in general but underestimate the wind speed in some areas of the flow. Furthermore, high-resolution models show smaller biases than the coarser simulations, but a similar pattern in the biases (Obermann et al. (2016a)). Changes in sea surface roughness parameterization showed an impact on wind speed and wind direction during Mistral events (Obermann et al. (2016b)). Increasing the model resolution improves the representation of wind speeds in the Mediterranean region (Herrmann et al. (2011); Ruti et al. (2008)) and enhances the quality of coupled simulations (Akhtar et al. (2017)).

Experiments with realistic and smoothed orography (Figure C.1) are performed in an idealized modeling setup using COSMO-CLM (Rockel et al. (2008); Blahak (2015)). Since COSMO-CLM performs well in real Mistral and Tramontane cases (Obermann et al. (2016a)), the focus is on the processes which contribute to the quality of the simulation. Besides Coriolis force and surface fluxes, this study isolates the impact of better orography representation in Mistral and Tramontane simulations. The orography is smoothed and the features smaller than the orography grid spacing (sub-orography scale) are parameterized using the subgrid-scale orography scheme (SSO) implemented in COSMO-CLM. The primary focus is on the change in maximum wind speed downstream of the mountain gap / the valley.

C.2. Simulation Setup

The simulation domain covers a $10° \times 10°$ area with 601×601 grid cells and 40 vertical levels using the idealized setup of the non-hydrostatic climate model COSMO5-CLM7 (Rockel et al. (2008); Blahak (2015)). Open boundary conditions (wave-absorbing conditions) were used with a constant 5 m/s inflow at the northern boundary with a constant temperature gradient of -6.5 K/km below 12 km and a temperature of 210.15 K above.

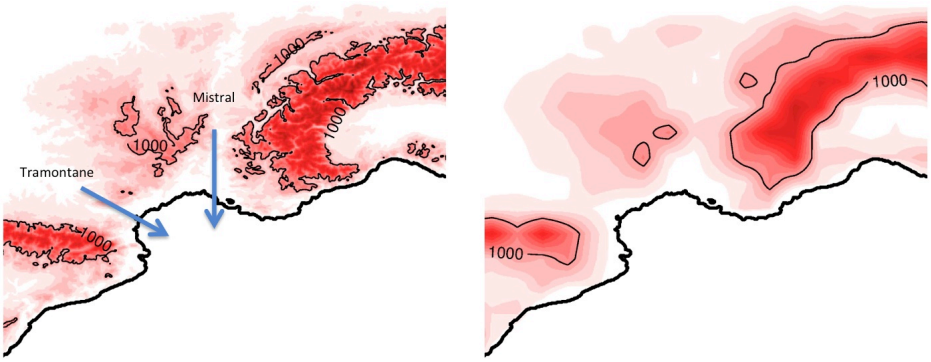

Figure C.1.: Orography of the simulations with a) ETOPO1 resolution ($\Delta x \approx 1.3$ km) and b) smoothed ($\Delta x \approx 44$ km). Coastlines (thick lines) and 1000-m isolines (thin lines) are indicated.

The numerical grid spacing was ≈1.3 km on a non-rotated longitude-latitude grid, which corresponds to the native grid spacing of the orography dataset ETOPO1 at about 45°N (Amante and Eakins (2009)). The altitude of the Mediterranean Islands (the Balearic Islands, Sardinia, and Corsica) was set to 0 m and their surface was treated as water surface. The orography at the northern border was linearly interpolated to 0 m, resulting in the orography shown in Figure C.1a. In the experiments, the orography was smoothed by factors 2–34 using linear interpolation, while keeping the numerical grid spacing constant at one arc minute. Simulations with an n-times smoothed orography were named oro$n$ (Table C.1).

Four different simulation setups were used, differing in whether or not they take into account Coriolis force, surface fluxes, and orography information on smaller scales than the orography grid (parameterized using SSO). Table C.2 gives an overview of the simulations.

Table C.1.: Orography representation scale and corresponding smoothing factor n.

n	Degrees	km
2	0.03	2.6
10	0.17	13.2
18	0.30	23.7
26	0.43	34.2
34	0.57	44.8

Table C.2.: Names of simulations and included effects.

Name	Coriolis	Surface Fluxes	SSO
oron_{none}	no	no	no
oron_{cori}	yes	no	no
oron_{flux}	yes	yes	no
oron_{SSO}	yes	yes	yes

Mistral and Tramontane are influenced by Coriolis force because it extends over 100s of km. The COSMO-CLM idealized setup applies the Coriolis force in the f-plane approximation with f=2sin(45°) (Blahak (2015)). Furthermore, the idealized setup does not have a geostrophic pressure initialization. The wind field needs some time to adjust to an equilibrium flow (Blahak (2015)). During the adjustment phase, some boundary effects might occur. Therefore, the simulations run for 14 days and the evaluation applies to days 11 to 14. All setups except oron_{none} include the Coriolis force.

Surface transfer coefficients for momentum and heat can be set to zero in idealized simulations. Zero transfer coefficients lead to the so-called free-slip boundary conditions and, therefore, no momentum transfer into the ground. Surface fluxes were set to zero in oron_{none} and oron_{cori} simulations. oron_{flux} and oron_{SSO} setups include surface fluxes with a constant roughness length of 0.01 m over the land area. Over sea surface, the Charnock formula (Charnock (1955)) parameterizes the surface roughness length depending on the local wind speed with a constant Charnock parameter of α=0.0123 (Doms et al. (2011)).

To account for the orography on smaller scales and counteract effects of smoothing the orography, the possibility to use an SSO parameterization (Lott and Miller (1997)) is implemented in COSMO-CLM (Schulz (2008)). In this study, the information on smaller scales than the orography (which is smoothed by the factors given in Table C.1) is used as parameters of the SSO, not the information on smaller scales than the numerical grid (which is ≈1.3 km for all simulations). The SSO parameterization

increases the surface fluxes and reduces the wind speeds near the surface. It is based on variance, anisotropy, angle between wind and main topography axis, and mean slope, which are calculated for each grid cell of the smoothed orography. SSO is included in the oron_{SSO} setup.

C.3. Results and Discussion

C.3.1. Source Processes

Figure C.2 shows the wind speed, wind direction, and sea level pressure for the simulation setups with orography information smoothed by a factor of 2. The complexity of the simulation is increasing from left to right.

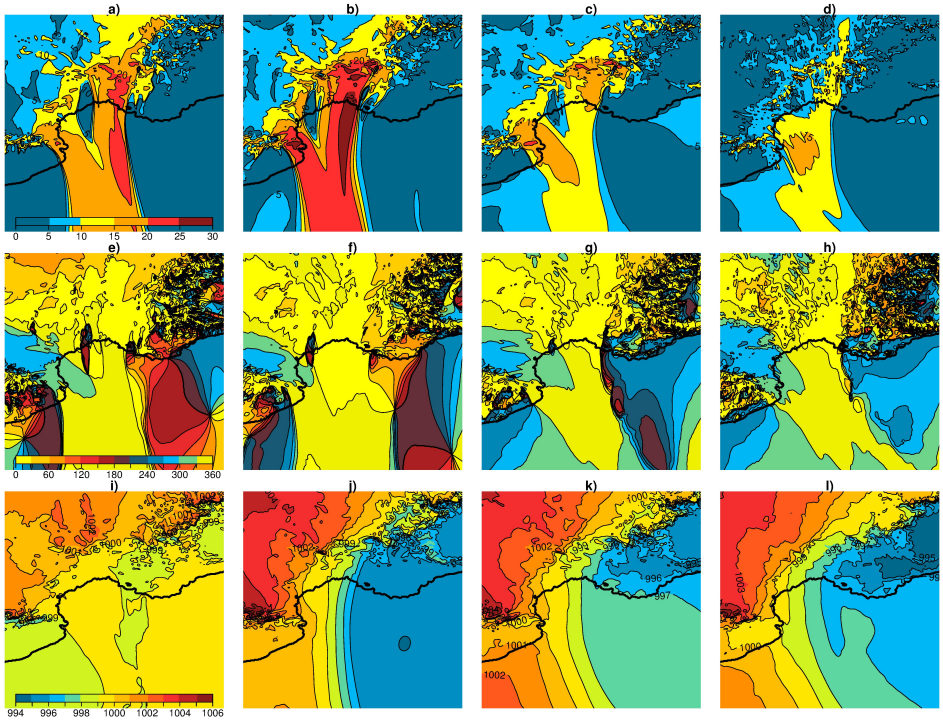

Figure C.2.: Mean wind speed (m/s, upper row) and mean wind direction (°, middle row) at lowest model level and mean sea level pressure (hPa, lower row) of day 11-14 for simulations oro2$_{none}$ (a, e, i), oro2$_{cori}$ (b, f, j), oro2$_{flux}$ (c, g, k), and oro2$_{SSO}$ (d, h, l).

In the simplest setup oro2$_{none}$, Mistral and Tramontane accelerate in the valleys (Figure C.2a) and show a northerly to northwesterly wind direction (Figure C.2e). Due to the leeward effects of mountain ranges, the sea level pressure is lower at the sides of the main flow than on its center (Figure C.2i). When Coriolis force is added, the maximum wind speeds increase by about 5 m/s (oro2$_{cori}$, Figure C.2b), and the wind comes from a more northerly direction (Figure C.2f). At the same time, an east-west pressure gradient develops due to the Coriolis force and the counteracting pressure

gradient force. When surface momentum transfer and, therefore, surface friction, is introduced the maximum wind speed decreases again by about 10 m/s (Figure C.2 c) and both the wind direction and the pressure gradient rotate counterclockwise (Figure C.2g,k). Adding SSO to the calculation of surface friction in oro2$_{SSO}$ leads to reduced wind speeds in most areas (Figure C.2d) and changes in wind direction and sea level pressure (Figure C.2h,l). Experiment oro2$_{SSO}$ also shows a better agreement with wind patterns during Mistral and Tramontane events from satellite data and ERA-Interim (Obermann et al. (2016a)) as well as balloon observations Drobinski et al. (2017)) than the other setups.

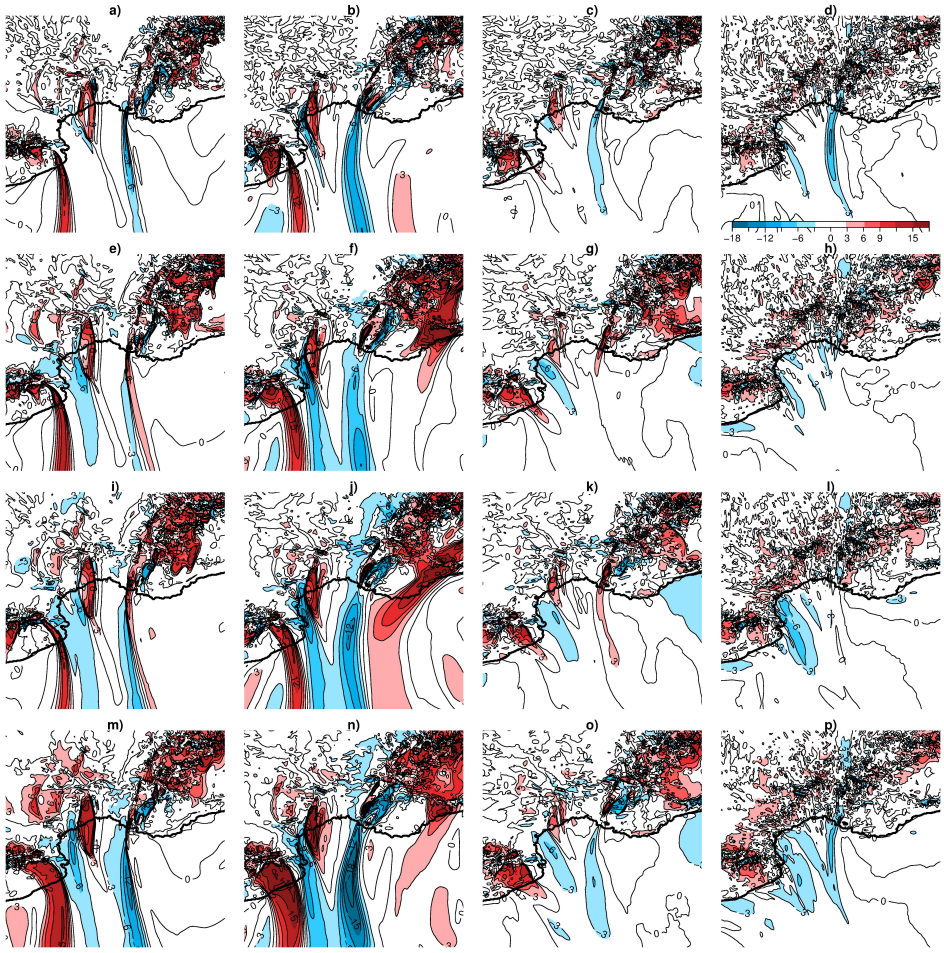

Figure C.3.: Change in wind speed (m/s) at lowest model level when orography is smoothed from $n = 2$ to $n = 10$ (upper row), $n = 18$ (second row), $n = 26$ (third row), and $n = 34$ (lower row) for simulations oron_{none} (left column), oron_{cori} (second column), oron_{flux} (third column), and oron_{SSO} (right column). Table C.1 shows the corresponding grid spacing in km.

C.3.2. Orographic Detail

Figure C.3 shows the wind speed change for smoothed orography simulations in comparison to the oro2 simulation of the same setup. The area east of Mistral shows smaller wind speeds than the reference, while they are higher west of Tramontane in oron_{none}, and oron_{cori} simulations, hinting to a westward shift of the wind systems. oron_{flux} shows a similar, but weaker shift, while oron_{SSO} shows decreasing wind speeds at both sides of the flow. Including SSO, therefore, could reduce this westward shift. In the area where both winds merge, the changes are smaller.

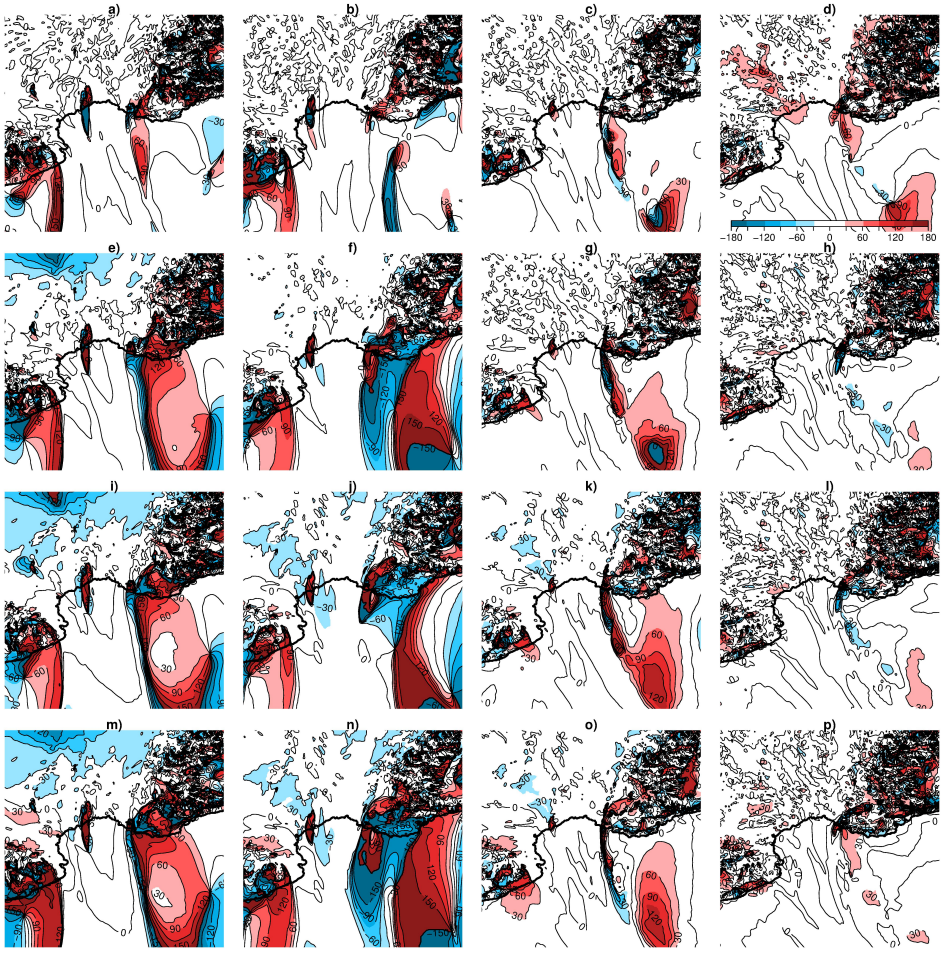

Figure C.4.: As Figure C.3 but for wind direction (°) at lowest model level. Positive (negative) values indicate a clockwise (counter-clockwise) shift.

Figure C.4 shows the change in wind direction. Strong changes in wind speed mainly occur at the borders of the flow, while the main flow wind direction does not change. The largest changes occur in the oron_{none} and oron_{cori} simulations. Including surface

fluxes in simulations reduces this dependence on orography smoothing. In combination with SSO, the change in wind direction is further reduced.

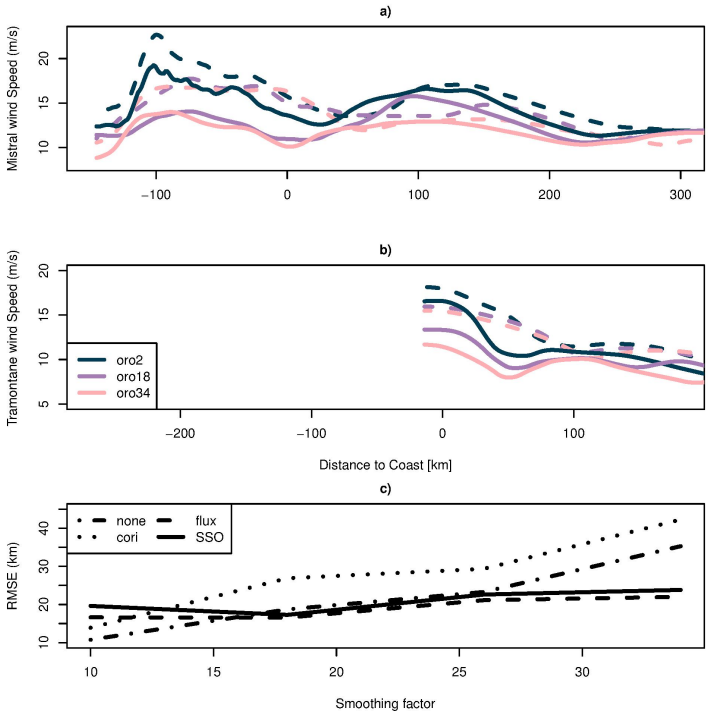

Figure C.5.: Maximum wind speed (m/s) at lowest model level for simulations oron_{SSO} (full lines) and oron_{flux} (dashed) in Mistral (a) and Tramontane (b) area and RMSE of maximum wind speed location (c).

Figure C.5 a) and b) show the maximum wind speed as a function of the distance to the coastline for Mistral and Tramontane. The acceleration of Mistral in the Rhône Valley, about 100 km away from the coast, is visible even in the smoothed simulations. All simulations with smoothed orography show smaller average wind speeds than the corresponding oro2 simulations. The shape of the maximum wind speed is similar to the mean observed wind speed during Mistral and Tramontane events (Obermann et al. (2016a)) with a pronounced acceleration at the constriction of the Rhône Valley. It also resembles the wind speed during Mistral events observed by Drobinski et al. (2017) using balloons. They divided the Mistral flow in an injection zone (towards the center of the Genua cyclone), an ejection zone (outwards of the cyclone) and a zone of geostrophic deceleration.

Figure C.5 c) shows the RMSE of the position at which the maximum wind speed emerges depending on the smoothing factor with oro2 as the reference. The RMSE of oron_{none} and oron_{cori} simulations increases with increasing smoothing factor from about

10–15 km to about 35–45 km, while the RMSE of oron_{flux} and oron_{SSO} increases less strongly.

The pattern in oron_{none} could partially be explained by the change in valley cross section due to smoothing. The smaller the cross-section, the stronger the Venturi effect. Table C.3 gives the cross sections for the 5 smoothing factors assuming a Mistral flow which extends from the surface of the orography to 1300 m above sea level which corresponds to the simulated boundary layer height. The cross-section increases with increasing smoothing factor and, therefore, could explain the reduced wind speed in simulations with coarse orography.

With increasing smoothing factor, not only the valley cross section changes, but also its overall width. A broader (narrower) valley could cause a broader (narrower) Mistral flow and, as a result, a decrease (increase) in wind speed at the borders of the flow. Table C.3 gives the narrowest valley width in 1000 m elevation. As the cross-section, the width increases with orography smoothing, explaining the broadening of the Mistral flow. For high smoothing factors as in oro34, the Massif Central and the Alps are already substantially flattened and blend into the valley decreasing the valley cross section and width again (see also Figure C.1). Table C.3 also shows the mean Mistral wind speeds along the line of the maximum wind speed displayed in Figure C.5. The mean wind speed decreases with increasing valley width and cross section for all setups.

Table C.3.: Changes in Rhône valley properties and mean Mistral wind speeds with smoothed orography.

n	Cross section (km^2)	Valley width (km)	Mean Mistral wind speed (m/s)			
			oron_{none}	oron_{cori}	oron_{flux}	oron_{SSO}
2	81.6	69.8	16.4	20.6	13.9	11.8
10	81.1	76.4	15.4	19.9	13.3	10.7
18	90.0	80.3	14.4	18.0	12.8	10.7
26	94.6	104.0	13.5	17.6	12.5	9.5
34	87.7	96.1	14.6	18.4	12.4	9.6

C.4. Conclusions

Idealized simulations of Mistral and Tramontane were presented. Four different modeling setups were used, testing the impact of Coriolis force, surface fluxes, and SSO. The horizontal grid spacing was kept constant while different orographic resolutions were tested, leading to changes in cross-section and width of the Rhône Valley, and to lower wind speeds in the main Mistral and Tramontane area. This dependence on orographic smoothing could explain part of the pattern in wind speed bias described by Obermann et al. (2016a).

With decreasing orographic resolution, i.e. increasing smoothing factors, the wind speed at the borders of the flow increased in the simplest model setup, which could be attributed to an increase in valley width and an increase in the area affected by the flow. The longitudinal position of the wind speed maximum also changed depending on the smoothing by 10–45 km, which is in the same order of magnitude as the vortex diameter in the Gulf of Lion found by Allou et al. (2010) (12–28 km). Thus, a misplacement of Mistral wind speeds could influence the development of the vortices in coupled simulations. When using SSO, the location of the maximum wind speed changes less strong with increasing smoothing factor.

Therefore, a high-resolution orography seems to be beneficial for regional climate simulations, especially with coupled models. An SSO parameterization improves the Mistral and Tramontane wind speed patterns for coarse orography simulations, but a systematic wind speed underestimation due to channeling effects remains present.

Acknowledgements

The authors would like to thank the Center for Scientific Computing (CSC) of the Goethe University Frankfurt am Main for providing computational facilities. B. Ahrens acknowledges support by Senckenberg Biodiversity and Climate Research Centre (BiK-F), Frankfurt am Main. The authors acknowledge the support from the German Federal Ministry of Education and Research (BMBF) under grant MiKliP II (FKZ 01LP1518C).

Conflict of Interest

The authors declare no conflict of interest.

Graphical Abstract

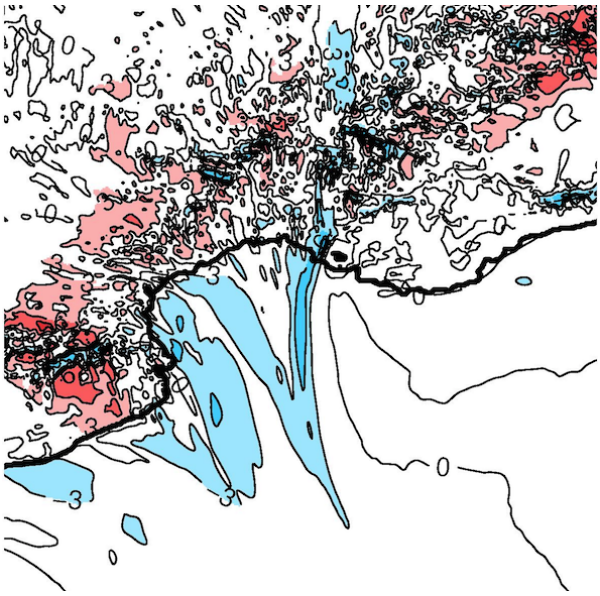

Figure C.6.: This study surveys the effect of orographic smoothing on Mistral and Tramontane by performing idealized COSMO-CLM simulations. Reduction of the orographic resolution leads to a change in wind pattern and a reduction of maximum wind speed. If a subgrid-scale orography parameterization is used, the smoothing effects are weaker, but a systematic decrease in wind speed with orographic smoothing is still present.

D. Paper 4: Mistral and Tramontane Wind Systems in Climate Simulations from 1950 to 2100

published as

Anika Obermann-Hellhund, Dario Conte, Samuel Somot, Csaba Zsolt Torma, and Bodo Ahrens, *Mistral and Tramontane wind systems in climate simulations from 1950 to 2100*, Climate Dynamics (2017), 1–11

Abstract

The characteristics of the mesoscale Mistral and Tramontane winds under changing climate conditions are of great interest for risk assessments. In this study, a classification algorithm is applied to identify Mistral and Tramontane-permitting sea-level pressure patterns, thus allowing for estimates of their future characteristics. Five simulations with three regional climate models on a 0.44° grid and five global circulation models are assessed for the representative concentration pathways (RCPs) 4.5 and 8.5. Regional climate simulations driven by ERA-Interim are used to test the classification algorithm and to estimate its accuracy. The derived Mistral and Tramontane time series are discussed. The results for the ERA-Interim period show that the classification algorithm and the regional climate models work well in terms of the number of Mistral and Tramontane days per year, but the results overestimate the average length of such events. For both the RCPs, only small changes in Mistral frequency were found in both regional and global climate simulations. Most simulations show a decrease in Tramontane frequencies and average period lengths during the 21st century. Regional climate simulations using RCP8.5 show fewer Tramontane events than those using RCP4.5.

Keywords General circulation models, Regional climate models, Time series, Model intercomparison, Mistral, Tramontane, Future climate, Bayesian network

D.1. Introduction

The Mistral and Tramontane are mesoscale winds in southern France. Both winds are channeled through valleys and impact the hydrological cycle of the Mediterranean Sea by causing deep-water formation in the Gulf of Lion (Marshall and Schott (1999); Somot et al. (2016)). The Mistral passes through the Rhône valley between the Alps and Massif Central from north to south, while the Tramontane emerges in the Aude valley between the Pyrenees and Massif Central (Fig. D.1). In these constricting valleys, both cold and dry winds accelerate before they reach the Mediterranean Sea at the Gulf of Lion. They are caused by similar synoptic situations, and consequently, they often coincide (Georgelin et al. (1994); Guenard et al. (2005)). Furthermore, Mistral and Tramontane winds can increase the risk and propagation of bush fires because of the dry polar air they bring to southern France (Pugnet et al. (2013)).

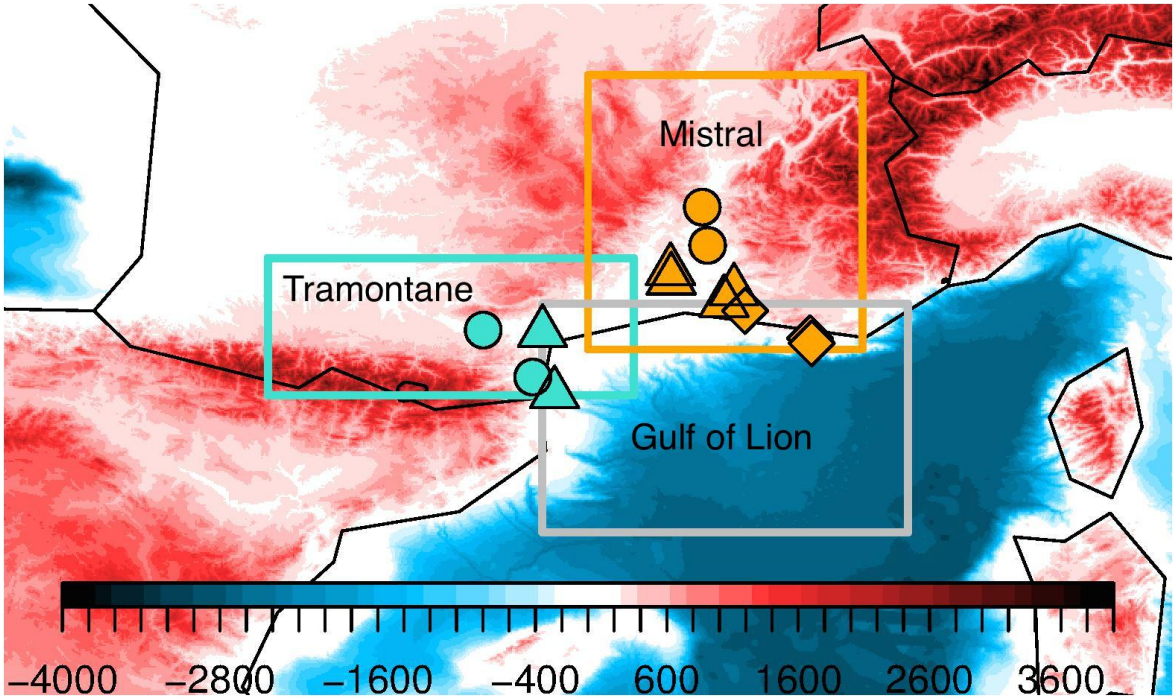

Figure D.1.: ETOPO1 (Amante and Eakins (2009)) orography (shaded in red) and bathymetry data (shaded in blue) in Mistral and Tramontane regions (units are meters). Analysis areas of Mistral and Tramontane valleys (outlined in orange and turquoise, respectively) and the Gulf of Lion (outlined in gray) area shown, as well as locations of stations for gust time series in Mistral (orange symbols) and Tramontane (turquoise symbols) areas such as in the valleys (circles) and plains (triangles), and close to the coast (squares).

In this study, a possible change in Mistral and Tramontane frequency and intensity under future climate conditions is surveyed. The frequency of occurrence and intensity of Mistral and Tramontane winds are of great interest not only for risk assessments under changing climatic conditions, but also for scientific reasons. Many case studies have dealt with Mistral and Tramontane events (e.g., Drobinski et al. (2005); Berthou et al. (2016)). Obermann et al. (2016a) found the sea-level pressure fields associated with an occurrence of Mistral and Tramontane to be simulated equally well in simulations with 0.088 to 0.44° grid spacing, while higher resolution simulations perform better in terms of wind speed and wind direction. Herrmann et al. (2011) and Ruti et al. (2008) found the representation of wind speeds in the Mediterranean region to be improved by increasing the resolution of the model employed.

Numerous studies deal with near-surface wind speeds over Europe in climate projections (see Pryor et al. (2006, 2012); Rockel and Woth (2007)), as well as changes in wind energy potential (e.g., Hueging et al. (2013)) and loss potential due to windstorms (Pinto et al. (2012)). Rockel and Woth (2007) found that the number of storm peaks (gusts greater then 8 Bft) increase over Western and Central Europe when applying the Special Report on Emissions Scenarios (SRES, Nakicenovic and Swart (2000)) A2 scenario, while their number decreases over the Western Mediterranean Sea. This is consistent with the findings of Beniston et al. (2007), who found an increase in simulated 90th percentiles of surface wind speeds north of the Alps and a decrease south of the Alps in SRES A2 simulations. Najac et al. (2008, 2011) projected that the wind speeds in the Mistral and Tramontane area in 2046–2065 will be lower than those in 1971–2000 in an ensemble of SRES A1B simulations. Somot et al. (2006) found a decrease in wind stress over the Mediterranean Sea in a SRES A2 simulation, especially in the Gulf of Lion area. Hueging et al. (2013) and Nikulin et al. (2011) projected a decrease in wind energy density and maximum wind speed in regional climate simulations driven by SRES A1B global simulations. However, to the best knowledge of the authors, the frequencies of occurrence of Mistral and Tramontane events in climate models have not yet been surveyed.

In this paper, a method to estimate future Mistral/Tramontane (M/T) occurrence frequencies is presented. A classification algorithm was applied to identify sea-level pressure patterns that permit Mistral and Tramontane winds, following the approach of Obermann et al. (2016a), who used empirical orthogonal functions of mean sea-level pressure fields and mapped it to Mistral and Tramontane time series derived from station observations. Regional climate model (RCM) simulations driven by ERA-Interim data (Dee et al. (2011)) were used to calibrate the classification algorithm and to estimate its accuracy. Five simulations with three RCMs at 0.44° grid spacing from the Med-CORDEX framework (Ruti et al. (2016)) driven by global circulation models (GCMs) from the fifth phase of the Climate Model Intercomparison Project (CMIP5, Taylor et al. (2012)) were then evaluated. Climate projections for two representative concentration pathways (RCPs, Moss et al. (2010)) are available within the Med-CORDEX dataset (RCP4.5 and

RCP8.5) and are discussed in this paper. In addition, the wind speeds during Mistral and Tramontane events are discussed.

This paper is structured as follows. The observation and simulation data are discussed in Section D.2. Then, the methods used are explained in Section D.3, followed by the results and discussion in Section D.4. The last section contains a summary of this work and the conclusions.

D.2. Data

The data used in this study include station observations, reanalysis data, GCMs, and RCMs. Table D.1 gives an overview of the GCMs and RCMs.

Table D.1.: GCM and RCM simulations and modeling groups. RCMs were forced by the GCMs listed in the same row of the table. Acronyms are explained in the text.

GCM		RCM	
Name	Group	Name	Group
MPI-ESM-LR	MPI-M	CCLM4-8-18	GUF
CMCC-CM	CMCC	CCLM4-8-19	CMCC
MPI-ESM-MR	MPI-M	RegCM4-3	ICTP
HadGEM2-ES	MOHC/INPE	RegCM4-3	ICTP
CNRM-CM5	CNRM-CERFACS	ALADIN52	CNRM

D.2.1. Observational Mistral and Tramontane Time Series

Mistral and Tramontane time series derived from station data are used for both training and testing of the classification algorithm for identifying Mistral and Tramontane situations. The daily gust time series from 13 Météo-France stations in the Mistral and Tramontane regions (locations are shown in Fig. D.1) provide gust data with wind velocities greater than 16 m/s from the dominant Mistral and Tramontane directions at each individual station. These observation data are available for the period 1981–2010. The days were tagged based on the occurrence of the two wind systems of interest. The method for Mistral and Tramontane identification is described in Obermann et al. (2016a), where this method was applied to the period 2001–2009. Table D.2 gives the resulting numbers of Mistral and Tramontane days in 1981–2010.

Table D.2.: Observed frequency of Mistral and Tramontane days in 1981–2010.

1981–2010	Tramontane	No Tramontane	Sum
Mistral	1382	368	1750
No Mistral	2129	7078	9207
Sum	3511	7446	10957

D.2.2. ERA-Interim

The reanalysis dataset ERA-Interim (Dee et al. (2011)) is used as a forcing for the evaluation runs of the RCMs in this study. It is calculated with a grid resolution of about 80 km. Sea-level pressure fields from ERA-Interim are used together with the observational Mistral and Tramontane time series to train the classification algorithm. ERA-Interim data were provided by the European Centre for Medium-Range Weather Forecasts (ECMWF) database.

D.2.3. Global Circulation Models (GCMs)

The Earth System Model (MPI-ESM, Mauritsen et al. (2012); Giorgetta et al. (2013)) of the Max-Planck-Institut für Meteorologie (Max Planck Institute for Meteorology, MPI-M) comprises the atmosphere model ECHAM6 (Stevens et al. (2013)) and the ocean model MPIOM (Jungclaus et al. (2013)). The two model configurations, LR (low resolution) and MR (medium resolution), differ in the number of levels in the atmosphere (LR: 47, MR: 95) and ocean grid spacing (LR: 1.5 °, MR: 0.4 °).

ECHAM5, (Roeckner et al. (2003)) with a grid spacing of about 0.75 ° and 31 vertical levels, is the atmospheric component of the Centro Euro-Mediterraneo sui Cambiamenti Climatici (CMCC) Climate Model (CMCC-CM). In this model, the ocean is represented by OPA 8.2 (Madec et al. (1997)) in the ORCA2 configuration (0.5–2 ° grid spacing).

HadGEM2-ES is the earth system version of the Hadley Centre Global Environment Model version 2 (HadGEM2, Martin et al. (2011)). It has a grid spacing of 1.25–1.875 ° in the atmosphere and 0.33–1.0 ° in the ocean component. Simulations were done by the Met Office Hadley Centre (MOHC) and Instituto Nacional de Pesquisas Espaciais (INPE).

CNRM-CM5 (Voldoire et al. (2013)) consists of the atmosphere model ARPEGE-climat v5.2 (Météo-France (2009)) with a grid spacing of about 1.4 °, 31 vertical levels, and the ocean model NEMO v3.2 (Madec (2008)), with a grid spacing of 0.3–1 ° and 43 vertical levels. The simulations used in this study were produced by the Centre National de Recherches Météorologiques/Centre Européen de Recherche et Formation Avancée en Calcul Scientifique (CNRM-CERFACS).

D.2.4. Regional Climate Models (RCMs)

The regional climate simulations investigated in this study were prepared in the Med-CORDEX framework (Ruti et al. (2016)) and HyMeX program (Drobinski et al. (2014)), and were performed on the Med-CORDEX domain (encompassing the Mediterranean

and Black Sea, as well as the surrounding land areas). Data from five different combinations of GCMs and atmosphere-only RCMs are available in the MedCORDEX database on 0.44° grids. In this study, the simulations are identified by the name of the RCM for ERA-Interim driven simulations. GCM driven simulations are identified by the GCM's name followed by the name of the RCM applied.

Simulations with the COSMO-CLM (CCLM) model (see Rockel et al. (2008)) were performed at two institutions: CMCC and Goethe University, Frankfurt (GUF). Simulations driven by ERA-Interim and MPI-ESM-LR were performed at GUF with CCLM4-8-18. The CCLM simulations produced by CMCC used model version CCLM4-8-19, and were driven by ERA-Interim and CMCC-CM.

RegCM4-3 (see Giorgi et al. (2012)) is a hydrostatic model. The RegCM4-3 runs were performed by the International Center for Theoretical Physics (ICTP).

CNRM performed the simulations with the limited area version of ARPEGE, ALADIN version 5.2 (Colin et al. (2010); Herrmann et al. (2011)) driven by ERA-Interim and CNRM-CM5.

D.2.5. Temporal and Spatial Interpolation of Simulation Datasets

Sea-level pressure datasets were interpolated bilinearly to a common 0.25° grid in the area -20.25–20.25° E and 25.75–55.5° N (treated in the same way as sea-level pressure fields in Obermann et al. (2016a)). Unless stated otherwise, calculations are based on daily means. The mean wind speeds in Mistral and Tramontane areas were obtained by calculating spatial averages for the areas indicated in Fig. D.1.

D.3. Methods

D.3.1. Sea-Level Pressure Pattern Classification

A classifying algorithm based on an empirical orthogonal function (EOF) analysis in conjunction with a Bayesian network was used to determine on which days the simulated large-scale sea-level pressure fields were likely to produce a Mistral or Tramontane event. For an introduction to Bayesian networks, see Scutari (2010). An introduction to EOF analysis can be found in von Storch and Zwiers (2001).

In this study, we follow the approach of Obermann et al. (2016a), where the classification process is discussed in detail. In both cases, a similar classification algorithm is used for identifying Mistral and Tramontane days in daily mean sea-level pressure fields from Med-CORDEX regional climate simulations. Therefore, only differences between earlier work and the present approach are discussed here.

The classification algorithm consists of the following three steps: preparation of input data, structure learning and training, and processing the output. In contrast to the above-mentioned paper, the EOFs were calculated from ERA-Interim sea-level pressure fields for the time interval 1981–2010 instead of 2000–2008. Although calculated for a different time period, the resulting EOFs look very much alike. A longer time series (30 years instead of 9 as in Obermann et al. (2016a)) of fewer principal components (the first 50 instead of the first 100) of ERA-Interim EOFs and the observed M/T time series were used for training. Higher numbers of EOFs were tested with the 30-yr training period, but did not significantly increase the number of correctly identified M/T days. Furthermore, large numbers of EOFs would introduce noise to the classification algorithm by adding small scale variations because Mistral and Tramontane winds are mesoscale phenomena driven by sea-level pressure gradients on scales of hundreds of kilometers.

Given a set of principal components from the EOF analysis of ERA-Interim, an RCM, or a GCM, the trained Bayesian networks' output is a number indicating if a day is likely to be a Mistral or Tramontane day or not. Values above a certain threshold were regarded as Mistral or Tramontane days, while those below the threshold were regarded as non-Mistral or non-Tramontane days. The threshold was chosen in such a way that the numbers of Mistral and Tramontane days in the overlapping time period of observed time series and simulations were the same. The thresholds were kept constant over the whole simulation period for the 1950–2100 simulations.

The proportion correct (PC) score is the percentage of days on which simulations and observations agree on the occurrence of a Mistral as well as a Tramontane event during a given time period. The mean obtained PC score (all year) for ERA-Interim was about 70 % for training periods longer than 9 years. The full 30 years of available data were

used for training because the PC score varies depending on the days used for training, and an extended training period smooths possible distortions introduced by exceptional individual random samples.

D.3.2. Testing the Classification Algorithm

To get an estimate of the classification accuracy, the classification algorithm was applied to the ERA-Interim-driven RCM simulations. Figure D.2 shows the number of Mistral and Tramontane days per year (i.e., from December of the previous year to November of the actual year) identified by the classification algorithm for ERA-Interim and ERA-Interim driven simulations. Correlations of simulated and observed days per year were 0.44 and higher for Mistral as opposed to 0.67 and higher for Tramontane, respectively (Table D.3). Table D.3 also shows the PC scores of the ERA-Interim-driven simulations with the observation Mistral and Tramontane time series as reference. The PC score reaches values between $66.6\,\%$ and $70.6\,\%$ in the ERA-Interim period. The obtained PC scores of the RCMs were higher than those in the trivial cases. If all days were identified as non-Mistral and non-Tramontane days, a PC score of 64.60 % would be reached. For the second trivial case, i.e., if all days were identified as Mistral and Tramontane days, the resulting PC score would be 12.61 %.

Table D.3.: Proportion correct (PC) score, correlation, and average period length of Mistral and Tramontane events from ERA-Interim and ERA-Interim-driven RCMs for the years 1982 to 2010 (1982 to 2008 for RegCM4-3) in days.

	PC score	Correlation days/year		Average period length	
Simulation		Mistral	Tramontane	Mistral	Tramontane
ERA-Interim	70.6	0.61	0.78	2.1	3.3
CCLM4-8-18	68.8	0.47	0.72	2.0	2.9
CCLM4-8-19	68.5	0.44	0.67	2.0	2.9
RegCM4-3	66.6	0.55	0.77	2.3	3.5
ALADIN52	68.3	0.57	0.67	2.2	2.9
Observation	100.0	1.00	1.00	1.7	2.5

All simulations are able to reproduce the number of M/T days per year, but the results overestimate the period length. If the Mistral and Tramontane days were distributed randomly, the average period length would be ≈ 1.2 days for Mistral winds and ≈ 1.5 days for Tramontane winds. The observed time series, however, shows higher average period lengths (1.7 for Mistral and 2.5 for Tramontane winds). The simulations

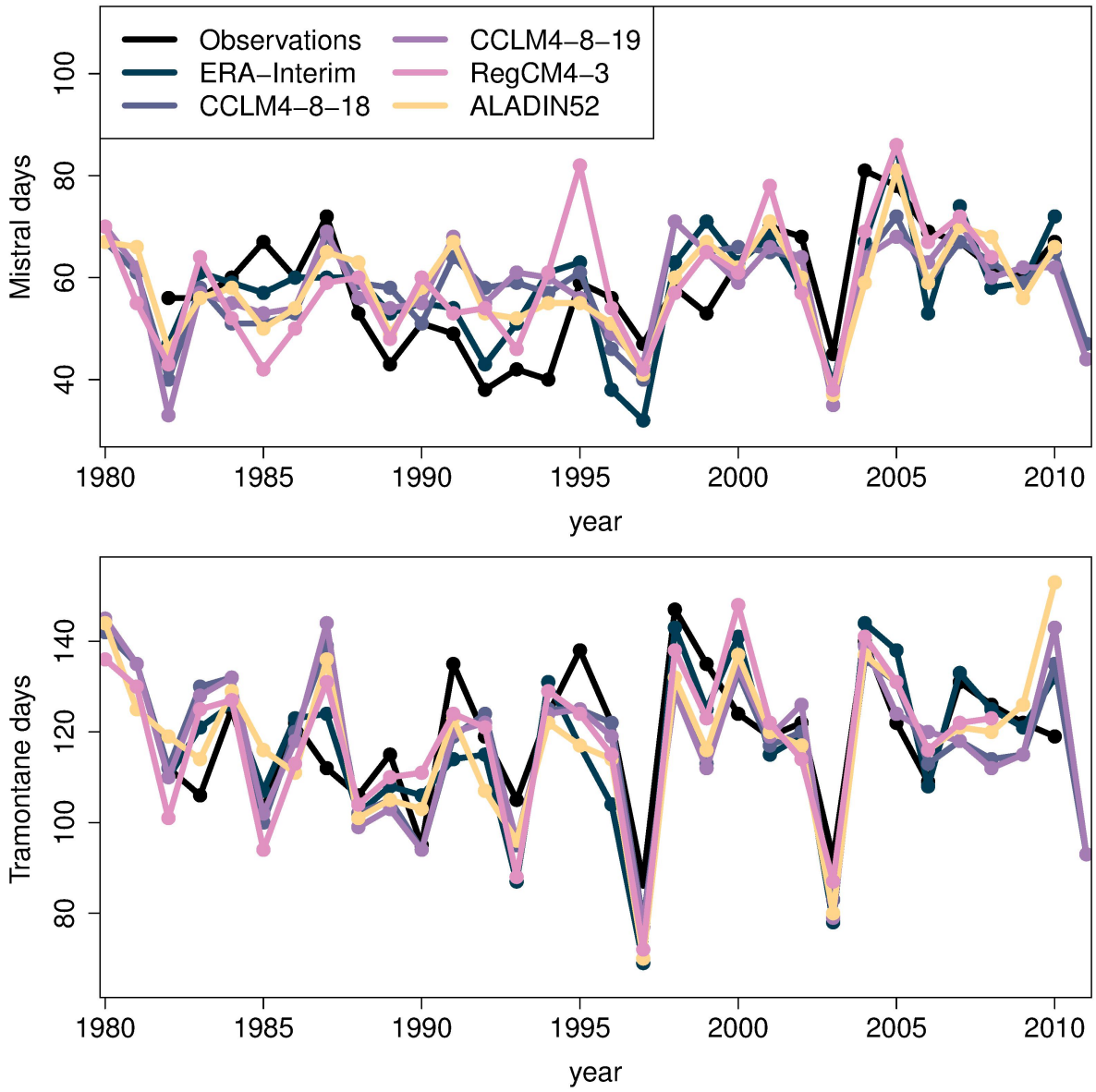

Figure D.2.: Number of Mistral and Tramontane days per year in ERA-Interim, ERA-Interim-driven simulations, and observations.

overestimate the period length by 17–35%. The reason for this could be an erroneous modeling of blocking situations, which causes the simulation to change too rarely from an M/T to a non-M/T situation and vice versa. The PC score of the RCMs with ERA-Interim as reference is 81.2–83.5%, which is in agreement with the results of Sanchez-Gomez et al. (2009) on the reproduction of ERA-Interim weather regimes in RCMs.

A pair of CCLM4-21-2 simulations (one of them coupled to NEMO, Akhtar et al. (2014)) was used to test the influence of coupling (not shown). The coupled run shows a slightly higher PC score than its uncoupled counterpart. The average period length is not influenced by coupling. Therefore, the coupling has a minor significant effect on Mistral and Tramontane time series obtained from sea-level pressure patterns. This is consistent with the results of Artale et al. (2010) for RegCM3 and Herrmann et al. (2011) for ALADIN simulations.

D.4. Results and Discussion

D.4.1. GCM Simulations

Tables D.4 and D.5 show the 30-yr means and standard deviations of M/T days per year for the GCMs. Values were calculated only if at least 20 years of simulation data were available for the given time period (e.g., 1981–2005 instead of 1981–2010 for the GCM simulations ending in 2005).

Table D.4.: Mean $\bar{x}$ and standard deviation σ of GCM simulated Mistral days per year for 1981–2010 and differences expressed as $\Delta\bar{x}$ and $\Delta\sigma$ to the values of that period. Values were calculated only if at least 20 years of simulation data were available for the given time period. Means that passed a Student's t-test and standard deviations that passed an F-test in relation to the 1981–2010 values at the 95% significance level are shown in bold.

Model	Simulation	1951 –1980		1981 –2010		2011 –2040		2041 –2070		2071 –2100	
		$\Delta\bar{x}$	$\Delta\sigma$	$\bar{x}$	σ	$\Delta\bar{x}$	$\Delta\sigma$	$\Delta\bar{x}$	$\Delta\sigma$	$\Delta\bar{x}$	$\Delta\sigma$
MPI-ESM-LR	historical	–4	–4	58	12	–	–	–	–	–	–
	rcp45	–	–	–	–	–3	–2	–1	–2	0	–3
	rcp85	–	–	–	–	+1	–3	–1	–3	+2	–2
CMCC-CM	historical	+3	**–4**	57	12	–	–	–	–	–	–
	rcp45	–	–	–	–	–1	+1	–1	–2	–4	–2
	rcp85	–	–	–	–	+1	–2	0	**–5**	–2	**–5**
MPI-ESM-MR	historical	+4	–3	57	12	–	–	–	–	–	–
	rcp45	–	–	–	–	+1	–2	+2	–1	+5	0
	rcp85	–	–	–	–	+1	+1	**+7**	–3	+6	–1
HadGEM2-ES	historical	0	11	56	9	–	–	–	–	–	–
	rcp45	–	–	–	–	+2	+3	–2	+3	0	+2
	rcp85	–	–	–	–	+1	+2	+3	+4	+2	+3
CNRM-CM5	historical	**–6**	+1	57	9	–	–	–	–	–	–
	rcp45	–	–	–	–	–4	+2	–2	0	–1	0
	rcp85	–	–	–	–	–3	–1	–2	+2	–3	+3
Observation	–	–	–	58	11	–	–	–	–	–	–

Table D.5.: Same as Table D.4 but for Tramontane days in GCMs.

Model	Simulation	1951 –1980		1981 –2010		2011 –2040		2041 –2070		2071 –2100	
		$\Delta\bar{x}$	$\Delta\sigma$	$\bar{x}$	σ	$\Delta\bar{x}$	$\Delta\sigma$	$\Delta\bar{x}$	$\Delta\sigma$	$\Delta\bar{x}$	$\Delta\sigma$
MPI-ESM-LR	historical	–4	–4	115	20	–	–	–	–	–	–
	rcp45	–	–	–	–	0	–2	+1	–4	+2	–4
	rcp85	–	–	–	–	+3	–3	+1	–5	+2	–4
CMCC-CM	historical	+3	–6	116	20	–	–	–	–	–	–
	rcp45	–	–	–	–	–3	–1	–5	**–7**	–9	–6
	rcp85	–	–	–	–	–5	–6	**–10**	**–7**	**–12**	**–8**
MPI-ESM-MR	historical	–4	+2	117	16	–	–	–	–	–	–
	rcp45	–	–	–	–	–4	0	–7	+2	–2	+4
	rcp85	–	–	–	–	**–9**	+2	–5	–2	**–9**	–2
HadGEM2-ES	historical	–1	+3	116	15	–	–	–	–	–	–
	rcp45	–	–	–	–	–1	+4	–6	+1	–6	+1
	rcp85	–	–	–	–	–5	+1	–1	0	–3	+6
CNRM-CM5	historical	**–11**	+3	116	14	–	–	–	–	–	–
	rcp45	–	–	–	–	–7	+5	–4	+6	–4	+5
	rcp85	–	–	–	–	**–11**	–1	–6	0	**–10**	**+8**
Observation	–	–	–	118	14	–	–	–	–	–	–

The GCMs show no significant change in Mistral days per year between the reference period (1981–2010) and the end of the 21st century. All GCM simulations except MPI-ESM-LR showed a decrease in Tramontane days per year. Most of them show a significant decrease in Tramontane days in RCP8.5, but do not agree if the change in number of Mistral events is stronger in RCP4.5 or RCP8.5. Few periods show a significant difference in mean or variance at the 95 % significance level compared to the period 1981–2010.

D.4.2. RCM Simulations

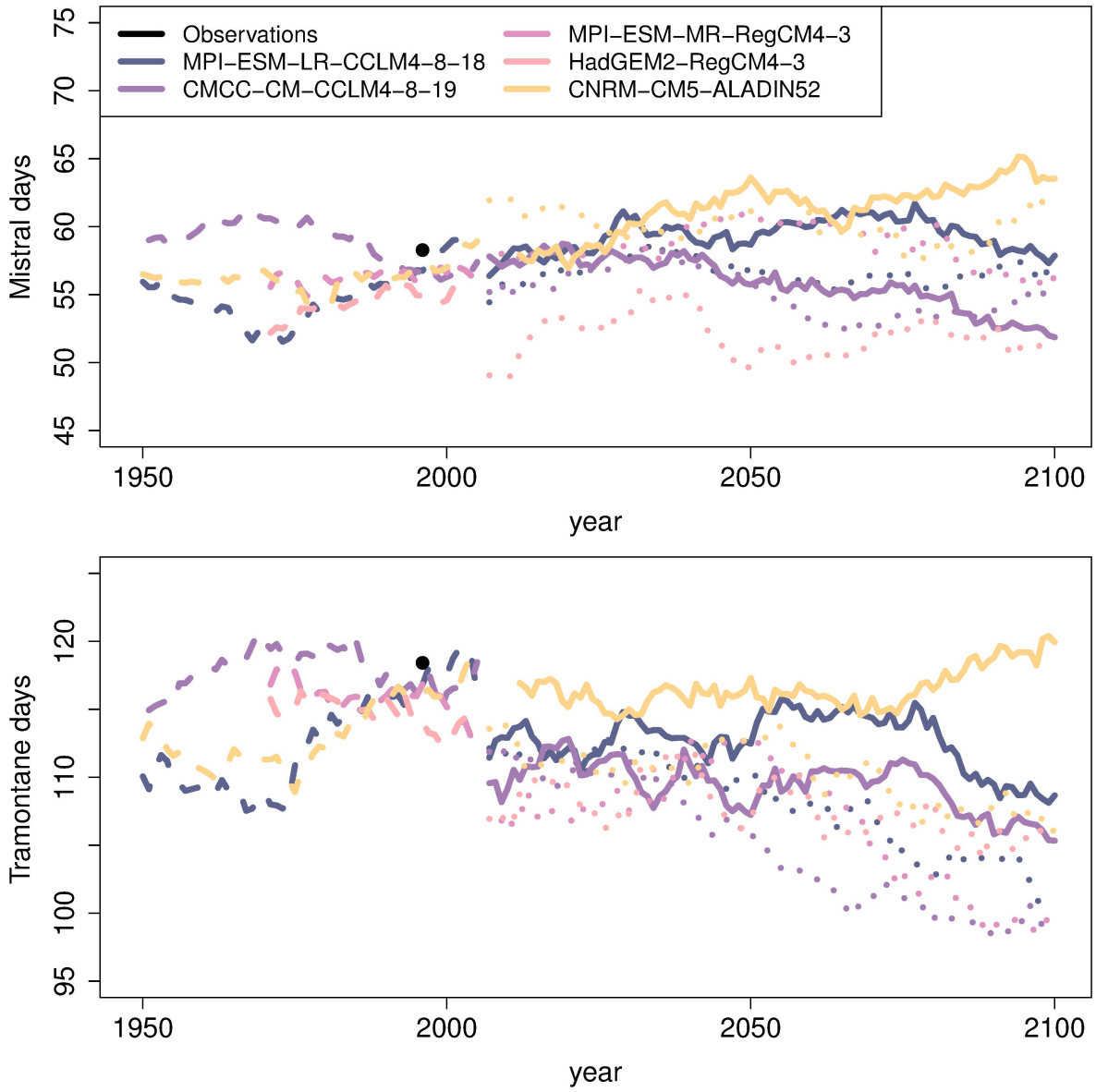

Figure D.3.: Thirty-year running mean of Mistral and Tramontane days per year in historical runs (dashed), RCP4.5 (full lines), and RCP8.5 (dotted lines) scenarios and mean of observed Mistral and Tramontane days per year (black dots).

Figure D.3 shows the 30-yr running mean of M/T days per year for RCMs in the 1950–2100 period. Tables D.6 and D.7 give the 30-yr averages and standard deviations of windy days per year. When both the RCP4.5 and RCP8.5 scenarios are available,

the mean number of windy days per year is lower in the RCP8.5 scenario than in the RCP4.5 scenario for most models. Besides HadGEM2-RegCM4-3 showing a smaller number of Mistral days in summer and a larger number in winter, the simulations agree on the distribution of windy days over the seasons (not shown).

Table D.6.: Overview analog to Table D.4 but for Mistral days in RCMs.

Model	Simulation	1951 –1980		1981 –2010		2011 –2040		2041 –2070		2071 –2100	
		$\Delta\bar{x}$	$\Delta\sigma$	$\bar{x}$	σ	$\Delta\bar{x}$	$\Delta\sigma$	$\Delta\bar{x}$	$\Delta\sigma$	$\Delta\bar{x}$	$\Delta\sigma$
MPI-ESM-LR-CCLM4-8-18	historical	–3	0	57	11	–	–	–	–	–	–
	rcp45	–	–	–	–	+3	–1	+5	0	+4	–1
	rcp85	–	–	–	–	+2	–1	0	**–4**	+1	–1
CMCC-CM-CCLM4-8-19	historical	+3	-3	57	10	–	–	–	–	–	–
	rcp45	–	–	–	–	+1	0	–2	–1	–3	0
	rcp85	–	–	–	–	–1	–1	–2	–2	–4	–3
MPI-ESM-MR-RegCM4-3	historical	–	–	56	12	–	–	–	–	–	–
	rcp85	–	–	–	–	+2	+1	+4	–1	+1	+2
HadGEM2-RegCM4-3	historical	–	–	55	10	–	–	–	–	–	–
	rcp85	–	–	–	–	-2	+4	–4	+1	–3	+3
CNRM-CM5-ALADIN52	historical	–1	**–4**	57	12	–	–	–	–	–	–
	rcp45	–	–	–	–	+2	–1	+6	+1	+5	–1
	rcp85	–	–	–	–	+3	–2	+5	–3	+2	+2
Observation	–	–	–	58	11	–	–	–	–	–	–

Table D.7.: Overview analog to Table D.4 but for Tramontane days in RCMs.

Model	Simulation	1951 –1980		1981 –2010		2011 –2040		2041 –2070		2071 –2100	
		$\Delta\bar{x}$	$\Delta\sigma$	$\bar{x}$	σ	$\Delta\bar{x}$	$\Delta\sigma$	$\Delta\bar{x}$	$\Delta\sigma$	$\Delta\bar{x}$	$\Delta\sigma$
MPI-ESM-LR-CCLM4-8-18	historical	**–13**	–3	116	19	–	–	–			
	rcp45	–	–	–	–	–6	–4	–3	–2	–8	–5
	rcp85	–	–	–	–	–6	–5	**–11**	**–7**	**–15**	–5
CMCC-CM-CCLM4-8-19	historical	+3	**–6**	116	18	–	–	–			
	rcp45	–	–	–	–	–5	0	–7	**–6**	**–9**	–5
	rcp85	–	–	–	–	–6	**–6**	**–13**	–5	**–17**	**–8**
MPI-ESM-MR-RegCM4-3	historical	–	–	116	17	–	–	–			
	rcp85	–	–	–	–	–8	+1	–6	–3	**–15**	–3
HadGEM2-RegCM4-3	historical	–	–	114	13	–	–	–			
	rcp85	–	–	–	–	–7	+3	-4	+5	–9	**+7**
CNRM-CM5-ALADIN52	historical	–4	–2	116	15	–	–	–			
	rcp45	–	–	–	–	–1	0	0	0	+2	+1
	rcp85	–	–	–	–	–6	0	–2	–2	–9	+6
Observation	–	–	–	118	14	–	–	–	–	–	–

Figure D.4 shows the 30-yr running mean of M/T period lengths for RCMs in the 1950–2100 period. With more than 3.5 days for Tramontane winds, HadGEM2-RegCM 4-3 shows larger average period lengths than the other models, while both CCLM versions show short period lengths of less than 2 days for Mistral winds and about 2.5 days for Tramontane winds. MPIESM-RegCM4-3 and both CCLM simulations for RCP8.5

show a decrease in Tramontane period lengths over the 21st century. Nevertheless, the observed period lengths stay above the expected period lengths for the case of randomly distributed events.

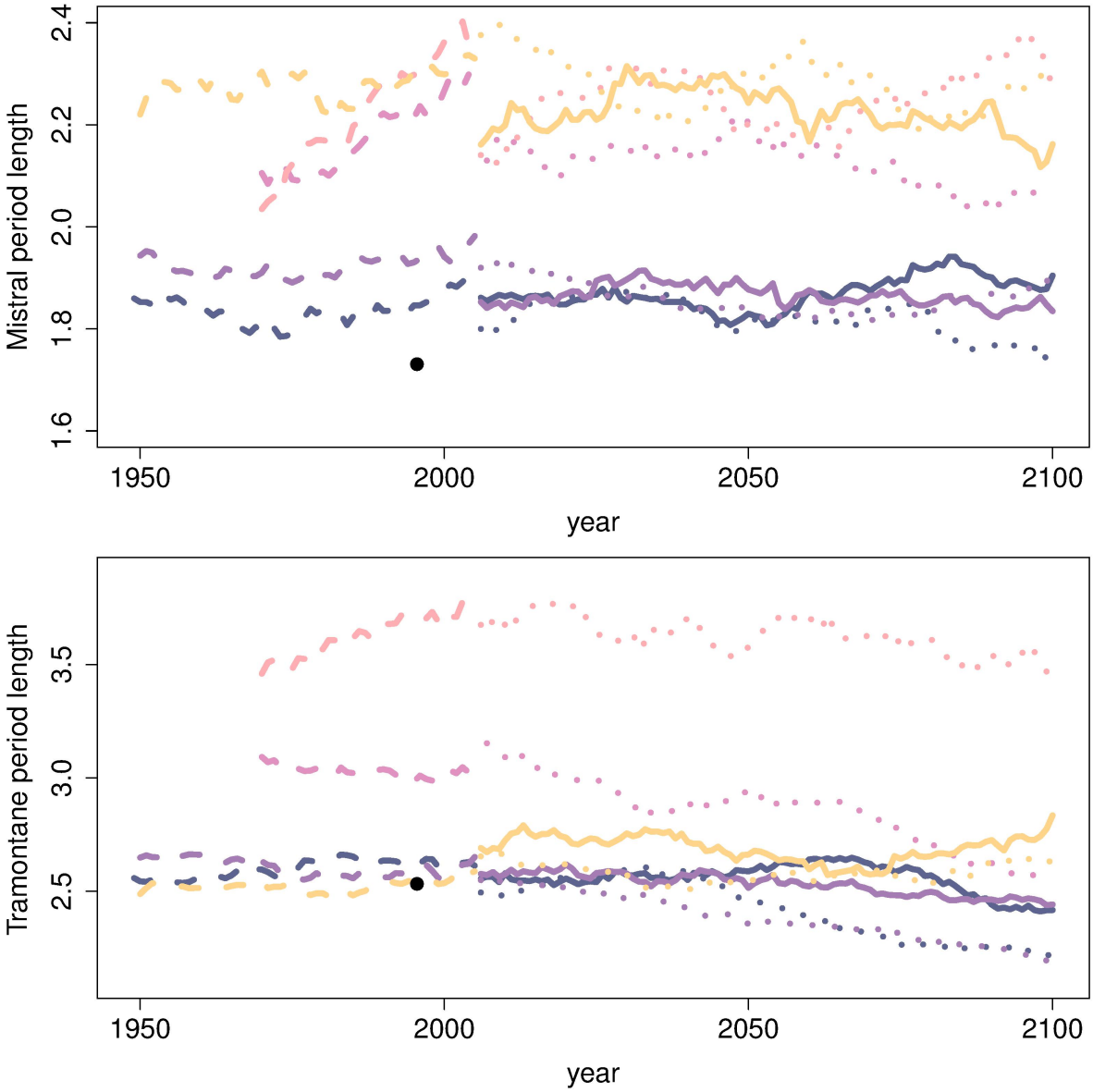

Figure D.4.: Time series of 30-yr running means of Mistral and Tramontane period lengths in days. Legend as in Fig. D.3.

D.4.3. GCM constraint on RCMs

To estimate the influence of the driving GCM on the M/T representation in RCMs, the PC score of the two setups MPI-ESM-LR-CCLM4-8-18 and CMCC-CM5-CCLM4-8-19 with the driving GCM as reference is used. These runs provide the longest time series of the models in this study, and both RCP4.5 and RCP8.5 simulations are available. The PC scores are given in Table D.8. The PC score between the RCM simulations and the driving GCMs is about 80%. This shows that the RCMs are constrained by the driving GCM, consistent with the results of Sanchez-Gomez et al. (2009), who found the RCMs ALADIN, CCLM, and RegCM to reproduce similar weather regimes as the driving dataset in about 70–90 % of the cases. When looking at Mistral days only, the proportion of correct score reaches higher values than for Tramontane winds.

Table D.8.: PC score of CCLM runs with driving GCMs as reference.

GCM	RCM	historical	rcp45	rcp85
MPI-ESM-LR	CCLM4-8-18	78.3	78.2	78.5
CMCC-CM	CCLM4-8-19	81.1	77.3	82.1

Torma and Giorgi (2014) found temperature and precipitation in RegCM simulations to be more sensitive to the applied convection scheme than to the driving GCM in some regions of the Med-CORDEX domain. Such a dependency on internal model physics could also affect pressure and wind speed. Different physics schemes, therefore, could cause RegCM4-3 and CCLM to show fewer M/T days than the driving GCMs and CNRM-CM5-ALADIN52 to show more M/T days than the driving GCMs. Furthermore, the RCMs show stronger changes than their driving GCMs for Tramontane winds. The higher agreement with GCMs in the Mistral case could be due to the fact that the Alps are more visible in coarser grids than the Pyrenees, and therefore higher resolution runs are necessary to simulate the Tramontane winds well. Another possible explanation is that pressure pattern details are less important for Mistral winds because the Alps strongly constrain them.

D.4.4. Pressure Pattern Persistence

The autocorrelation of principal components time series with a lag of one or more days can be used to determine the persistence of pressure patterns. Here, we use the number of lagged days after which the autocorrelation decreases below 0.5 to evaluate the persistence of pressure patterns. For ERA-Interim, this value is 0–1 days for most principal components. Only the first three principal components show

higher persistence (3, 5, and 2 days, respectively). All simulations show an increase in persistence of the second principal component in both the RCP4.5 and RCP8.5 simulations compared to the historical simulations, with RCP8.5 runs showing the highest persistence. The RCM simulations show longer persistence in several higher principal components, while the GCMs show no persistence in higher order principal components.

D.4.5. Wind Speed Changes

Figure D.6 shows the mean wind speed in Mistral and Tramontane areas (both including the Gulf of Lion area, areas as indicated in Fig. D.1) for M/T days and non-M/T days. The M/T days show significantly higher wind speeds than the non-M/T days for all simulations. Both RegCM4-3 simulations show a smaller difference between M/T and non-M/T days than the other RCMs. Figure D.5 shows the difference in wind speed 90th percentiles between the periods 2071–2100 and 1981–2010. The Gulf of Lion region shows the largest differences. The changes in the RCP8.5 simulations are greater than those in RCP4.5.

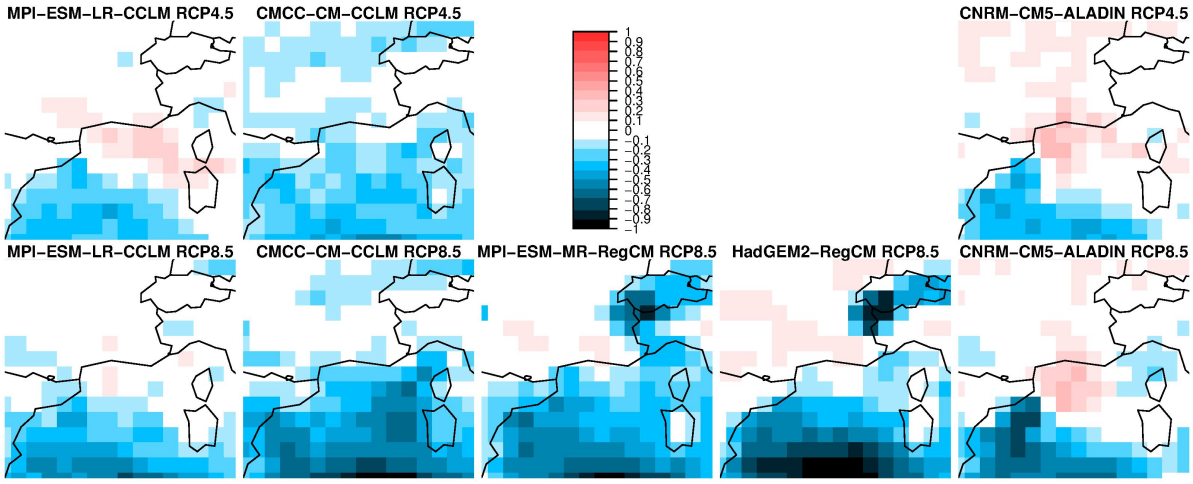

Figure D.5.: Difference in 90th percentile of daily mean surface wind speed between the periods 2071–2100 and 1981–2010 (units are meters per second).

Fig. D.5 shows a decrease in the wind speed 90th percentile in the Gulf of Lion for all RCM simulations. This decrease could be due to fewer Tramontane events. The two models that have more classified Mistral days in 2071–2100 (CNRM-CM5-ALADIN52 and MPI-ESM-LR-CCLM4-8-18) show a small decrease (CNRM-CM5-ALADIN52 for

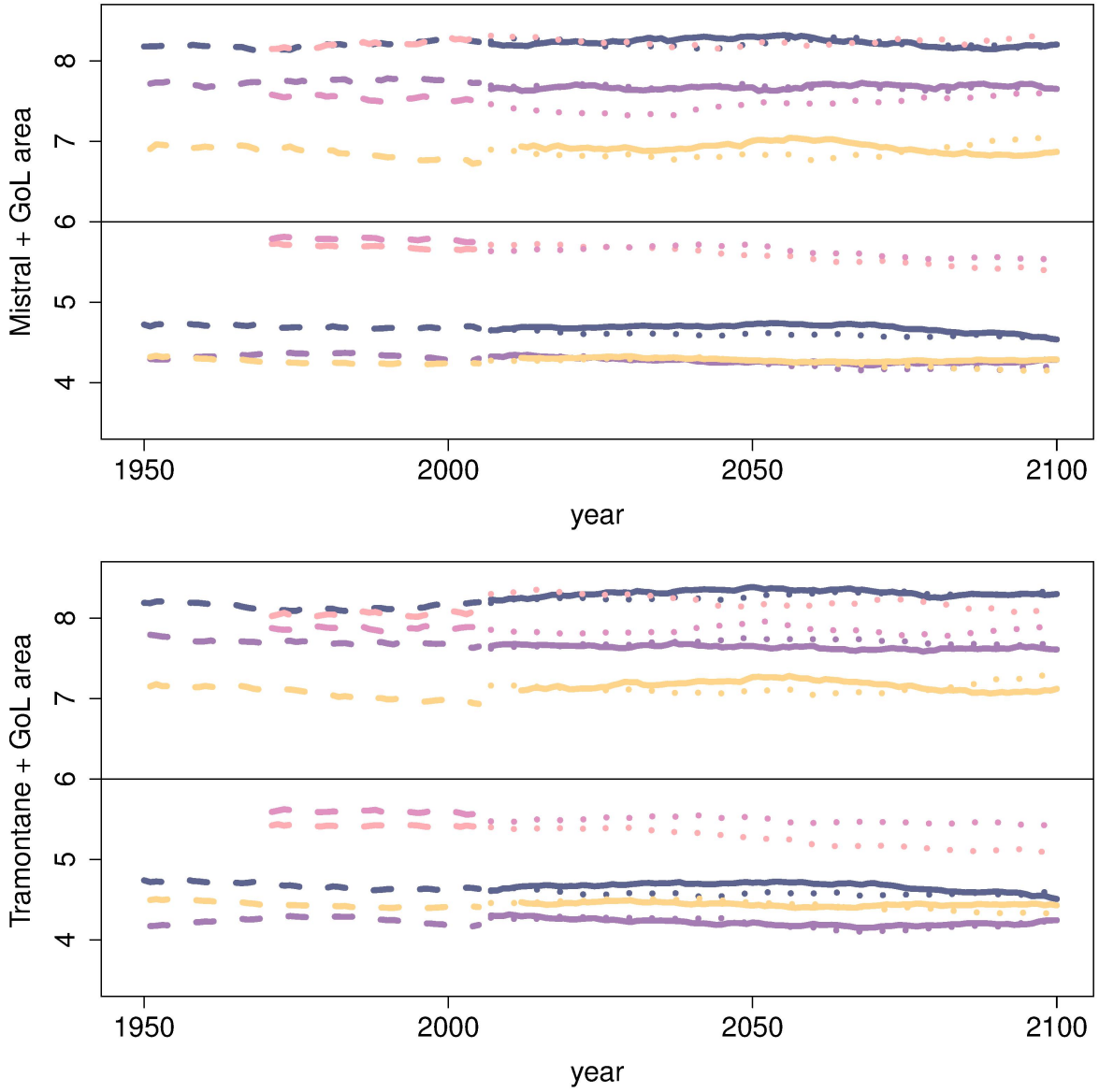

Figure D.6.: Thirty-year running mean wind speed on days with Mistral and Tramontane (upper half of figures) and without Mistral and Tramontane (lower half of figures) in the Mistral, Tramontane, and Gulf of Lion (GoL) areas. Legend as in Fig. D.3.

RCP8.5 even shows an increase) in the 90th percentile in the Mistral area. Most simulations show a decrease in the same areas as was found for SRES scenarios A1B (e.g., Najac et al. (2008, 2011)) and A2 (Somot et al. (2006)).

D.4.6. Classification Quality in Future Climate Conditions

The climate could change to a state in which different types of Mistral and Tramontane winds occur that were not present in the training period and, therefore, could not be detected by the classification algorithm. The principal components of several EOFs show changes in their mean during the 21st century (data not shown), which is indicative of a change in sea-level pressure patterns. Since Mistral and Tramontane winds depend on orographic effects such as channeling, as well as pressure gradients, a spatial shift in the pressure patterns relative to the orography should lead to a different number of M/T days. If the classification algorithm happened to be erroneous and, therefore, failed to identify M/T days, there should be a drift in the wind speed during M/T days and non-M/T days to more similar values, i.e., the gap in wind speed between M/T and non-M/T days decreases. If more days with M/T were classified as non-M/T, the average non-M/T wind speed would increase, while non-M/T days classified as M/T day would lead to a decrease in M/T-day wind speed. Since the mean wind speeds during neither M/T nor non-M/T days show a large change in the 21st century, this effect appears unlikely.

D.5. Summary and Conclusion

In this study, Mistral and Tramontane frequencies of occurrence in climate simulations ranging from 1950 to 2100 were derived from simulated sea-level pressure patterns using EOFs and a Bayesian network. The results for the ERA-Interim period show that the classification algorithm and RCMs are able to reproduce the number of Mistral and Tramontane days per year, while the period length is overestimated. This overestimation could be due to erroneous simulation of blocking situations in the models.

The five simulations with three RCMs and five GCMs in this study show only small changes in Mistral frequency in RCP4.5 and RCP8.5 projections, but a significant decrease in Tramontane frequency. Most GCMs and RCMs show a decrease in Tramontane days per year, but changes are stronger in RCM simulations. This leads to the conclusion that future climate could lead to a change in Tramontane frequency, while the average wind speed during Tramontane events is not projected to change.

The wind speed 90th percentile of RCP8.5 is lower than that of RCP4.5 for most simulations. The decrease in wind speed in the Gulf of Lion area, which was found in previous studies, could be potentially attributed to fewer Tramontane events in future climate. Since Mistral and Tramontane events are driven orographically and by pressure patterns, the classification algorithm should be able to identify possible Mistral and Tramontane situations in projections as well. It appears unlikely that these findings are due to incorrect identification of M/T situations.

On about 80% of days, the RCMs and their driving GCMs agree on the occurrence of Mistral and Tramontane winds. In this study, each RCM was driven by a different GCM. This makes it difficult to estimate how different RCMs would simulate Mistral and Tramontane winds when given the same GCM input data. Therefore, it would be interesting to run several RCMs with the same GCM forcing and to increase the ensemble size in future studies.

Acknowledgements

This work is part of the Med-CORDEX initiative (www.medcordex.eu) supported by the HyMeX program (www.hymex.org); it is a contribution to the HyMeX program (HYdrological cycle in The Mediterranean EXperiment) made possible through INSU-MISTRALS support.

We acknowledge the World Climate Research Programme's Working Group on Coupled Modelling, which is responsible for CMIP, and we thank the climate modeling groups (listed in Table D.1 of this paper) for producing and making available their model output. For CMIP, the U.S. Department of Energy's Program for Climate Model Diagnosis and Intercomparison provided coordinating support and led the development of software infrastructure in partnership with the Global Organization for Earth System Science Portals.

The simulations used in this work were downloaded from the Med-CORDEX database. Gust time series were provided by Valérie Jacq (Météo-France), who unfortunately passed away recently and would have been happy to see such a study.

GUF simulations were performed at DKRZ and LOEWE-CSC. B. A. acknowledges support from Senckenberg BiK-F. B. A. and A. O.-H. acknowledge support by the German Federal Ministry of Education and Research (BMBF) under Grant MiKlip: Regionalization 01LP1518C. S. S. was supported by the French National Research Agency (ANR) project REMEMBER (contract ANR-12-SENV-001).

Bibliography

Abulafia D., Bischoff M. (2013) Das Mittelmeer: Eine Biographie. FISCHER E-Books

Accadia C., Zecchetto S., Lavagnini A., Speranza A. (2007) Comparison of 10-m Wind Forecasts from a Regional Area Model and QuikSCAT Scatterometer Wind Observations over the Mediterranean Sea. Monthly Weather Review 135(5):1945–1960, DOI 10.1175/MWR3370.1

Akhtar N., Brauch J., Dobler A., Béranger K., Ahrens B. (2014) Medicanes in an ocean–atmosphere coupled regional climate model. Nat Hazards Earth Syst Sci 14:2189–2201

Akhtar N., Brauch J., Ahrens B. (2017) Climate modeling over the Mediterranean Sea: impact of resolution and ocean coupling. Climate Dynamics pp. 1–16, DOI 10.1007/s00382-017-3570-8

Allou A., Forget P., Devenon J.-L. (2010) Submesoscale vortex structures at the entrance of the Gulf of Lions in the Northwestern Mediterranean Sea. Continental Shelf Research 30(7):724–732, DOI http://dx.doi.org/10.1016/j.csr.2010.01.006

Amante C., Eakins B. W. (2009) ETOPO1 1 Arc-Minute Global Relief Model: Procedures, Data Sources and Analysis. NOAA Technical Memorandum NESDIS NGDC-24, DOI 10.7289/V5C8276M

Andreas E. L. (2004) Spray stress revisited. J Phys Oceanogr 34:1429–1439

Artale V., Calmanti S., Carillo A., Dell'Aquila A., Herrmann M., Pisacane G., Ruti P. M., Sannino G., Struglia M. V., Giorgi F., Bi X., Pal J. S., Rauscher S. (2010) An atmosphere–ocean regional climate model for the Mediterranean area: assessment of a present climate simulation. Climate Dynamics 35(5):721–740, DOI 10.1007/s00382-009-0691-8

Barry R. (2008) Mountain Weather and Climate. Cambridge University Press

Bastin S., Drobinski P., Guénard V., Caccia J.-L., Campistron B., Dabas A. M., Delville P., Reitebuch O., Werner C. (2006) On the Interaction between Sea Breeze and Summer Mistral at the Exit of the Rhône Valley. Monthly Weather Review 134(6):1647–1668, DOI 10.1175/MWR3116.1

Beniston M., Stephenson D. B., Christensen O. B., Ferro C. A., Frei C., Goyette S., Halsnaes K., Holt T., Jylhä K., Koffi B., et al. (2007) Future extreme events in European climate: an exploration of regional climate model projections. Climatic Change 81(1):71–95

Béranger K., Drillet Y., Houssais M.-N., Testor P., Bourdallé-Badie R., Alhammoud B., Bozec A., Mortier L., Bouruet-Aubertot P., Crépon M. (2010) Impact of the spatial distribution of the atmospheric forcing on water mass formation in the Mediterranean Sea. Journal of Geophysical Research: Oceans 115(C12):n/a–n/a, DOI 10.1029/2009JC005648

Berthou S., Mailler S., Drobinski P., Arsouze T., Bastin S., Béranger K., Lebeaupin-Brossier C. (2014) Prior history of Mistral and Tramontane winds modulates heavy precipitation events in southern France. Tellus A 66(0)

Berthou S., Mailler S., Drobinski P., Arsouze T., Bastin S., Béranger K., Lebeaupin-Brossier C. (2015) Sensitivity of an intense rain event between atmosphere-only and atmosphere-ocean regional coupled models: 19 September 1996. Quarterly Journal of the Royal Meteorological Society 141(686):258–271, DOI 10.1002/qj.2355

Berthou S., Mailler S., Drobinski P., Arsouze T., Bastin S., Béranger K., Lebeaupin Brossier C. (2016) Lagged effects of the Mistral wind on heavy precipitation through ocean-atmosphere coupling in the region of Valencia (Spain). Climate Dynamics pp. 1–15, DOI 10.1007/s00382-016-3153-0

Blahak U. (2015) Simulating idealized cases with the COSMO-model (draft version). Tech. rep., DWD

Carniel S., Benetazzo A., Bonaldo D., Falcieri F. M., Miglietta M. M., Ricchi A., Sclavo M. (2016) Scratching beneath the surface while coupling atmosphere, ocean and waves: Analysis of a dense water formation event. Ocean Modelling 101:101–112, DOI http://dx.doi.org/10.1016/j.ocemod.2016.03.007

Cavaleri L., Fox-Kemper B., Hemer M. (2012) Wind waves in the coupled climate system. Bull Amer Meteor Soc 93:1651–1661

Charnock H. (1955) Wind stress on a water surface. Quarterly Journal of the Royal Meteorological Society 81(350):639–640, DOI 10.1002/qj.49708135027

Chelton D. B., Schlax M. G., Freilich M. H., Milliff R. F. (2004) Satellite measurements reveal persistent small-scale features in ocean winds. science 303(5660):978–983

Cimbala J., Çengel Y. (2008) Essentials of fluid mechanics: fundamentals and applications. McGraw-Hill series in mechanical engineering, McGraw-Hill Higher Education

Colin J., Déqué M., Radu R., Somot S. (2010) Sensitivity study of heavy precipitation in Limited Area Model climate simulations: influence of the size of the domain and the use of the spectral nudging technique. Tellus A 62(5):591–604, DOI 10.1111/j.1600-0870.2010.00467.x

Corsmeier U., Behrendt R., Drobinski P., Kottmeier C. (2005) The mistral and its effect on air pollution transport and vertical mixing. Atmospheric Research 74(1):275 – 302, DOI http://dx.doi.org/10.1016/j.atmosres.2004.04.010

Dee D. P., Uppala S. M., Simmons A. J., Berrisford P., Poli P., Kobayashi S., Andrae U., Balmaseda M. A., Balsamo G., Bauer P., Bechtold P., Beljaars A. C. M., van de Berg L., Bidlot J., Bormann N., Delsol C., Dragani R., Fuentes M., Geer A. J., Haimberger L., Healy S. B., Hersbach H., Hólm E. V., Isaksen L., Kållberg P., Köhler M., Matricardi M., McNally A. P., Monge-Sanz B. M., Morcrette J.-J., Park B.-K., Peubey C., de Rosnay P., Tavolato C., Thépaut J.-N., Vitart F. (2011) The ERA-Interim reanalysis: configuration and performance of the data assimilation system. Quarterly Journal of the Royal Meteorological Society 137(656):553–597, DOI 10.1002/qj.828

Diffenbaugh N. S., Giorgi F. (2012) Climate change hotspots in the CMIP5 global climate model ensemble. Climatic Change 114(3):813–822, DOI 10.1007/s10584-012-0570-x

Domínguez M., Gaertner M., de Rosnay P., Losada T. (2010) A regional climate model simulation over West Africa: parameterization tests and analysis of land-surface fields. Climate Dynamics 35(1):249–265, DOI 10.1007/s00382-010-0769-3

Doms G., J. Foerstner E. H., Herzog H.-J., Mironov D., Raschendorfer M., Reinhardt T., Ritter B., Schrodin R., Schulz J.-P., Vogel G. (2011) A Description of the Nonhydrostatic Regional COSMO Model Part II: Physical Parameterization

Donelan M. A., Dobson F. W., Smith S. D., Anderson R. J. (1993) On the Dependence of Sea Surface Roughness on Wave Development. J Phys Oceanogr 23(9):2143–2149, DOI 10.1175/1520-0485(1993)023<2143:OTDOSS>2.0.CO;2

Dorman C. E., Mejia J. F., Koračin D. (2013) Impact of US west coastline inhomogeneity and synoptic forcing on winds, wind stress, and wind stress curl during upwelling season. Journal of Geophysical Research: Oceans 118(9):4036–4051

Draxl C., Hahmann A. N., Peña A., Giebel G. (2014) Evaluating winds and vertical wind shear from Weather Research and Forecasting model forecasts using seven planetary boundary layer schemes. Wind Energy 17(1):39–55, DOI 10.1002/we.1555

Drobinski P., Flamant C., Dusek J., Flamant P., Pelon J. (2001) Observational Evidence And Modelling Of An Internal Hydraulic Jump At The Atmospheric Boundary-Layer Top During A Tramontane Event. Boundary-Layer Meteorology 98(3):497–515, DOI 10.1023/A:1018751311924

Drobinski P., Bastin S., Guenard V., Caccia J.-L., Dabas A., Delville P., Protat A., Reitebuch O., Werner C. (2005) Summer mistral at the exit of the Rhône valley. Quarterly Journal of the Royal Meteorological Society 131(605):353–375, DOI 10.1256/qj.04.63

Drobinski P., Ducrocq V., Alpert P., Anagnostou E., Béranger K., Borga M., Braud I., Chanzy A., Davolio S., Delrieu G., Estournel C., Filali Boubrahmi N., Font J., Grubišić V., Gualdi S., Homar V., Ivančan-Picek B., Kottmeier C., Kotroni V., Lagouvardos K., Lionello P., Llasat M. C., Ludwig W., Lutoff C., Mariotti A., Richard E., Romero R., Rotunno R., Roussot O., Ruin I., Somot S., Taupier-Letage I., Tintore J., Uijlenhoet R., Wernli H. (2014) HyMeX: A 10-Year Multidisciplinary Program on the Mediterranean Water Cycle. Bull Amer Meteor Soc 95:1063–1082

Drobinski P., Alonzo B., Basdevant C., Cocquerez P., Doerenbecher A., FourriÃ© N., Nuret M. (2017) Lagrangian dynamics of the mistral during the HyMeX SOP2. Journal of Geophysical Research: Atmospheres 122(3):1387–1402, DOI 10.1002/2016JD025530, 2016JD025530

Edelmann B. (2015) Dependence of COSMO-CLM simulated Wind on Wind Stress Parameterisation in the Gulf of Lion. Master's thesis, Goethe Universität Frankfurt

Finnigan J. (2015) BOUNDARY LAYER (ATMOSPHERIC) AND AIR POLLUTION | Complex Terrain . In: North G. R., Pyle J., Zhang F. (eds) Encyclopedia of Atmospheric Sciences (Second Edition), second edition edn, Academic Press, Oxford, pp. 242 – 249, DOI https://doi.org/10.1016/B978-0-12-382225-3.00084-0

Flaounas E., Drobinski P., Vrac M., Bastin S., Lebeaupin-Brossier C., Stéfanon M., Borga M., Calvet J.-C. (2013) Precipitation and temperature space-time variability and extremes in the Mediterranean region: evaluation of dynamical and statistical downscaling methods. Climate Dynamics 40(11-12):2687–2705, DOI 10.1007/s00382-012-1558-y

Gaberšek S., Durran D. R. (2004) Gap Flows through Idealized Topography. Part I: Forcing by Large-Scale Winds in the Nonrotating Limit. Journal of the Atmospheric Sciences 61(23):2846–2862, DOI 10.1175/JAS-3340.1

Gaberšek S., Durran D. R. (2006) Gap Flows through Idealized Topography. Part II: Effects of Rotation and Surface Friction. Journal of the Atmospheric Sciences 63(11):2720–2739, DOI 10.1175/JAS3786.1

Garcia S. (2014) Channeling effects in the region of Mistral Wind. Master's thesis, Justus-Liebig-Universität Gießen and University College Dublin

Georgelin M., Richard E., Petitdidier M., Druilhet A. (1994) Impact of Subgrid-Scale Orography Parameterization on the Simulation of Orographic Flows. Monthly Weather

Review 122:1509–1522, DOI 10.1175/1520-0493(1994)122<1509:IOSSOP>2.0.CO;2

Giles B. (1977) Fluidics, the Coanda Effect, and some orographic winds. Archiv für Meteorologie, Geophysik und Bioklimatologie, Serie A 25(3):273–279, DOI 10.1007/BF02321800

Giorgetta M. A., Jungclaus J., Reick C. H., Legutke S., Bader J., Böttinger M., Brovkin V., Crueger T., Esch M., Fieg K., Glushak K., Gayler V., Haak H., Hollweg H.-D., Ilyina T., Kinne S., Kornblueh L., Matei D., Mauritsen T., Mikolajewicz U., Mueller W., Notz D., Pithan F., Raddatz T., Rast S., Redler R., Roeckner E., Schmidt H., Schnur R., Segschneider J., Six K. D., Stockhause M., Timmreck C., Wegner J., Widmann H., Wieners K.-H., Claussen M., Marotzke J., Stevens B. (2013) Climate and carbon cycle changes from 1850 to 2100 in MPI-ESM simulations for the Coupled Model Intercomparison Project phase 5. Journal of Advances in Modeling Earth Systems 5(3):572–597, DOI 10.1002/jame.20038

Giorgi F. (2006) Climate change hot-spots. Geophysical Research Letters 33(8):n/a–n/a, DOI 10.1029/2006GL025734, l08707

Giorgi F., Gutowski W. J. (2015) Regional dynamical downscaling and the CORDEX initiative. Annual Review of Environment and Resources 40:467–490

Giorgi F., Coppola E., Solmon F., Mariotti L., Sylla M., Bi X., Elguindi N., Diro G., Nair V., Giuliani G., et al. (2012) RegCM4: model description and preliminary tests over multiple CORDEX domains. Clim Res 52:7–29

Golbraikh E., Shtemler Y. M. (2013) Drag coefficient for the air-sea exchange in hurricane conditions. ArXiv e-prints

Guenard V., Drobinski P., Caccia J.-L., Campistron B., Bench B. (2005) An Observational Study of the Mesoscale Mistral Dynamics. Boundary-Layer Meteorology 115(2):263–288, DOI 10.1007/s10546-004-3406-z

Guénard V., Drobinski P., Caccia J. L., Tedeschi G., Currier P. (2006) Dynamics of the MAP IOP 15 severe Mistral event: Observations and high-resolution numerical simulations. Quarterly Journal of the Royal Meteorological Society 132(616):757–777, DOI 10.1256/qj.05.59

Herrmann M., Somot S., Calmanti S., Dubois C., Sevault F. (2011) Representation of daily wind speed spatial and temporal variability and intense wind events over the Mediterranean Sea using dynamical downscaling : impact of the regional climate model configuration. Nat Hazards Earth Syst Sci 11:1983–2001, DOI 10.5194/nhess-11-1983-2011

Hong S.-Y., Noh Y., Dudhia J. (2006) A new vertical diffusion package with an explicit treatment of entrainment processes. Monthly Weather Review 134:2318–2341

Hourdin F., Musat I., Bony S., Braconnot P., Codron F., Dufresne J.-L., Fairhead L., Filiberti M.-A., Friedlingstein P., Grandpeix J.-Y., Krinner G., LeVan P., Li Z.-X., Lott F. (2006) The LMDZ4 general circulation model: climate performance and sensitivity to parametrized physics with emphasis on tropical convection. Climate Dynamics 27(7-8):787–813, DOI 10.1007/s00382-006-0158-0

Hueging H., Haas R., Born K., Jacob D., Pinto J. G. (2013) Regional changes in wind energy potential over Europe using regional climate model ensemble projections. Journal of Applied Meteorology and Climatology 52(4):903–917

Jacq V. (2011) personal communication

Jacq V., Albert P., Delorme R. (2005) Le mistral, en 1925 et aujourd'hui : Le mistral - Quelques aspects des connaissances actuelles. La Météorologie 50:30–38

Jiménez P., Dudhia J. (2014) On the wind stress formulation over shallow waters in atmospheric models. Geoscientific Model Development Discussions 7(6):9063–9077

Jungclaus J., Fischer N., Haak H., Lohmann K., Marotzke J., Matei D., Mikolajewicz U., Notz D., Storch J. (2013) Characteristics of the ocean simulations in the Max Planck Institute Ocean Model (MPIOM) the ocean component of the MPI-Earth system model. Journal of Advances in Modeling Earth Systems 5(2):422–446

Jungo P., Goyette S., Beniston M. (2002) Daily wind gust speed probabilities over Switzerland according to three types of synoptic circulation. International journal of climatology 22(4):485–499

Kothe S., Panitz H.-J., Ahrens B. (2014) Analysis of the radiation budget in regional climate simulations with COSMO-CLM for Africa. Meteorologische Zeitschrift 23(2):123–141, DOI 10.1127/0941-2948/2014/0527

Lange B., Højstrup J., Larsen S., Barthelmie R. (2001) A Fetch Dependent Model Of Sea Surface Roughness For Offshore Wind Power Utilisation. In: PROCEEDINGS OF THE EUROPEAN WIND ENERGY CONFERENCE (COPENHAGEN 2001), WIP, MUNICH AND ETA, FLORENZ, pp. 830–833

Lawrence D., Slingo J. (2004a) An annual cycle of vegetation in a GCM. Part I: implementation and impact on evaporation. Climate Dynamics 22(2-3):87–105, DOI 10.1007/s00382-003-0366-9

Lawrence D., Slingo J. (2004b) An annual cycle of vegetation in a GCM. Part II: global impacts on climate and hydrology. Climate Dynamics 22(2-3):107–122, DOI 10.1007/s00382-003-0367-8

Lebeaupin Brossier C., Drobinski P. (2009) Numerical high-resolution air-sea coupling over the Gulf of Lions during two tramontane/mistral events. Journal of Geophysical Research: Atmospheres 114(D10):n/a–n/a, DOI 10.1029/2008JD011601, d10110

Lionello P., Bhend J., Buzzi A., Della-Marta P., Krichak S., Jansà A., Maheras P., Sanna A., Trigo I., Trigo R. (2006) Chapter 6 Cyclones in the Mediterranean region: Climatology and effects on the environment. Developments in Earth and Environmental Sciences 4:325 – 372, DOI http://dx.doi.org/10.1016/S1571-9197(06)80009-1, mediterranean

Lionello P., Abrantes F., Congedi L., Dulac F., Gacic M., Gomis D., Goodess C., Hoff H., Kutiel H., Luterbacher J., Planton S., Reale M., Schröder K., Struglia M. V., Toreti A., Tsimplis M., Ulbrich U., Xoplaki E. (2012) Introduction: Mediterranean Climate–Background Information. In: Lionello P. (ed) The Climate of the Mediterranean Region, Elsevier, Oxford, pp. xxxv – xc, DOI http://dx.doi.org/10.1016/B978-0-12-416042-2.00012-4

Lott F., Miller M. J. (1997) A new subgrid-scale orographic drag parametrization: Its formulation and testing. Quarterly Journal of the Royal Meteorological Society 123(537):101–127, DOI 10.1002/qj.49712353704

Louka P., Galanis G., Siebert N., Kariniotakis G., Katsafados P., Pytharoulis I., Kallos G. (2008) Improvements in wind speed forecasts for wind power prediction purposes using Kalman filtering. Journal of Wind Engineering and Industrial Aerodynamics 96(12):2348–2362, DOI http://dx.doi.org/10.1016/j.jweia.2008.03.013

Lungu T., Dunbar S., Weiss B., Stiles B., Huddleston J., Callahan P., Shirtliffe G., Perry K. L., Hsu C., Mears C., Wentz F., Smith D. (2006) QuikSCAT science data product user's manual version 3.0. Rep. D-18053, 97 pp., Jet Propulsion Laboratory

Madec G. (2008) NEMO ocean engine. Note du Pole de modélisation, 27, 1288–1619, Institut Pierre-Simon Laplace (IPSL)

Madec G., Delecluse P., Imbard M., Levy C. (1997) Ocean general circulation model reference manual. Note du Pôle de modélisation

Mariotti A., Struglia M. V., Zeng N., Lau K.-M. (2002) The Hydrological Cycle in the Mediterranean Region and Implications for the Water Budget of the Mediterranean Sea. Journal of Climate 15(13):1674–1690, DOI 10.1175/1520-0442(2002)015<1674:THCITM>2.0.CO;2

Marshall J., Schott F. (1999) Open-ocean convection: Observations, theory, and models. Reviews of Geophysics 37(1):1–64, DOI 10.1029/98RG02739

Martin G. M., Bellouin N., Collins W. J., Culverwell I. D., Halloran P. R., Hardiman S. C., Hinton T. J., Jones C. D., McDonald R. E., McLaren A. J., O'Connor F. M., Roberts M. J., Rodriguez J. M., Woodward S., Best M. J., Brooks M. E., Brown A. R., Butchart N., Dearden C., Derbyshire S. H., Dharssi I., Doutriaux-Boucher M., Edwards J. M., Falloon P. D., Gedney N., Gray L. J., Hewitt H. T., Hobson M., Huddleston M. R., Hughes J., Ineson S., Ingram W. J., James P. M., Johns T. C., Johnson C. E.,

Jones A., Jones C. P., Joshi M. M., Keen A. B., Liddicoat S., Lock A. P., Maidens A. V., Manners J. C., Milton S. F., Rae J. G. L., Ridley J. K., Sellar A., Senior C. A., Totterdell I. J., Verhoef A., Vidale P. L., Wiltshire A. (2011) The HadGEM2 family of Met Office Unified Model climate configurations. Geoscientific Model Development 4(3):723–757, DOI 10.5194/gmd-4-723-2011

Mass C. F., Ovens D., Westrick K., Colle B. A. (2002) Does increasing horizontal resolution produce more skillful forecasts? Bulletin of the American Meteorological Society 83(3):407–430

Mauritsen T., Stevens B., Roeckner E., Crueger T., Esch M., Giorgetta M., Haak H., Jungclaus J., Klocke D., Matei D., Mikolajewicz U., Notz D., Pincus R., Schmidt H., Tomassini L. (2012) Tuning the climate of a global model. Journal of Advances in Modeling Earth Systems 4(3):n/a–n/a, DOI 10.1029/2012MS000154, m00A01

Météo-France (2009) ARPEGE-Climat V5.1 algorithmic documentation. Tech. rep., Météo-France/CNRM

Moss R. H., Edmonds J. A., Hibbard K. A., Manning M. R., Rose S. K., Van Vuuren D. P., Carter T. R., Emori S., Kainuma M., Kram T., et al. (2010) The next generation of scenarios for climate change research and assessment. Nature 463(7282):747–756

Najac J., Boé J., Terray L. (2008) A multi-model ensemble approach for assessment of climate change impact on surface winds in France. Climate Dynamics 32(5):615–634, DOI 10.1007/s00382-008-0440-4

Najac J., Lac C., Terray L. (2011) Impact of climate change on surface winds in France using a statistical-dynamical downscaling method with mesoscale modelling. International Journal of Climatology 31(3):415–430, DOI 10.1002/joc.2075

Nakicenovic N., Swart R. (2000) Special Report on Emissions Scenarios: A Special Report of Working Group III of the International Panel on Climate Change. Cambridge University Press

Nikulin G., Kjellström E., Hansson U., Strandberg G., Ullerstig A. (2011) Evaluation and future projections of temperature, precipitation and wind extremes over Europe in an ensemble of regional climate simulations. Tellus A 63(1):41–55, DOI 10.1111/j.1600-0870.2010.00466.x

Obermann A., Bastin S., Belamari S., Conte D., Gaertner M. A., Li L., Ahrens B. (2016a) Mistral and Tramontane wind speed and wind direction patterns in regional climate simulations. Climate Dynamics pp. 1–18, DOI 10.1007/s00382-016-3053-3

Obermann A., Edelmann B., Ahrens B. (2016b) Influence of sea surface roughness length parameterization on Mistral and Tramontane simulations. Advances in Science and Research 13:107–112, DOI 10.5194/asr-13-107-2016

Overland J. E. (1984) Scale Analysis of Marine Winds in Straits and along Mountainous Coasts. Monthly Weather Review 112(12):2530–2534, DOI 10.1175/1520-0493(1984)112<2530:SAOMWI>2.0.CO;2

Parish T. (2015) MOUNTAIN METEOROLOGY | Katabatic Winds. In: North G. R., Pyle J., Zhang F. (eds) Encyclopedia of Atmospheric Sciences (Second Edition), second edition edn, Academic Press, Oxford, pp. 75 – 79, DOI http://dx.doi.org/10.1016/B978-0-12-382225-3.00189-4

Pinto J. G., Karremann M. K., Born K., Della-Marta P. M., Klawa M. (2012) Loss potentials associated with European windstorms under future climate conditions. Climate Research 54(1):1–20

Potter H. (2015) Swell and the drag coefficient. Ocean Dynamics 65(3):375–384, DOI 10.1007/s10236-015-0811-4

Powell M. D., Vickery P. J., Reinhold T. A. (2003) Reduced drag coefficient for high wind speeds in tropical cyclones. Nature 422(6929):279–283

Pryor S., Schoof J. T., Barthelmie R. (2006) Winds of change?: Projections of near-surface winds under climate change scenarios. Geophysical Research Letters 33(11)

Pryor S., Barthelmie R. J., Clausen N.-E., Drews M., MacKellar N., Kjellström E. (2012) Analyses of possible changes in intense and extreme wind speeds over northern Europe under climate change scenarios. Climate dynamics 38(1-2):189–208

Pugnet L., Chong D., Duff T., Tolhurst K. (2013) Wildland–urban interface (WUI) fire modelling using PHOENIX Rapidfire: A case study in Cavaillon, France. In: Proceedings of the 20th International Congress on Modelling and Simulation, Adelaide, Australia, pp. 1–6

Quintana-Seguí P., Le Moigne P., Durand Y., Martin E., Habets F., Baillon M., Canellas C., Franchisteguy L., Morel S. (2008) Analysis of near-surface atmospheric variables: Validation of the SAFRAN analysis over France. Journal of applied meteorology and climatology 47(1):92–107

Reiter E. R. (1975) Handbook for Forecasters in the Mediterranean, Weather Phenomena of the Mediterranean Basin: Part 1. General Description of the Meteorological Processes. Tech. rep.

Renault L., Chiggiato J., Warner J. C., Gomez M., Vizoso G., Tintoré J. (2012) Coupled atmosphere-ocean-wave simulations of a storm event over the Gulf of Lion and Balearic Sea. Journal of Geophysical Research: Oceans 117(C9):n/a–n/a, DOI 10.1029/2012JC007924, c09019

Ricchi A., Miglietta M. M., Falco P. P., Benetazzo A., Bonaldo D., Bergamasco A., Sclavo M., Carniel S. (2016) On the use of a coupled ocean-atmosphere-wave model during an extreme cold air outbreak over the Adriatic Sea. Atmospheric Research 172-173:48–65, DOI http://dx.doi.org/10.1016/j.atmosres.2015.12.023

Risien C. M., Chelton D. B. (2006) A satellite-derived climatology of global ocean winds. Remote Sensing of Environment 105(3):221–236, DOI http://dx.doi.org/10.1016/j.rse.2006.06.017

Rockel B., Woth K. (2007) Extremes of near-surface wind speed over Europe and their future changes as estimated from an ensemble of RCM simulations. Climatic Change 81(1):267–280

Rockel B., Will A., Hense A. (2008) The regional climate model COSMO-CLM (CCLM). Meteorologische Zeitschrift 17(4):347–348

Roeckner E., Bäuml G., Bonaventura L., Brokopf R., Esch M., Giorgetta M., Hagemann S., Kirchner I., Kornblueh L., Manzini E., Rhodin A., Schlese U., Schulzweida U., Tompkins A. (2003) The atmospheric general circulation model ECHAM 5. PART I: Model description. Report / MPI für Meteorologie 349

Ruti P. M., Marullo S., D'Ortenzio F., Tremant M. (2008) Comparison of analyzed and measured wind speeds in the perspective of oceanic simulations over the Mediterranean basin: Analyses, QuikSCAT and buoy data. Journal of Marine Systems 70(1-2):33–48

Ruti P. M., Somot S., Giorgi F., Dubois C., Flaounas E., Obermann A., Dell'Aquila A., Pisacane G., Harzallah A., Lombardi E., Ahrens B., Akhtar N., Alias A., Arsouze T., Aznar R., Bastin S., Bartholy J., Béranger K., Beuvier J., Bouffies-Cloché S., Brauch J., Cabos W., Calmanti S., Calvet J.-C., Carillo A., Conte D., Coppola E., Djurdjevic V., Drobinski P., Elizalde-Arellano A., Gaertner M., Galàn P., Gallardo C., Gualdi S., Goncalves M., Jorba O., Jordà G., L'Heveder B., Lebeaupin-Brossier C., Li L., Liguori G., Lionello P., Maciàs D., Nabat P., Önol B., Raikovic B., Ramage K., Sevault F., Sannino G., Struglia M. V., Sanna A., Torma C., Vervatis V. (2016) Med-CORDEX Initiative for Mediterranean Climate Studies. Bulletin of the American Meteorological Society 97(7):1187–1208, DOI 10.1175/BAMS-D-14-00176.1

Sanchez-Gomez E., Somot S., Déqué M. (2009) Ability of an ensemble of regional climate models to reproduce weather regimes over Europe-Atlantic during the period 1961–2000. Climate Dynamics 33(5):723–736, DOI 10.1007/s00382-008-0502-7

Schaeffer A., Garreau P., Molcard A., Fraunié P., Seity Y. (2011) Influence of high-resolution wind forcing on hydrodynamic modeling of the Gulf of Lions. Ocean Dynamics 61(11):1823–1844, DOI 10.1007/s10236-011-0442-3

Schmidtke H., Scherrer H. (1997) Sturmschäden im Wald. Schlussbericht / NFP 31, vdf, Hochschulverlag AG an der ETH Zürich

Schott F., Visbeck M., Send U., Fischer J., Stramma L., Desaubies Y. (1996) Observations of deep convection in the Gulf of Lions, northern Mediterranean, during the winter of 1991/92. Journal of Physical Oceanography 26(4):505–524

Schulz J.-P. (2008) Introducing sub-grid scale orographic effects in the COSMO model. COSMO Newsletter 9:29–36

Scutari M. (2010) Learning Bayesian Networks with the bnlearn R Package. Journal of Statistical Software 35(3):1–22

Simpson J. E. (1994) Sea breeze and local winds. Cambridge University Press

Skamarock W., Klemp J., Dudhia J., Gill D., Barker D., Duda M., Huang X., Wang W., Powers J. (2008) A description of the advanced research WRF version 3. Tech. rep., NCAR

Small R., Carniel S., Campbell T., Teixeira J., Allard R. (2012) The response of the Ligurian and Tyrrhenian Seas to a summer Mistral event: A coupled atmosphere-ocean approach. Ocean Modelling 48(0):30–44, DOI http://dx.doi.org/10.1016/j.ocemod.2012.02.003

Smith R. (2015) MOUNTAIN METEOROLOGY | Overview. In: North G. R., Pyle J., Zhang F. (eds) Encyclopedia of Atmospheric Sciences (Second Edition), second edition edn, Academic Press, Oxford, pp. 57 – 61, DOI https://doi.org/10.1016/B978-0-12-382225-3.00239-5

Somot S., Sevault F., Déqué M. (2006) Transient climate change scenario simulation of the Mediterranean Sea for the twenty-first century using a high-resolution ocean circulation model. Climate Dynamics 27(7):851–879, DOI 10.1007/s00382-006-0167-z

Somot S., Houpert L., Sevault F., Testor P., Bosse A., Taupier-Letage I., Bouin M.-N., Waldman R., Cassou C., Sanchez-Gomez E., Durrieu de Madron X., Adloff F., Nabat P., Herrmann M. (2016) Characterizing, modelling and understanding the climate variability of the deep water formation in the North-Western Mediterranean Sea. Climate Dynamics pp. 1–32, DOI 10.1007/s00382-016-3295-0

Stéfanon M. M., Drobinski P., D'Andrea F., Lebeaupin-Brossier C., Bastin S. (2014) Soil moisture-temperature feedbacks at meso-scale during summer heat waves over Western Europe. Climate Dynamics 42(5-6):1309–1324, DOI 10.1007/s00382-013-1794-9

Stevens B., Giorgetta M., Esch M., Mauritsen T., Crueger T., Rast S., Salzmann M., Schmidt H., Bader J., Block K., Brokopf R., Fast I., Kinne S., Kornblueh L., Lohmann U., Pincus R., Reichler T., Roeckner E. (2013) Atmospheric component of the MPI-M

Earth System Model: ECHAM6. Journal of Advances in Modeling Earth Systems 5(2):146–172

von Storch H., Zwiers F. (2001) Statistical Analysis in Climate Research. Cambridge University Press

Taylor K. E., Stouffer R. J., Meehl G. A. (2012) An overview of CMIP5 and the experiment design. Bulletin of the American Meteorological Society 93(4):485–498

Thévenot O., Bouin M.-N., Ducrocq V., Lebeaupin Brossier C., Nuissier O., Pianezze J., Duffourg F. (2015) Influence of the sea state on Mediterranean heavy precipitation: a case-study from HyMeX SOP1. Quarterly Journal of the Royal Meteorological Society pp. n/a–n/a, DOI 10.1002/qj.2660

Torma C., Giorgi F. (2014) Assessing the contribution of different factors in regional climate model projections using the factor separation method. Atmospheric Science Letters 15(4):239–244, DOI 10.1002/asl2.491

Tsamardinos I., Brown L. E., Aliferis C. F. (2006) The max-min hill-climbing Bayesian network structure learning algorithm. Machine Learning 65(1):31–78, DOI 10.1007/s10994-006-6889-7

Ulbrich U., Lionello P., Belušić D., Jacobeit J., Knippertz P., Kuglitsch F. G., Leckebusch G. C., Luterbacher J., Maugeri M., Maheras P., Nissen K. M., Pavan V., Pinto J. G., Saaroni H., Seubert S., Toreti A., Xoplaki E., Ziv B. (2012) 5 - Climate of the Mediterranean: Synoptic Patterns, Temperature, Precipitation, Winds, and Their Extremes . In: Lionello P. (ed) The Climate of the Mediterranean Region, Elsevier, Oxford, pp. 301 – 346, DOI https://doi.org/10.1016/B978-0-12-416042-2.00005-7

Vidal J.-P., Martin E., Franchistéguy L., Baillon M., Soubeyroux J.-M. (2010) A 50-year high-resolution atmospheric reanalysis over France with the Safran system. International Journal of Climatology 30:1627–1644

Voldoire A., Sanchez-Gomez E., Salas y Mélia D., Decharme B., Cassou C., Sénési S., Valcke S., Beau I., Alias A., Chevallier M., Déqué M., Deshayes J., Douville H., Fernandez E., Madec G., Maisonnave E., Moine M.-P., Planton S., Saint-Martin D., Szopa S., Tyteca S., Alkama R., Belamari S., Braun A., Coquart L., Chauvin F. (2013) The CNRM-CM5.1 global climate model: description and basic evaluation. Climate Dynamics 40(9-10):2091–2121

Warrens M. J. (2008) On association coefficients for $2\times$ 2 tables and properties that do not depend on the marginal distributions. Psychometrika 73(4):777–789